A high-power laser transmitter for ground-based and airborne water-vapor measurements in the troposphere

Dissertation zur Erlangung des Doktorgrades
der Naturwissenschaften (Dr. rer. nat.)

Fakultät Naturwissenschaften
Universität Hohenheim

Institut für Physik und Meteorologie

Vorgelegt von
Max Schiller

aus Moskau, Russische Föderation

Stuttgart, Deutschland
2009

This thesis was accepted as a doctoral dissertation in fulfillment of the requirements for the degree "Doktor der Naturwissenschaften" by the Faculty of Natural Sciences at the University of Hohenheim, Stuttgart, Germany on 12 March 2009.

Date of oral examination: 6 July 2009

Examination committee:

Supervisor and reviewer:	Prof. Dr. Volker Wulfmeyer
	Institute of Physics and Meteorology,
	University of Hohenheim
Co-reviewer:	Prof. Dr. Martin Ostermeyer
	Group of Nonlinear Optics and experimental Quantum Information Processing,
	University of Potsdam
Additional examiner:	Prof. Dr. Kurt Jetter
	Institute of Applied Mathematics and Statistics,
	University of Hohenheim
Dean:	Prof. Dr. Stephan C. Bischoff
	Faculty of Natural Sciences,
	University of Hohenheim

To my Mom

Abstract

A gain-switched high-power single-frequency Ti:sapphire laser was developed. It is pumped with a frequency-doubled diode-pumped Nd:YAG laser. The laser fulfills the requirements for a transmitter of a water-vapor differential absorption lidar (DIAL), intended for accurate high temporally- and spatially-resolved measurements from the ground to the upper troposphere. The laser was developed using thermal, resonator-design, spectral, and pulse-evolution models. There were layouts assembled for operation at 935 nm and 820 nm optimized for airborne and ground-based measurements, respectively.

A birefringent filter and an external-cavity diode laser as an injection seeder are controlling the spectral properties of the transmitter. With a 1σ frequency stability of $< 60\,\text{MHz}$, an emission bandwidth of $< 160\,\text{MHz}$, and a spectral purity of $> 99.7\,\%$, the total error from the laser properties is smaller than 5 % for water-vapor measurements in the troposphere. The laser beam profile is near-Gaussian with $M^2 < 2$. The achieved laser power was 4.5 W at 935 nm and 7 W at 820 nm at repetition rate of 250 Hz. These values are the highest reported for a single-frequency Ti:sapphire laser.

As a part of a ground-based water-vapor DIAL system, the transmitter was deployed during the measurement campaign COPS (Convective and Orographically-induces Precipitation Study). Comparisons with radiosondes confirmed a high precision of the acquired water-vapor day- and nighttime measurements.

Zusammenfassung

Ein verstärkungsgeschalter leistungsstarker monofrequenter Ti:Saphir-Laser, der mit einem frequenzverdoppeltem diodengepumpten Nd:YAG Laser gepumpt ist, wurde entwickelt. Der Laser erfüllt die hohen Anforderungen eines Transmitters für ein Wasserdampf-Differential-Absorption-Lidar (DIAL), der mit hoher zeitlicher und räumlicher Auflösung Messungen innerhalb der Troposphäre durchführen soll. Für die Entwicklung des Lasers wurden Modelle für die thermischen Eigenschaften, das Resonatordesign, das Emissionspektrum sowie den Pulsaufbau verwendet. Es wurden Laseraufbauten gefertigt, die für den Einsatz bei 935 nm für Flugzeug-Plattformen bzw. 820 nm für bodengestützte Messungen optimiert sind.

Ein doppelbrechender Filter und ein External-Cavity-Diodenlaser als Injection-seeder sorgen für die hohe Güte der spektralen Eigenschaften des Senders. Mit einer 1σ-Frequenzstabilität < 60 MHz, einer Bandbreite < 160 MHz und einer spektralen Reinheit $> 99,7$ % ist der Gesamtfehler der Wasserdampfmessungen in der Troposphäre, der durch die Eigenschaften des Lasers bedingt ist, kleiner als 5 %. Werte der mittleren Ausgangsleistung von 4,5 W bei 935 nm und 7 W bei 820 nm sind die zur Zeit höchsten, die von einem monofrequenten Ti:Saphir-Laser mit nahezu gaussförmigem Strahlprofil und $M^2 < 2$ erreicht wurden.

Als Teil eines bodengestützten Wasserdampf DIALs, wurde der Transmitter während der Messkampagne COPS (Convective and Orographically-induces Precipitation Study) verwendet. Vergleiche von Messungen bei Tag und bei Nacht mit Radiosondenaufstiegen zeigten gute Übereinstimmungen.

Contents

Acronyms

ABL – atmospheric boundary layer

AC – (multipass) absorption cell

AGL – above the ground level

AR – anti-reflective

BF – birefringent (Lyot) filter

BS – beam splitter

CCD – charge-coupled device

COPS – Convective and Orographically-induced Precipitation Study

cw – continuous wave

DIAL – differential absorption lidar

DM – dichroic mirror

ECDL – external-cavity diode laser

EM – electro-magnetic

FSR – free spectral range

FR – Faraday rotator

HR – high-reflective

FI – Faraday (optical) isolator (diode)

IOP – intensive observation period (during measurement campaign)

IS – injection seeder

LIDT –laser-induced damage threshold

MO – master oscillator

MOPA – master oscillator – power amplifier

Nd:YAG – yttrium aluminium garnet activated with neodymium ions Nd^{3+}

OC – output coupler

PDH – Pound-Drewer-Hall (stabilization technique)

SHG – second harmonic generation

SNR – signal-to-noise ratio

TEM – transverse electro-magnetic

TISA – sapphire activated with titan ions T^{3+}

WWRP – world weather research programme

List of Figures

List of Tables

Chapter 1

Introduction

Nowadays requirements for the accuracy of the weather forecast become more stringent every year caused by increasing population density and thus increasing vulnerability of human life and economics to extreme weather events. A failure of a forecast may cause severe economical losses, as it happened by the flood in Europe in 2002 with 30 billion Euro damage. Due to the report of one of the world biggest insurance agencies "Swiss Re", only insured losses caused by natural factors in 2007 exceeded 70 billion US$ worldwide (23 billion US$ in Europe). Existing weather forecast models, for example the model of the Deutsche Wetterdienst (DWD), still suffers limited predictability of extreme events, especially in regions with a complex orography. Among other issues they suffer from a lack of reliable data of the 3-d distribution of water vapor [e.g., Schwitalla et al., 2008; Zus et al., 2008].

The simulation of the mesoscale water-vapor distribution is fundamental for the precipitation forecast down to the scales of catchments and land-use with a high accuracy. Without this information, progress in understanding such atmospheric processes as orographically-induced convection and formation of clouds [DWD, 2001; Wulfmeyer, 2008a,b] is very limited. Better knowledge in this area allows for improved and prolonged prediction of hailstorms and other extreme events on the mesoscale.

With the growing of understanding of the human impact on the climate trend, the corresponding studies attracted in the last decade large attention of the society. Variety of scenarios according to different green-house gas emission and diverse respond of the Earth system are already used for global and regional simulation and for political council. However, regional climate simulations are still limited by poor knowledge of processes like land-surface exchange convection, formation of clouds and initiation of precipitation [IPCC, 2007; IPCC, 2008].

Accurate, spatio-temporal, high-resolved measurements of the 3-d distribution of water vapor can make major contribution in this connection [Emanuel et al., 1995; Wulfmeyer et al., 2003].

These challenges in the weather forecast led to initiation of several programs, e.g. the Priority Program (PP) 1167 "Quantitative Precipitation Forecast PQP" by the German Research Foundation (DFG) in 2003 (PQP stands for "Praecipitationis Quantitativae Praedictio") [Hense et al., 2004] with a 1-year general observation period (GOP) and a 3-month intensive observation period over western France and south-eastern Germany in 2007 named COPS (Convective and Orographically-induced Precipitation Study) [Wulfmeyer et al., 2008a]. In order to achieve maximum measurement synergy, GOP and COPS were coordinated with several national and international programs, e.g. THORPEX, a Global Atmospheric Research Program of the World Weather Research Program (WWRP) of the WMO (World Meteorological Organization), TRACKS (Transport and Chemical Conversion in Convective Systems) of German Helmholtz Center, ARM (Atmospheric Radiation Measurement) of US Department of Energy.

For the climate research water-vapor measurements were requested by the World Meteorological Organization (WMO) within the Global Energy and Water Cycle Experiment (GEWEX) and the Global Water Vapor Project (GVAP) as well as by the National Research Council of the USA. Recently, several initiatives have been inaugurated in order to coordinate and to further develop suitable observing systems, e.g., the Integrated Global Observing Strategy (IGOS) with its "Water Cycle Theme", the Global Climate Observing System (GCOS), and the Global Earth Observing System of Systems (GEOSS). The Committee on Earth Observing Satellites (CEOS) (e.g., WMO 2000) is developing requirements for suitable space borne systems.

An observing system has to fulfill certain specifications to deliver data of the mentioned quality. The requirements are well known to the scientific community. For water-vapor measurements in climate research, there is mainly a request for sensors, which can measure vertical profiles with high resolution and accuracy (error < 10 %) day and night up to the lower stratosphere. The high accuracy of the measurements must be granted for several decades in order to allow for trend analyses. In weather research networks ground-based, scanning systems are required able to build within 10 minutes a 3-d map of an inhomogeneous water-vapor field with a few hundred meters vertical and horizontal resolution and overall error instrumental uncertainty < 5 % [Weckwerth et al., 1999; Wulfmeyer et al., 2003]. An observing system with such a high fidelity can be defined as a reference one for water-vapor measurements [Wulfmeyer et al., 2006]. Table 1.1 summarizes the accuracy requirements for the water-vapor measurement, requested by

Table 1.1 Requirements set for the next generation of water-vapor measuring systems [Wulfmeyer and Walter, 2001a; Wulfmeyer and Walter, 2001b; Wulfmeyer et al., 2003; Gérard et al., 2004; Di Girolamo et al., 2004]

Parameter	Turbulence	Weather forecast	Initiation of convection	Regional climate	Global climate
Horizontal resolution, m	30	200-2000	300	10000	50000
Vertical resolution in ABL, m	30	100	100	300	500
Vertical resolution in free troposhere, m	—[1]	1000	1000	1000	2000
Repeatability	1 s	900 s	600 s	1 h	6 h
Precision, %	5	10	10	10	10
Bias, %	5[2]	5	5	1-2	1-2
Timeliness, h	—	1 for nowcasting	—	—	—
Coverage	Vertical profiling[3]	2-d, 3-d, radius >10 km from ground[4]	2-d, 3-d, radius >10 km from ground	100x100 km^2 [5]	Global

ABL – atmospheric boundary layer; 1) only applications in ABL considered; 2) must mainly be time independent; 3) 2-d or 3-d measurements would be very beneficial; 4) set-up of networks important; 5) using ground-based networks or space borne remote sensing

atmosphere processes, weather and climate studies for ground-based, airborne and space borne observing systems.

Presently, there are no sensors available of the required accuracy, specially for measurements in the daytime. Precision and resolution of the existing instruments is by far not sufficient to provide the information necessary for a deeper process understanding. For example, none of the existing sensors has the ability to measure 3-d water-vapor fields with the aim to determine their vertical and horizontal inhomogeneities. A new generation of ground-based, airborne and satellite borne observing systems is therefore required.

The goal of this work was the design of a transmitter for an observing system, to provide a high spatially- and temporally-resolved low-error profiling of water-vapor fields in the atmosphere during day- and nighttime measurements. The developed transmitter was incorporated into a ground-based DIAL system and operated extensively. Furthermore, its applicability for airborne and space borne platforms was demonstrated as well.

Chapter 2 contains an overview of available water-vapor sensors, formalization of the requirements to the transmitter and definition of its principal layout. In Chapters 3, 4 and 5 development process of the transmitter is shown, from modeling to a working prototype and its specification. In Chapter 6 results of the first field experiment using the created device are presented. Chapter 7 contains summary of the performed work and an outlook.

Chapter 2

Lidar measurements of water vapor with high spatial and temporal resolution

2.1 Overview of measurement techniques

A brief overview of the remote sensing systems for profiling of the atmospheric water vapor is presented here. According to the specification (see Table 1.1), two-to-three dimensional measurements of the atmospheric water vapor are required. Such a task can not be performed with passive remote sensing techniques due to their insufficient spatial resolution.

Among active remote sensing techniques, Global Positioning System (GPS) provides the easiest possibility for the water-vapor in atmosphere. The measurement principle is based on a water-vapor induced delay of the satellite signal, so that the integrated water-vapor content on the track between the transmitter and the receiver can be retrieved [Bevis et al., 1992]. The overall error of approx. 5% makes this technique beneficial for for model verification and for synergetic measurements with high resolution systems. However, a poor horizontal resolution, limited by typical averaging time of 30 minutes, and vertical resolution of $> 1\,\text{km}$ do not allow the application of the GPS for a high-resolved water-vapor profiling of the atmosphere.

Dependency of the air refraction index from the water-vapor partial pressure is deployed for radar measurements of the near-surface humidity [Fabry et al., 1997]. Such an information is useful for present-day mesoscale models. However, this technique does not obtain range-resolved measurements and its implementation is limited to low elevation angles when a radar emission can hit a hard target.

2.1 Overview of measurement techniques

LIght Detection And Ranging (LIDAR) is an active remote sensing technique providing spatial- and temporal-resolved information on key atmospheric variables, e.g. temperature, water vapor concentration, optical properties of aerosols. A lidar system comprises three principle parts: a laser transmitter, a receiver and a data acquisition system. The transmitter generates a laser pulse of few dozens of nanoseconds with certain spectral properties. The pulse is spatially transformed with a beam-matching optics to obtain low beam divergence, not exceeding the field-of-view (FOV) of the telescope of the receiver part (usually < 1 mrad). The pulse enery is emitted into the atmosphere, experience backscatter on molecules and aerosol particles. A fraction of the backscattered emission is picked up by the telescope.

The received radiation is focuses on a detector such as a photomultiplier tube (PMT) or an avalanche photodetector (APD). The acquisition system triggered by the laser pulse, records the time-resolved intensity of the backscattered emission and, hence, its range-resolved profile along the optical axis of the telescope. Steering coaxially the outgoing laser beam and the FOV of the telescope, a 3-d map of the atmospheric backscatter radiation is recorded [Eloranta and Forrest 1992, Spuler and Mayor 2005]. Lidar deployment is limited solely in presence of precipitations and optically thick clouds, causing a strong backscatter in te near-field and signal attenuation in the far-field.

The spatial resolution of the lidar signal along the line of sight is limited by the bandwidth ΔF of an analog-digital converter (ADC): $\Delta r = c/2n\Delta F$, where c/n is the speed of propagation of an electro-magnetic (EM) wave in the atmosphere. The temporal resolution is limited by a repetition rate of the transmitter. To increase the signal-to-noise ratio (SNR), the atmospheric profiles can be averaged in time and in range.

The power of the detected backscattered signal of the EM-emission with a frequency v from a remote r is described with a lidar equation [e.g., Wandinger 2005, Wulfmeyer and Walter 2001a, Wulfmeyer and Walter 2001b]:

$$P_v(r) = P_p \eta \frac{c t_p}{2n} \frac{A}{r^2} O(r) \beta^v(r) \exp\left\{ -2 \int_0^r \alpha^v(r') dr' \right\}, \tag{2.1}$$

with P_p average power in the pulse, η efficiency of the receiver, t_p pulse width, full width on half maximum (FWHM), A/r^2 solid angle, corresponding the field-of-view (FOV) of the receiver, $O(r)$ overlap between the laser beam and the FOV of the receiver. Here $\beta^v = \beta^v_{par} + \beta^v_{mol}$ frequency-dependent total backscatter coefficient caused by aerosol particles and atmospheric

molecules, $\alpha^v = \alpha^v_{par} + \alpha^v_{mol}$ – frequency-dependent total extinction coefficient of aerosol particles and atmospheric molecules.

Among the lidar systems, there are two techniques applicable for water-vapor measurements: a Raman lidar [Melfi, 1969] and a differential absorption lidar (DIAL) [Schotland, 1966].

2.1.1 Raman lidar

The Raman-lidar system is intended to measure the inelastically backscattered signal, emerged during scattering of the EM-emission on that molecules, which absorb part of the exciting photon energy or emit part of their internal energy with the backscattered photon, changing their vibrational and/or rotational state (Raman effect). This change of energy of the photon causes a frequency shift of the backscattered light and is specific for the scattering molecule.

The power of the detected Raman signal of the EM-emission with a frequency v_{Ram} from a remote r is described with a Raman-lidar equation [e.g., Wandinger, 2005; Radlach et al., 2008]:

$$P_{v_{Ram}}(r) = P_p \eta \frac{ct_p}{2n} \frac{A}{r^2} O(r) \beta^{v_{Ram}}(r) \exp\left\{ -\int_0^r \left(\alpha^v(r') + \alpha^{v_{Ram}}(r') \right) dr' \right\}, \qquad (2.2)$$

with P_p average power in the emitted pulse at the transmitter wavelength. This equation has the following distinctions from the conventional lidar Eq.2.1: the backscatter coefficient $\beta^{v_{Ram}}$ is obtained solely by the number density and cross-section of the Raman-active gases; the extinction coefficient on the 'way back' $\alpha^{v_{Ram}}$ is calculated not for the frequency of the transmitter but for the Raman-shifted frequency. Figure 2.1 shows an example of the Raman backscatter spectrum of the atmosphere, corresponding to an incident wavelength of 355 nm.

Applying narrow-band filters in the receiver, the intensity of the Raman-scattering of the gas of interest can be detected. To extract information on the water-vapor mixing ratio, the signal P_R of the Raman-band of water vapor must be compared with a reference one P_{Ref}, usually with the Raman band of nitrogen:

$$m(r) = C \frac{P_{Rv}(r) \exp\left\{ -\int_0^r \alpha^{v'}_{\mathrm{Re}\,f\Sigma}(r') dr' \right\}}{P_{Refv}(r) \exp\left\{ -\int_0^r \alpha^{v'}_{R\Sigma}(r') dr' \right\}}, \qquad (2.3)$$

where C is a calibration constant.
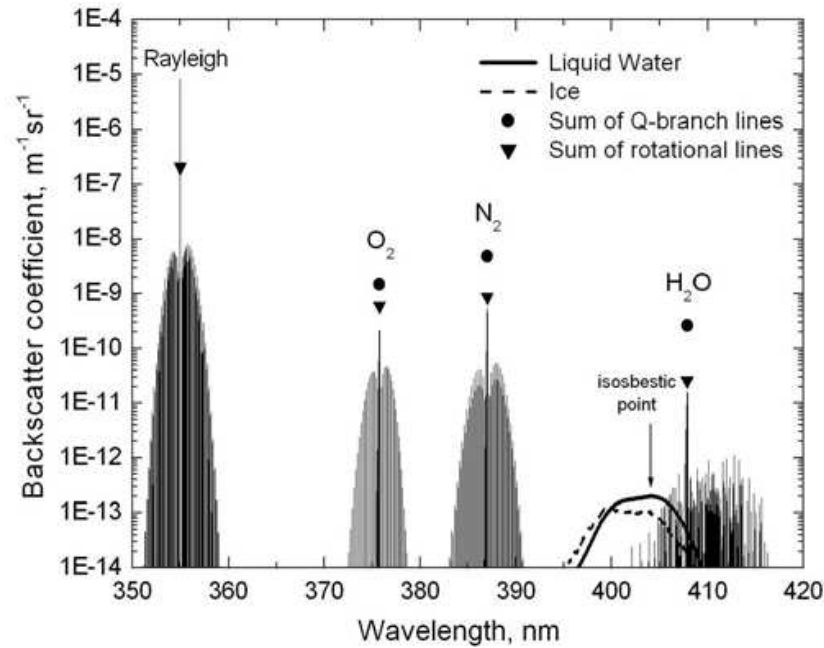
Fig.2.1. Raman backscatter spectrum of the atmospere for an incident laser wavelength of 355 nm, normal pressure, a temperature of 300 K, an N_2 and O_2 content of 0.781 and 0.209, respectively, and a water-vapor mixing ratio of 10 g/kg. The curves for liquid water and ice are arbitrarily scaled. At the isosbestic point the liquid-water backscattered spectrum is temperature insensitive [Wandinger 2005].

However, applicability of this technique is limited by a small cross-section of the Raman scattering. Although the resolution and the accuracy of nighttime measurements satisfy the aforementioned requirements (see Table 1.1), a low SNR during daytime makes water-vapor measurements rather challenging. In spite of availability of new high-power lasers and narrow-band filters, even the most modern Raman lidars provide data with lower quality than DIAL: in the daytime, the maximum uncertainty $< 5\%$ was demonstrated only for the heights up to 4 km, with 60-210 m spatial and 120 s temporal resolution [Whiteman, 2006]. Furthermore, these systems require initial calibration of their receivers [Ferrare et al., 2001; Wulfmeyer and Bösenberg, 1998].

Nevertheless, this robust technique do not require a high spectral purity and frequency stability of the transmitter as with a DIAL. Ones calibrated, the system stays tuned for the whole period of observations. An additional feature of the temperature profiling of the atmosphere makes Raman lidars very attractive for synergetic operations with water-vapor DIAL systems [Behrendt at al., 2005; Radlach et al., 2008].

2.1.2 Differential-absorption lidar

Although the DIAL technique can be applied for atmospheric profiling for a variety of gases (CO_2, SO_2, O_3 etc.) [Gimmestad, 2005], within this thesis implementation of DIALs is described with respect to measurements of atmospheric water vapor.

This technique employees distinctions of water-vapor absorption on different wavelengths to derive information concerning atmospheric water-vapor distribution from the backscattered signal. The transmitter emits pulses at different wavelengths corresponding different absorption cross-section of water vapor. To implement the DIAL technique, the lidar transmitter has to generate at least two wavelengths, one tuned to a water-vapor absorption line (online wavelength), another to a region with low water-vapor absorption (offline wavelength).

If wavelengths are chosen close to each other and the Doppler broadening [Ansmann, 1985] of the backscattered signal can be neglected, the difference between online and offline signals is solely due to water vapor. To derive number density of water vapor at a remote r from the DIAL, the so-called Schotland approximation can be used [e.g., Bösenberg, 1998; Browell et al., 1998]

$$N(r) = \frac{\Delta\alpha(r)}{\Delta\sigma} = \frac{1}{2\Delta\sigma}\frac{\mathrm{d}}{\mathrm{d}r}\ln\left(\frac{P_{on}(r)}{P_{off}(r)}\right), \tag{2.4}$$

$\Delta\alpha = \alpha(v_{on}) - \alpha(v_{off})$ and $\Delta\sigma = \sigma(v_{on}) - \sigma(v_{off})$ is discrepancy of the water-vapor extinction coefficients and absorption cross-sections, respectively, at the online and offline wavelengths, P_{on} and P_{off} are intensities of the backscattered signal at online and offline wavelengths. With the spatial resolution of measurements limited to the size of a range bin Δr, Eq. 2.4 is modified to

$$N(r) = \frac{1}{2\Delta\sigma\Delta r}\ln\left(\frac{P_{off}(r+\Delta r)P_{on}(r)}{P_{off}(r)P_{on}(r+\Delta r)}\right). \tag{2.5}$$

The key advantage of the DIAL technique is a self-calibration feature: Eq. 2.4 does not include any instrumental constant as well as no *apriori* information on backscatter and extinction coefficients of atmospheric constituents. Difference in energies of the generated online and offline pulses does not influence the result neither. By proper selection of working wavelengths the temperature sensitivity of the absorption cross-section $\sigma(v_{on,off},T)$ is minimized and its spectrum can be estimated with a low uncertainty using HITRAN and ESA databases [HITRAN, 2005; ESA, 2000]. Hence, the DIAL technique obtains measurements of atmospheric water vapor with a high temporal and spatial resolution [Wulfmeyer, 1998; Wulfmeyer and Bösenberg, 1998; Wulfmeyer, 1999a,b; Behrendt et al., 2007a,b].

Having SNR of the elastic backscattered signal three order of magnitude higher than for the Raman signal, DIAL appears to be the only available choice for the reference water-vapor remote sensing system [Wulfmeyer et al., 2006].

2.2 System requirements

In contrast to the Raman lidar, the most stringent requirements in the DIAL system are applied not to the receiver but to the transmitter part [Ismail and Browell, 1989; Wulfmeyer, 1998]. In the recent time an extensive work was made to formalize the requirements for a reference water-vapor DIAL system, deployed on a ground-based and airborne platform [Bösenberg, 1998; Wulfmeyer, 1998; Wulfmeyer and Bösenberg, 1998; Wulfmeyer and Walter, 2001a,b; Petrova-Mayor et al., 2008]. To obtain measurements of water vapor with an overall instrumental error $< 5\%$, the laser transmitter must fulfill the following specifications (see Table 2.1).

Table 2.1 Summary of the requirements for the laser transmitter of the reference water-vapor DIAL. Here FWHM – full width at half maximum.

Parameter	Ground-based (within boundary layer)	Airborne and space borne
1. Wavelength, nm	730, 820, 935, 1450	
2. Average power, W	> 10	
3. Pulse energy, mJ	$> 40 - 10$	
4. Repetition rate, Hz	$250 - 1000$	
5. Pulse duration, ns	< 200	
6. Pulse linewidth, FWHM MHz	< 400	< 160
7. Frequency stability, MHz 1σ	< 200	< 60
8. Spectral purity, %	> 99.5	>99.7
9. Energy instability, % 1σ	< 4	
10. Tunability, GHz	± 10	
11. Beam quality, M^2	< 2	
12. Depolarization ratio, %	< 1	
13. Pointing instability, μrad 1σ	15	

In the following sections a brief discussion on the specifications is given.

1. Choosing the working wavelength region, the following conditions have to be concerned [Wulfmeyer and Walter, 2001a]:

- wavelength dependence of the atmospheric backscatter and extinction coefficients. A longer wavelength corresponds a smaller values of these coefficients with a ratio $1/\lambda^4$ for molecules and $1/\lambda$ for particles;

- wavelength dependence of the atmospheric background signal. For daytime measurements a strong short-wavelength background from the solar radiation has to be considered. Nevertheless, in the near IR region narrow-band filters can be used to decrease the background emission to an acceptable level. Hence, the working absorption lines are located in the wavelength range 700 – 1500 nm;

- presence of suitable water-vapor lines. The optimum detection is achieved when for the given spatial resolution of measurements Δr, the water-vapor absorption coefficient within a single cell is $\alpha = 0.03\ldots0.1$ with a total optical thickness along the measured profile $\tau \lesssim 1$. Thus, for scanning measurements with a ground-based DIAL, the weaker lines for horizontal profiling has to be preferred, whereas for the vertical profiling the stronger ones has to be chosen. The optimal deployment of a line is restricted to certain range of partial pressure of water vapor, hence certain atmospheric conditions. To neglect temperature dependence of the absorption cross-section in calculations, the water-vapor lines with a lower-state energy $E'' < 300\ \text{cm}^{-1}$ has to be preferred. Furthermore, to minimize the calculation uncertainty, the ratio of the online and offline absorption cross-sections has to be $\gtrsim 100$;

- availability of detectors with a high SNR, a low dark current and linear response on the optical signal within a range $> 80\ \text{dB}$ for an optimum detectivity over the whole measured profile. Avalanche photodetectors were considered fitting these specifications, having an advantage to photomultipliers in less "ringing" after reaching the saturation value. This eliminates a systematic error in the presence of clouds;

- availability of laser mediums, obtaining a high average power, a high pulse energy output and a high wall-plug efficiency in the preferred wavelength region;

- eye safety. Regarding [ANSI, 1986] and simulations from [Wulfmeyer and Walter, 2001a], acceptable wavelength regions for eye-safe lidar measurements locates below ~400 nm and above ~1400 nm. To assure an eye-friendly operation outside these regions, the designed DIAL has to be accomplished with a safety radar.

2-3. Essential characteristics are the pulse energy and the average power. End-to-end performance analyses show that the SNR of the lidar backscatter signal has to be > 3 for a single laser shot in a single range bin [Wulfmeyer and Walter, 2001a].

4. A high repetition-rate of the transmitter is essential to realize 3-d measurements of the water-vapor distribution with a high temporal and spatial resolution. This is particularly required for observations of convection and turbulent processes in the atmosphere.

5. A pulse duration of 200 ns defines a minimum spatial resolution of 30 m. End-to-end performance models demonstrate that this spatial resolution is essential to remove bias sources in the retrieval of water-vapor profiles. Typically, laser pulses have length of 20…50 ns. This parameter does not influence the designing of the transmitter.

6.-8. The spectral properties of the laser are the most demanding and stringent requirements for the transmitter. These have been extensively discussed in [Bösenberg, 1998; Wulfmeyer, 1998; Wulfmeyer and Bösenberg, 1998]. The system should fit the given specifications to obtain water-vapor measurements with a transmitter caused uncertainty $< 5\,\%$. The values of bandwidth, frequency stability and spectral purity are set to obtain their individual uncertainties $< 3\,\%$. The requirements for the linewidth and the frequency stability are mainly governed by a spectral narrowing of the water-vapor absorption cross-section, when the maximum width of the absorption line varies from $\approx 4\,\text{GHz}$ at the ground level down to $1\text{-}2\,\text{GHz}$ in the upper troposphere. Thus, the operation of a laser transmitter has to be limited to one or two longitudinal modes, employing sophisticated frequency stabilization techniques. The requirements applied to the spectral purity (SP) allow for minimizing the bias in regions with a high water-vapor optical thickness. The SP is defined as a fraction of the intensity spectrum of the laser emission within the specified bandwidth.

9. The specified value of the shot-to-shot energy stability minimizes systematic errors in the water-vapor retrieval with the DIAL technique.

10. The tunability of the transmitter frequency allows for optimizing the system performance in highly variable atmospheric constitutions. The given value of 10 GHz is applied to 'on the fly' tuning of the laser, e.g., when switched from vertical to horizontal profiling. Furthermore, an additional coarse tuning within a whole set of water-vapor absorption lines is required to shift from a strong absorption line to a weak one to decrease signal absorption in a near range.

11. A low M^2 allows to operate the system with a narrow FOV, which is of essential importance for daytime measurements.

12.-13. The depolarization ratio and the pointing stability are not considered as critical parameters, but their specifications are required for designing the laser transmitter. Nevertheless, it has to be verified that the ratio of the angular jitter of the laser beam in the FOV of the telescope to the size of FOV is < 1/10.

2.3 Currently available high-power systems

The first DIAL system was reported by [Schotland, 1966] and was intended for the water-vapor profiling of the atmosphere. The set-up of the transmitter was based on two flash-lamp pumped ruby lasers, temperature-tuned to the 'online' and 'offline' wavelengths of the water-vapor absorption in the vicinity of 694.3 nm. Ground-based measurements were performed up to the heights of 1-2 km with a spatial resolution of 100 m and temporal resolution around an hour. Values of linewidth and frequency stability were specified to be ≈ 5 GHz.

Later for transmitters of water-vapor DIAL systems were implemented CO_2-lasers working in the 10 μm wavelength region [Zuev et al., 1983], and pumped dye lasers emitting in the near-IR, at 0.7 μm [Cahen et al., 1982]. An airborne system was reported [Ehret et al., 1993]. These transmitters had reasonable pulse energies and higher repetition rates, e.g. 70 mJ and 10 Hz, with a bandwidths of ~1 GHz, achieved with intra-cavity etalons. These systems provided data with a statistical error of 10% and 4 min/60-120 m tempo-spatial resolution up to the height of 3 km for ground-based measurements. To obtain the measurement sensitivity of the water-vapor mixing ratio of approximately 0.01 g/kg for airborne profiling in the upper troposphere (8200 m), where the ambient values range between 0.03 and 0.2 g/kg, an averaging over 200 shot pairs was necessary [Ehret et al., 1993]. At the repetition rate of the double pulses of 3 Hz and the aircraft speed of 180 m/s, for the chosen vertical resolution of 300 m this averaging yields an 11 km horizontal resolution.

To decrease the transmitter size and increase its 'wall-plug' efficiency, especially critical for airborne devices, development of transmitters on solid-state active mediums was initiated. An airborne flash-lamp pumped Alexandrite-laser has been designed at CNRS (Centre National de la Recherche Scientifique) in Paris, France as a part of LEANDRE II system (Lidar pour l'Etude des interactions Aérosols Nuages Dynamique Rayonnement et du cycle de l'Eau) [Bruneau et al., 1991; Bruneau et al., 2001a,b]. This system operates in the wavelength region of 730-770 nm in

a double-pulse mode with a pulse delay of 50 µs and a repetition rate of 10 Hz. A single-shot pulse energy of 50 mJ was achieved. A bandwidth of 700 MHz and a spectral purity of 99.99% were obtained using intra-cavity etalons. The lasing frequency was defined with an uncertainty < 150 MHz.

The next breakthrough in the transmitter development was achieved with implementation of an injection seeding (IS) technique, when a weak cw laser defines the spectral properties of the pulsed laser [Barnes and Barnes, 1993; Barnes et al., 1993; Bruneau et al., 1994]. Application of IS drastically improved the bandwidth, frequency stability and, especially, spectral purity of transmitters (for more details see Subsection 4.1.2).

The first transmitter, where all the advantages of the seeding technique were implemented and which was verified for the total instrumental error < 5%, was developed as a part of a ground-based water-vapor and temperature DIAL at MPI (Max Planck Institute of Meteorology) in Hamburg [Wulfmeyer and Bösenberg, 1994; Wulfmeyer et al., 1995; Wulfmeyer, 1998]. An Argon-laser pumped cw Ti:sapphire (TISA) laser was applied for injection seeding of a ring-cavity flash-lamp pumped Alexandrite-laser, emitting at 725 nm for water-vapor and at 770 nm for temperature measurements. A pulse energy of 50 mJ at a repetition rate of 20 Hz with a linewidth < 160 MHz, a frequency stability < 43 MHz 1σ and a spectral purity > 99.99% was demonstrated during long-term tests as well as in following field campaigns.

As the first step for developing a space borne DIAL, a system was designed in NASA (National Aeronautics and Space Administration) as a part of LASE (Lidar Atmospheric Sensing Experiment) [Browell et al., 1996] for autonomous operation on research aircrafts [Browell et al., 1998; Ismail et al., 2008]. LASE is based on a flash-lamp pumped Nd:YAG laser used to pump a linear-resonator injection-seeded TISA laser, emitting at 815 nm. The transmitter operates in a double-shot mode with a pulse delay of 200-400 µs at a repetition rate of 5 Hz. A single-shot pulse energy of this system is 100-150 mJ with a bandwidth < 120 MHz, a frequency stability < 190 MHz and a spectral purity > 99%. Typical water-vapor measurements obtained with this system have 300-500 m vertical and 30 s temporal resolution. Starting from 1995, this DIAL participated a numerous measurement campaigns, e.g. SGP97 (Southern Great Plains 1997 Experiment), IHOP2002 (The International H2O Project).

In the last years several water-vapor DIAL systems based on high-power transmitters were reported. An airborne DIAL was designed in DLR Obepfaffenhofen within WALES project (Water Vapour Lidar Experiment in Space) [Wirth et al., 2009], as a further development of their

previous system of a similar set-up [Poberaj et al., 2002]. The transmitter is based on a Nd:YAG-pumped injection-seeded optical parametric oscillator (OPO), operating at 920-940 nm. The laser alternates between two wavelengths at a rate of 100 Hz. There are two identical laser systems operating temporally interleaved, producing a four-pulse train at four wavelengths with a total repetition rate of 50 Hz. The obtained output energy is 45 mJ per pulse, characterized with a bandwidth < 120 MHz, a frequency stability < 15 MHz and a spectral purity > 99.9%. It is the first airborne system, allowing the coverage from the lower stratosphere to the ground with an error ~10% (the exact value is still to be defined). The first deployment of the system was performed in 2007.

A new laser for DIAL was developed at MPI in the last years [Ertel et al., 2005]. The transmitter is based on an injection seeded ring-resonator TISA laser, pumped with a frequency doubled Nd:YAG laser. Two external-cavity diode lasers were implemented for seeding operation at online and offline wavelengths, respectively. The laser alternates between online and offline on a pulse-to-pulse base at a rate of 50 Hz. An output pulse energy is 18 mJ at 817 nm. Applying a novel injection locking technique, a spectral purity > 99.95% was achieved. A pulse bandwidth is 22 MHz.

Another ground-based DIAL system was designed at RLC (Research Center Karlsruhe, formerly Fraunhofer Institute) [Vogelmann and Trickl, 2008]. The transmitter utilizes an injection-seeded pulsed Nd:YAG laser, used to pump two OPO converters, whose output is coupled in a flash-lamp pumped TISA regenerative amplifier. For the lidar operation, typical energies are around 150 mJ at 817 nm at a rate of 20 Hz, alternating between two wavelengths. The specification of the transmitter was performed for the OPO systems with output energies of ≈ 0.5 mJ each, a bandwidth of 130-250 MHz (depending on the pulse length of the Nd:YAG), and a frequency stability < 35 MHz. A spectral purity > 99.9% was specified at 852.333 nm using a caesium absorption cell. The DIAL operates at the Schneefernerhaus high-altitude research station (2675m asl, Zugspitze, Germany). Measurements were performed with a temporal resolution of 1000 s and a vertical resolution of 53-210 m in a near- and far-field (7200 m), respectively.

In the given overview the observation was focused on high-power transmitters. However, it is worth to mention water-vapor DIAL systems with diode lasers as transmitters [Hamilton et al., 2008]. Their advantages are compact design, a high 'wall-plug' efficiency and simple construction. To obtain pulse operation, the cw output of the transmitter is modulated with an amplitude modulator (usually, an acousto-optical). Using external-cavity diode lasers (ECDL),

Table 2.2 Specification of transmitters of existing water-vapor DIALs.

Parameter	Ground-based			Airborne			
	MPI95	MPI05	RCK	DLR93	LASE	LEANDRE	WALES
Wavelength, nm	720-780	810-825	800-860	720	815	730-770	935
Pulse energy, mJ	50	15	150[1]	30-40	100-150	50	45
Repetition rate, Hz	20	50	20[1]	10	5, dp	10, dp	200
Linewidth, MHz	160	22	130-250[1]	450	120	700	120
Frequency stability, 1σ MHz	43	–	35[1]	300	190	150	15
Spectral purity, %	99.99	99.95	99.9[2]	75	99	99.99	99.9

dp – double-pulse; 1) specified before regenerative amplifier; 2) specified at 852.333 nm

a high accuracy of spectral properties of the laser emission can be achieved. With a frequency stability of 88 MHz, a linewidth of 300 kHz and a spectral purity $> 99.5\%$ the transmitter is verified for an instrumental error $< 3\%$ for measurements within boundary layer [Nehrir et al., 2008]. Nevertheless, the maximum output power after two tapered amplifiers of 500 mW cw restricts the tempo-spatial resolution of the water-vapor measurement to 60 min and 150 m, respectively.

2.4 Transmitter selection

From the presented water-vapor DIALs only the WALES at DLR Oberpfaffenhofen fulfils the requirements for the reference system, as it was specified in the Table 2.1. However, on the start of the current project that transmitter was not available. The ground-based system from MPI is also suitable for the accurate measurements, but the low repetition rate restricts its implementation in the scanning mode.

Deciding for the transmitter of the water-vapor DIAL, an option with a pump laser and a frequency converter was preferred. The latter was selected from Raman crystal, OPO and TISA. They all require a diode-pumped Nd(Yb):YAG (YLF) laser, whose final selection can be made later.

As far as we were unaware of any high-power Raman-crystal operation, this material did not fit the requirements. Both TISA and OPO have their advantages, but on the start of the project it
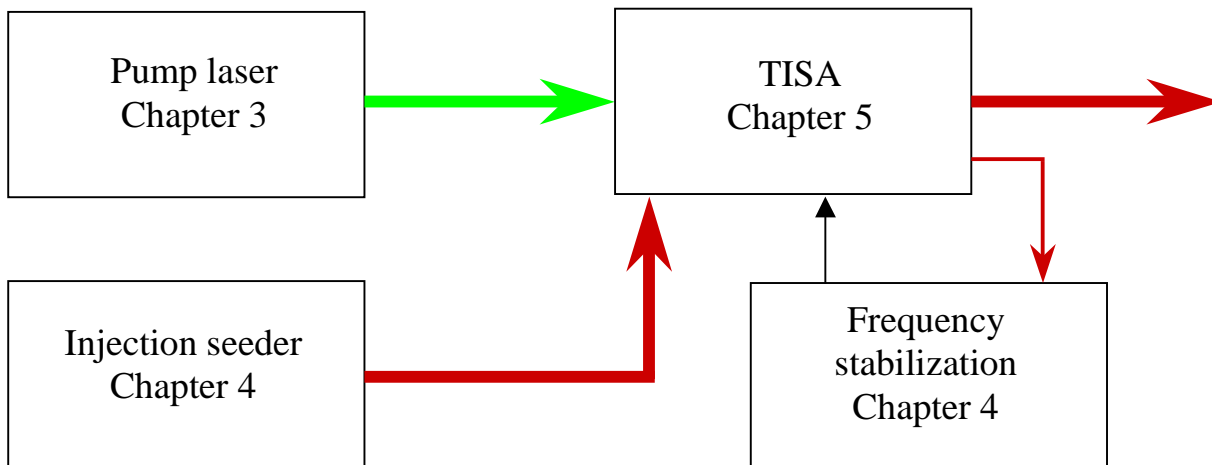
Fig.2.2 Principal scheme of the transmitter for the water-vapor DIAL.

was not clear, whether OPO can stand an average power of > 10 W, whereas TISA is the well known material for high-power applications [Yamakawa, 2000; Zavelani-Rossi, 2000]. The beam quality of OPO characterized by a typical value of $M^2 > 5$ was the other limiting factor. Having in the working group an expertise of developing TISA and alexandrite lasers, TISA was preferred for the laser medium.

Figure 2.2 depicts the principal layout of the DIAL transmitter, composed from a pump laser (see Chapter 3) and a TISA laser, operating at 935 nm and at 820 nm for airborne and ground-based measurements, respectively (see Chapter 5). For the fine spectral selection, the injection seeding technique together with stabilization of the TISA cavity was applied (see Chapter 4).

Chapter 3

Pump laser

3.1 Introduction

To fulfill the requirements for a ground-based, airborne and space borne water vapor DIALs, summarized in the Table 2.1, the source laser for pumping the TISA converter must obtain the following specifications:

- a high overall efficiency and compact design to operate in the field;

- a high pulse energy (~ 200 mJ);

- a high repetition rate (> 250 Hz) for scanning applications;

- an excellent beam quality to optimize pumping and to avoid hot spots in the beam profile;

- optional single-frequency operation for future applications such as pumping OPO-systems (not applied in this experiment).

On the beginning of this work we were unaware of any commercially available system fitting this specification. Therefore, within a collaboration of the University of Potsdam and the company IB Laser AG such a laser was designed and manufactured [Ostermeyer et al., 2005]. The staff of IPM (Institute of Physics and Meteorology) at UHOH (Hohenheim University) was involved in the optical design of the transmitter and proper assembling of the components, final specification and the following routine maintenance of the system,.

Fig. 3.1 Set-up of the pump laser. IS – Injection seeder (P~50 mW, waist radius w_{horis}=0.222 mm, w_{vert}=0.226 mm, waist location – –45 mm from output surface of laser), MO – master oscillator, preA – pre-amplifier, postA – post-amplifier, FI – Faraday isolator, EOM – electro-optical phase modulator, F1-F8 – lenses, HR – high-reflecting mirror, PR – partially-reflecting mirror (R=90%), HR99 – a resonator mirror (R=99%) glued on a piezo actuator, YAG1-YAG5 - pump chambers, PC – Pockels cell (2xRTP crystals), TFP – thin-film polarizer, OC – output coupler (R=70%, radius of curvature +3 m), QR – quarz rotator, 90°, SHG – second harmonic generator (2xLBO crystals, 10x10x15 mm, 20°C), DM – dichroic mirror (HR532AR1064/AR1064), A1 – aperture (∅1.5 mm), A2 - water-cooled aperture (∅7 mm), W – window (AR/AR 532/1064), Det – InGaAs photodetector (Thorlabs, 410). Focal lengths of the lenses (mm): F3 – 400, F4 – –300, F5 - –150, F6 – 1000, F7 – –100, F8 – 150. Axial distances (mm): a = 412, b = 284. Size of the Nd:YAG rods (mm): YAG1 – ∅3x50, 0.4% doped, YAG2 and YAG3 – ∅3x90, 0.8% doped, YAG4 and YAG5 – ∅8x93, 0.6% or 0.4% doped (see Table 3.1).

Fig.3.2. Layout of the pump laser corresponding the scheme 3.1, used without IS for this work. The size of the breadboard is 120x60 cm.

3.2 System layout

The combination of the requirements, – such as a robust setup, high pulse energies, a high repetition rate, single-frequency operation, a good beam quality, – led to a Master Oscillate Power Amplifier (MOPA) architecture. For the active medium the Nd:YAG crystals were chosen. A transversal rod pumping using laser diodes was preferred to improve stability and efficiency of operation and to ease cooling of the crystals. For the pump diodes, the bars "ProLight Monsoon" MMO-808-050 from Spectra-Physics and LB-80A01-60QCW-270W from Monochrome were used (see Table 3.1). The principle scheme and the layout of the laser are depicted on Figs. 3.1 and 3.2, respectively.

3.2.1 Resonator

In the oscillator, a Nd:YAG rod (3 mm diameter, 50 mm length, 0.9% doping level) is used. The crystal is pumped transversely with six diode bars ProLight Monsoon, arranged in a threefold geometry around the laser rod (see Fig.3.3).

The pump pulse of the diodes has a length of 300 µs, obtaining an average pump power of 56 W with a corresponding thermal lens focal length value of $f = 1.71$ m. The beam radius of the eigenmode in the rod amounts to 0.6 mm. To verify the TEM_{00} operation, an aperture with a diameter of 1.5 mm was incorporated in the laser cavity. A twisted-mode arrangement with two
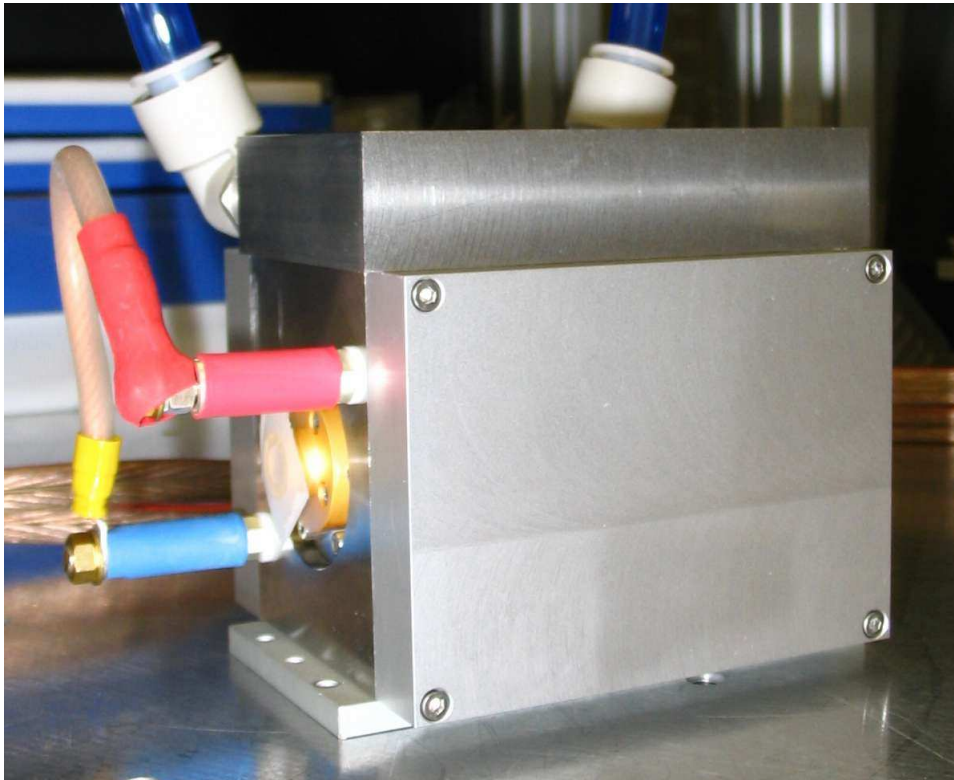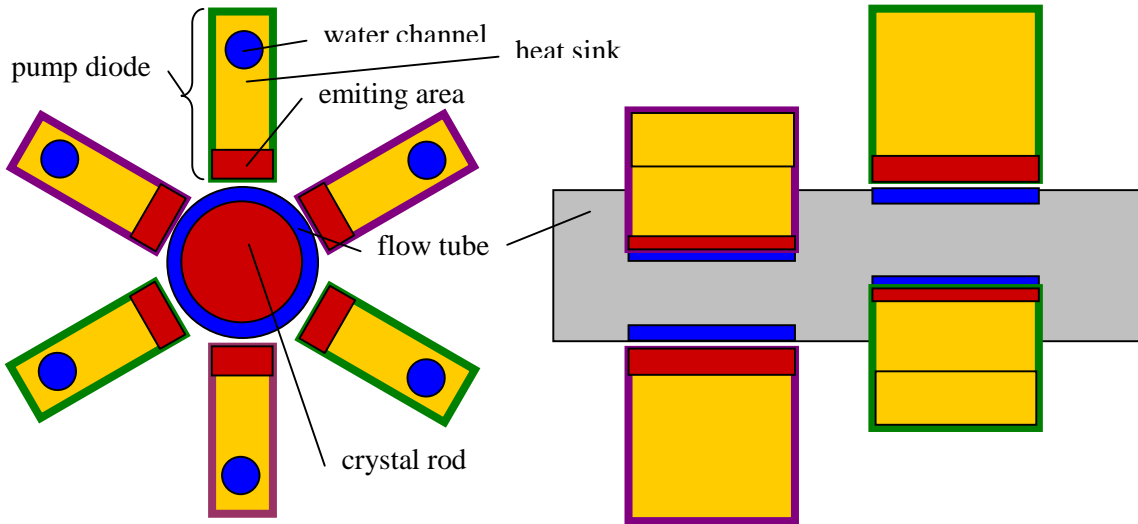
Fig.3.3 Principle scheme of the transversal pumping technique applied in the MO pump chamber (upper panel). The Nd:YAG rod is mounted inside a tube with an AR-coating on the inner side. The space between tube and crystal is filled with flowing water for heat removal. Six pump diodes in the threefold geometry form two 'stars' (diodes in the first marked violet, in the second green) and pump the rod through windows in the flowing tube. The heat sinks of the diodes are water-cooled as well. On the photo of the pump chamber (lower panel) electric contacts are shortened to protect pump diodes from static electricity. The aperture of the crystal is covered to prevent dust contamination on the end-surface of the rod. The outer dimensions are 7×5×7 cm as L×W×H.
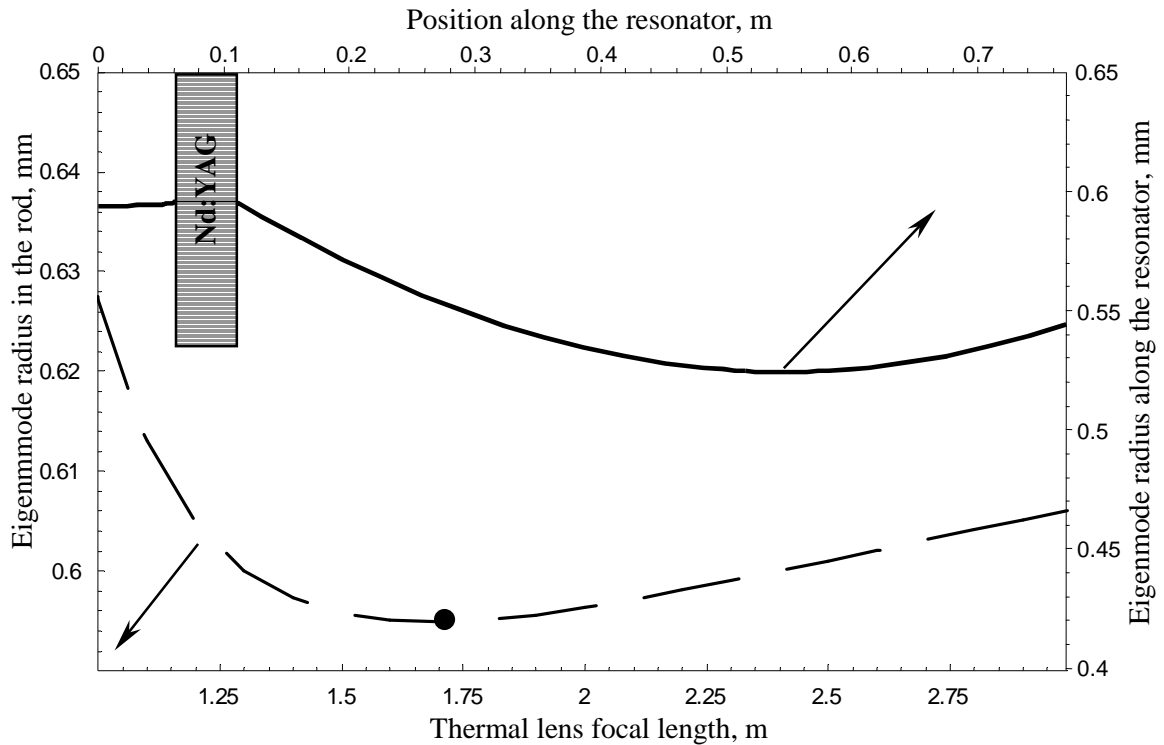
Fig.3.4 Calculated stability zone of the MO, the eigenmode size in the rod as a function of the thermal lens focal length (dashed curve), and the eigenmode size along the resonator, starting at the back HR mirror (solid curve) . Current thermal lens focal length value is marked with a circle.

quarter-wave plates before and after the laser rod was implemented to prevent spatial hole burning, thus increasing the lasing efficiency and removing the obstacle for the single-frequency operation. The oscillator is Q-switched by an RTP (Rubidium Titanyl Phosphate) Pockels-cell.

The back highly-reflective (HR) mirror is flat and has a reflectivity of 99% allowing for coupling of the seeding photons in the cavity. The calculations of the resonator design were performed using a matrix formalism, similar as in [Wulfmeyer, 1998; Wulfmeyer et al., 2000] (see Eqs.5.6-5.8). Taking into account the requirement of resonator dynamical stability, compromising between size of the eigenmode volume in the rod and misalignment sensitivity of the cavity and obtaining a pulse length of > 20 ns to prevent components of the MO and following amplifier stages from optical damage, a 770 mm long cavity was chosen. An output coupler (OC) was calculated to have a radius of curvature of 3 m with a reflectivity of 70%. Figure 3.4 depicts a resonator stability zone, – a range of the thermal lens values corresponding minimal fluctuations of the eigenmode size in the rod, – and the eigenmode radius along the laser cavity.

M^2	1.14/1.15
Astig.	0.07
Asym.	1.02
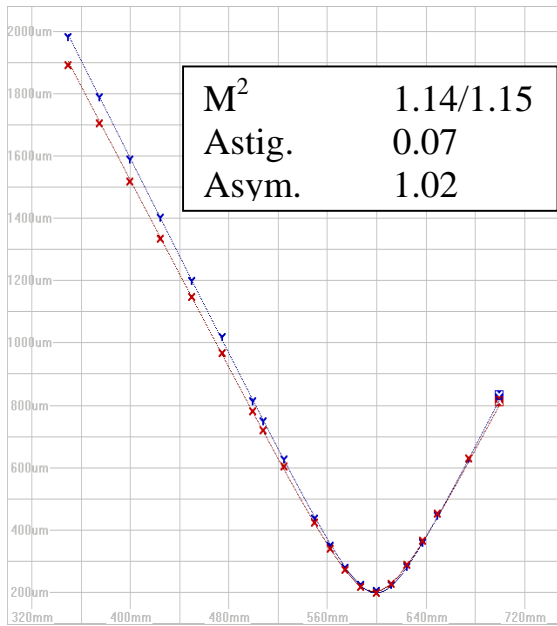
Fig.3.5 M^2-measurment of the MO beam in the horizontal (x, red) and vertical (y, blue) planes.

1 mm
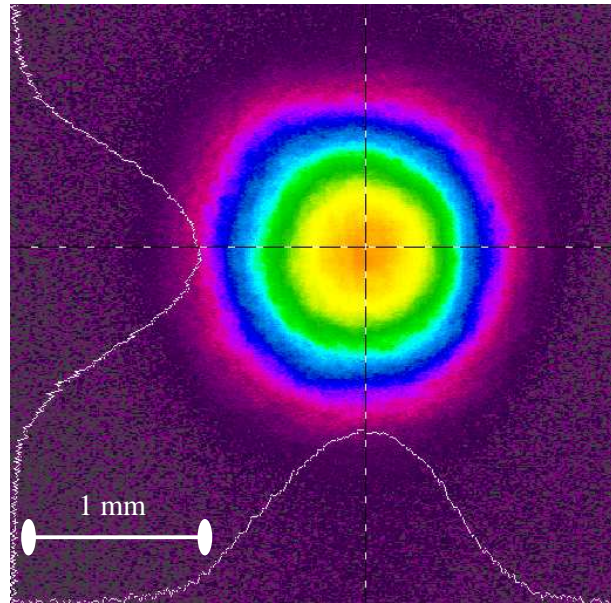
Fig.3.6 Profile of the laser beam after the MO.

These calculations as well as all the further ones for the pump laser were performed at IPM. Assembling of the Nd:YAG, namely, the MO, a pre-amplifier, a post-amplifier, and a second harmonic generator, and its iterative optimization were accomplished within a cooperation of IPM and IB Laser.

The output beam of the MO is linear polarized with a purity of $> 99\%$. The beam parameters in a horizontal/vertical direction have the following specifications: a near-gaussian profile, $M^2 = 1.14/1.15$, astigmatism 0.07, asymmetry 1.02 (see Fig.3.5). The measurement was performed with a Spiricon M2-200 device using a D4σ-method [ISO 11146-1, 2005] during assembling of the system. The output pulse energy yields 11 mJ. A beam profile recorded with a CCD-camera Spiricon TM6 is shown on the Fig. 3.6.

The injection seeder of the pump laser is a monolithic Nd:YAG cw ring-laser (Innolight "Mephisto") with an output power of 50 mW, protected from the back reflex with a Faraday isolator (FI). The seeder beam propagates through an electro-optical phase modulator (EOM) as a part of a stabilization system and lenses F1 and F2 to match the intra-cavity eigenmode. The desired polarization orientation is obtained with a halfwave plate (see Fig.3.1). Currently, no injection-seeding operation is applied.

3.2.2 Amplifiers

Pump chambers of amplifiers are assembled in two pairs for a pre-amplifier and a post-amplifier. Each pump chamber of the pre-amplifier includes a Nd:YAG rod (diameter 3 mm, length 90 mm, doping level of 0.8%) pumped by 12 diode bars (ProLight Monsoon) in a threefold geometry with an optimum pump pulse duration of 224 μs. This yields an average optical pump power of 92 W per pump chamber. To prevent parasitic lasing in the amplifiers, all rods have a 0.3° wedge. To isolate the MO from occasionally contra-propagating light from the amplifiers which could disturb the evolution of the laser pulse, a Faraday isolator was applied.

For an effective compensation of thermally induced phase distortions and a birefringence in the crystals, the following technique was applied [Hodgson, 1996, p.295; Konno et al., 1997; Sträßer et al., 2007]. The lens combination in front of the pre-amplifier shapes the output of the MO, yielding a symmetric propagation of the TEM_{00} through the pump chambers. The beam, set divergent in front of the pre-amplifier, is collimated by the thermal lens in the first pump chamber. Furthermore, the waist of the collimated beam locates in the center of the optical path between the rods. The thermal lens in the second pump chamber, identical to the thermal lens in the first pump chamber, converges the laser mode symmetrically to the input of the amplifier. To compensate the induced birefringence, a 90° optical rotator was mounted between the chambers [Koechner, 1996, p.409].

Measurements of thermal lens focal lengths in the pump chambers of the MO and the amplifiers were performed in IB Laser. The technique is similar to one applied by [Koechner, 1970]. A pump chamber is mounted in a plane resonator close to one of the mirrors, so that a distance to the other mirror is an order of magnitude longer. Increasing pump power of the diode bars, the corresponding growth of the output energy of this laser is observed until a fast power drop. At the peak of the output power the cavity configuration is equivalent to a semi-confocal resonator, hence, value of the focal length of the thermal lens equals the double resonator length. Drop of the output power with the further pump increase is caused by shifting of the resonator out of its stability zone. Applying different cavity lengths, a functional dependence between the pump power and the strength of the thermal lens can be defined.

To optimize the parameters of the beam shapers (optical power, position regarding the pump chambers), a CAD-program ZEMAX was implemented. Applying results of the thermal lens measurement in Nd:YAG crystals, the optical layout of the laser was modeled using ZEMAX. The rods with thermally induced lens were described as gradient mediums with parabolic

dependence of the refraction index [Koechner, 1996, p.400; Wagner et al., 2005]. Modeling a propagation of the laser beam from the MO, parameters of the beam shapers were defined. The optimization was performed regarding the aforementioned requirement of the symmetric pump-chamber propagation with a size of the eigenmode in the rods as a boundary condition. The beam diameter had to be in a range limited by the crystal aperture from top and by damage threshold of the Nd:YAG from bottom.

When MO was assembled, the first beam shaper (lenses F3 and F4 on Fig. 3.1) and the pre-amplifier were mounted on the breadboard of the laser system. The spatial parameters of the laser beam behind the MO, the beam shaper and the pump-chambers of the pre-amplifier were characterized with the Spiricon M2-200 device to find a discrepancy with the model. When the real beam propagation after the pre-amplifier did not fit the calculated one, the program parameters were corrected to remove this deviation. The first beam shaper was recalculated regarding the changed conditions, the layout was modified and the beam parameters were checked again.

Such an iteration was repeated until the parameters of the real laser beam after the pre-amplifier matched the model with an error, limited by a measurement uncertainty. The measurement errors were caused by residual non-zero astigmatism and spatially inhomogeneous phase distortions of the mode cross-section. It was not possible to eliminate these imperfections completely due to a distinction between the thermal lenses in the pump chambers and alignment uncertainties. Thus, the symmetrical propagation of the real beam through the pre-amplifier with identical thermal lenses in its pump chambers was verified. Modeling of the next beam-shaper (lenses F5 and F6) and assembling of the post-amplifier was performed regarding the same procedure, using the laser beam after the pre-amplifier as a reference one.

For the experiment with the TISA laser, the pump laser was used in two different configurations. The distinction was due to a type of the post-amplifier. In a first configuration (Pump-1), the post-amplifier with 36 pump diodes "Prolight Monsoon" per pump chamber in a six-fold geometry was deployed [Ostermeyer et al., 2005]. For a pump pulse duration of 300 μs, an average pump power of the diodes was 345 W per pump chamber. The Nd:YAG rods had a diameter of 8 mm, a length of 93 mm and a doping level of 0.6%.

Later these pump chambers were replaced to increase the output of the laser, and the experiment was continued with a second configuration of the pump laser (Pump-2). The post-amplifier pump chambers were modified to deploy 32 more powerful diode bars "Monochrome" each, assembled

in an eight-fold geometry. For a pump pulse duration of 257 μs an average pump power of the diodes was 450 W per pump chamber. The geometry of the rods was preserved, doping level was decreased to 0.4%. For specifications of the laser see Table 3.1.

3.2.3 Output energy control

Propagation of the laser beam through the amplifiers in a MOPA configuration is prone to the thermal lensing in the crystals. Steering of the repetition rate or the pump pulse energy will cause deviation of the beam propagation, yielding a drop of the output power and a severe change of the spatial properties of the outgoing beam. Hence, these usual techniques can not be implemented in the pump laser for a smooth tuning of the output power.

For such a fine control, tuning of a Q-switch delay in the MO and of a fire delay of the pump-diodes in the amplifier stages was implemented. It works as follows: in a stand-by state, all pump chambers in the MO and the amplifiers are powered and diode bars pump the crystals, forming quasi-stable thermal lenses. The Q-switch is delayed, so that the energy stored in the Nd:YAG crystal of the MO is decayed with spontaneous transitions. No lasing is possible. Shifting the delay value from the lasing threshold at 350 μs to the maximum output of 11 mJ at 12 μs, the pulse energy of the MO can be controlled with a 1 μs step for a fine output adjustment. With this technique, the thermal load of the rods stays constant and the spatial properties of the MO emission are preserved for the whole range of the output energy.

The amplification in the amplifier stages is controlled regarding the same scheme: in a steady-state condition the pump diodes are delayed regarding the Q-switch of the MO and no amplification of the master-pulse is performed. Decreasing the delay, a temporal overlap between pulses of the pump diodes and the propagating laser emission is increasing. The amplification starts. For the amplifiers the same 1 μs minimal tuning step can be used, obtaining a fine tune of the output.

Although this technique preserves the beam parameters, typically some short- and long-term fluctuations of the spatial characteristic of the laser emission may be expected. This is caused, likely, by the thermal effects: heating of the crystals of the pump chambers, the Q-switch, the Faraday rotator and the quartz rotators. For a stable operation of the laser, some warm-up time is optionally required. For further details see Subsection 3.3.2.

3.2.4 Second harmonic generation

The wavelength of the pump source has to be tuned to the vicinity of the absorption maximum of TISA at 514 nm. Using a second harmonic generation (SHG) technique, approx. a half of the

output energy of the pump laser at 1064 nm is converted to 532 nm. Here the absorption cross-section of the TISA amounts 80% from maximum [Moulton, 1986].

In the pump laser an SHG-converter comprises two identical Lithium triborate (LBO) crystals with a square aperture of 10 mm and a length of 15 mm, mounted regarding a "walk-off" compensation scheme [Boyd and Kleinman, 1968]. The lens combination after the post-amplifier (lenses F7 and F8, see Fig.3.1) adjusts the parameters of the laser beam to obtain its symmetrical propagation through the frequency doubler and a homogeneous energy density distribution on the crystal surfaces. Due to a residual absorption in the crystals, the converter builds a weak thermal lens at high power levels. The optimization of the beam shaper was performed implementing the same technique as for the amplifiers.

The phase-matching condition in non-linear optical materials has a severe temperature sensitivity [Hodgson, 1996, p.575]. Hence, the SHG-cluster was mounted on Peltier-elements, whose other side was put in contact with a water-cooled heat sink. A temperature sensor and an automatic driver perform dynamic temperature stabilization with a precision of few hundreds of Kelvin. To prevent adsorption of water vapor on the LBO end-surfaces, the crystal set was sealed in a plastic case with an input and output windows and a build-in replaceable water absorber.

To prevent occasional damage of the crystals on their edges by the propagating beam, a water-cooled aperture was placed between the last lens combination and the SHG. A halfwave plate was mounted in front of the SHG-converter, obtaining an option to adjust the frequency-doubling conversion efficiency from the maximal 50% to 0%. This feature is valuable for further operation of the pump laser at the original wavelength of 1064 nm with other active mediums, e.g., OPO, Er:YAG.

3.3 Pump laser specification

3.3.1 Output power and beam quality

The parameters of the pump laser were fully specified before the experiment with the TISA laser. The pump laser was deployed in two configurations, Pump-1 and Pump-2, with different post-amplifiers, hence, different output powers and beam qualities (see Table 3.1). In this table values of the output power and the pulse energy at 1064 nm are given for the case when the halfwave plate in front of the SHG is tuned to provide minimum conversion into green. At the maximum conversion efficiency the IR output is about 50%.

3.3 Pump laser specification

Table 3.1 Pump laser specification, pump diodes specification. Here FWHM – full width on a half maximum, SP – Spectra-Physics, Mon – Monochrome.

Parameter	Pump-1	Pump-2
Wavelength, nm	1064/532	1064/532
Repetition rate, Hz	250	250
Pulse energy after SHG, mJ and type of pump diodes – max MO – max pre-amplifier – max post-amplifier (full output)	9@1064 nm, 1@532 nm (SP) 70@1064 nm, 13@532 nm (SP) 220@1064 nm 108@532 nm (SP)	384@1064 nm 184@532 nm (Mon)
Output power (max), W	55@1064 nm 27@532 nm	96@1064 nm 46@532 nm
Pulse duration (FWHM), ns	20	19
M^2 for horizontal/ vertical cross-section	2.1/2.4@532 nm	3.1/3.1@1064 nm 3.9/4.3@532 nm
Optical conversion efficiency at 1064 nm	5.9%	8.4%
Pump diodes		
	Spectra-Physics MMO-808-50	Monochrome LB-80A01-60QCW-270W
Wavelength, nm	808±3	808±3
Output power, W cw	50	270
Maximum duty cycle	10 %	10 %
Size of active aria (L×H)	10 mm × 1 µm	10 mm × 1 µm
Divergence (FWHM)	38° × 7°	30° × 10°

With modernisation of the pump laser from the Pump-1 to the Pump-2, the power and the pulse energy were almost doubled, but a beam quality at 1064 nm as well as at 532 nm decreased (see also Fig.3.7-3.9). The major part of the spatial distortions is produced by the pre-amplifier. Small number of pump diodes (12) and not-optimized construction of the pump chambers failed to provide a required homogeneity of the illumination of a ⌀4 mm Nd:YAG rod. To improve the illumination pattern, the ⌀4 mm rods were replaced with ⌀3 mm ones. To obtain the similar amplification ratio in the smaller volume of the active medium, the pump power of the diodes was intensified, increasing thermally-induced distortions of the amplified laser beam. However, it was decided to keep the ⌀3 mm rods, because this design provides a better beam quality. These pump chambers were implemented in both configurations of the pump laser.
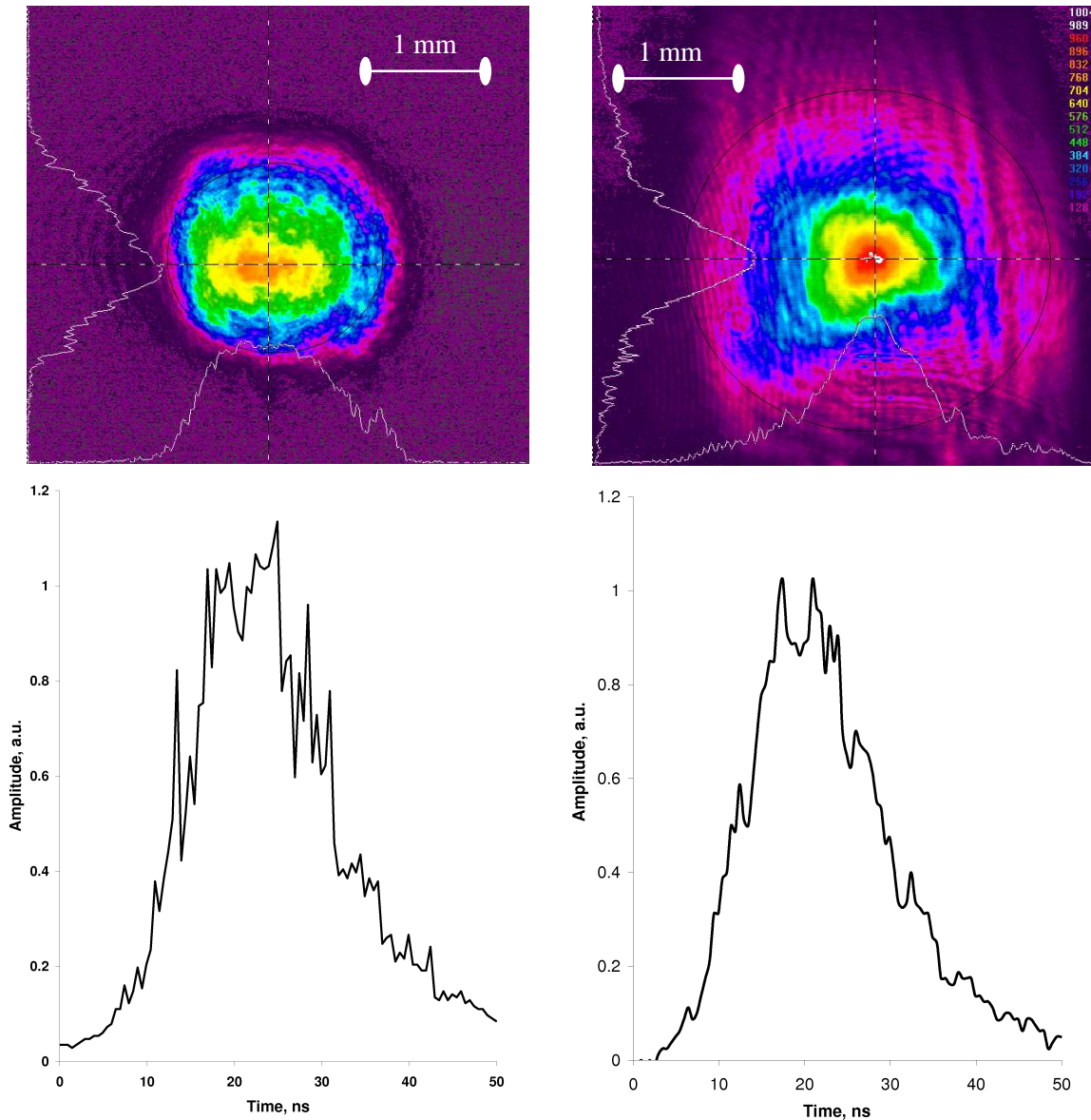
Fig.3.7 Pump energy distribution on the TISA-crystal (up) and temporal profile of the not seeded pump pulse (down) in Pump-1 (left) and Pump-2 (right). Wavelength 532 nm.

Further amplification of the laser emission in the 32-diodes pump-chambers of the post-amplifier is not able to amend the quality of the outgoing beam. Furthermore, in the configuration Pump-2 the spatial beam distortion after the pre-amplifier is increased in the post-amplifier (see Fig. 3.9). The post-amplifier provides a higher amplification ratio than in the configuration Pump-1 (see Fig. 3.8), while the implemented crystal rods for the same size have a smaller doping level. This leads to large spatial non-uniformity in the gain depletion, worse compensation of thermally-induced aberrations, and, hence, grow of wavefront distortions in the amplified laser beam. The temporal profiles of the pump pulses in both configurations do not show remarkable difference.

3.3 Pump laser specification
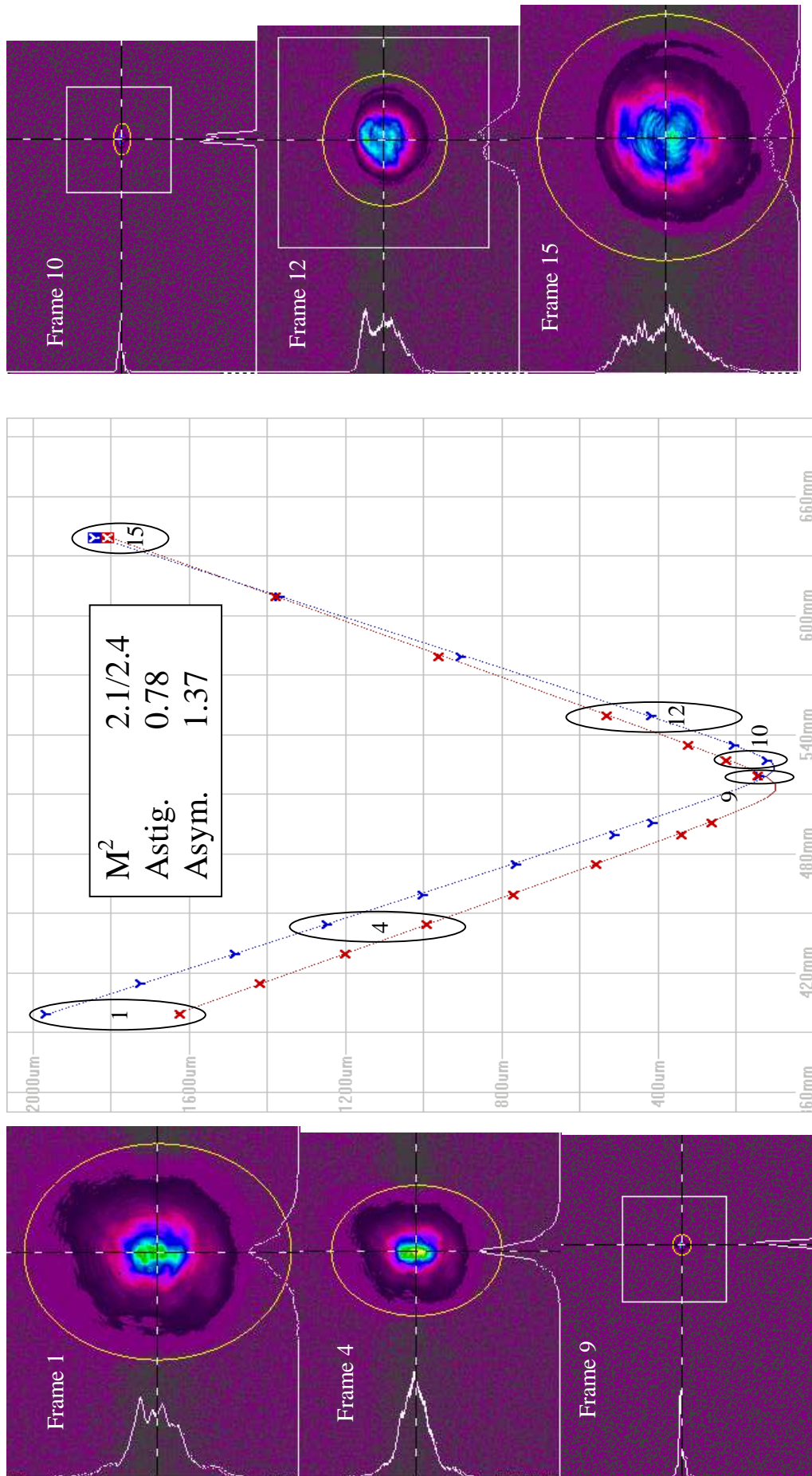
Fig.3.8 M^2-measurement of the pump-laser beam in the configuration Pump-1 for the horizontal (X) and vertical (Y) plane, wavelength 532 nm, output power 30 W. Some of the frames are depicted as well, numbered from left to right.
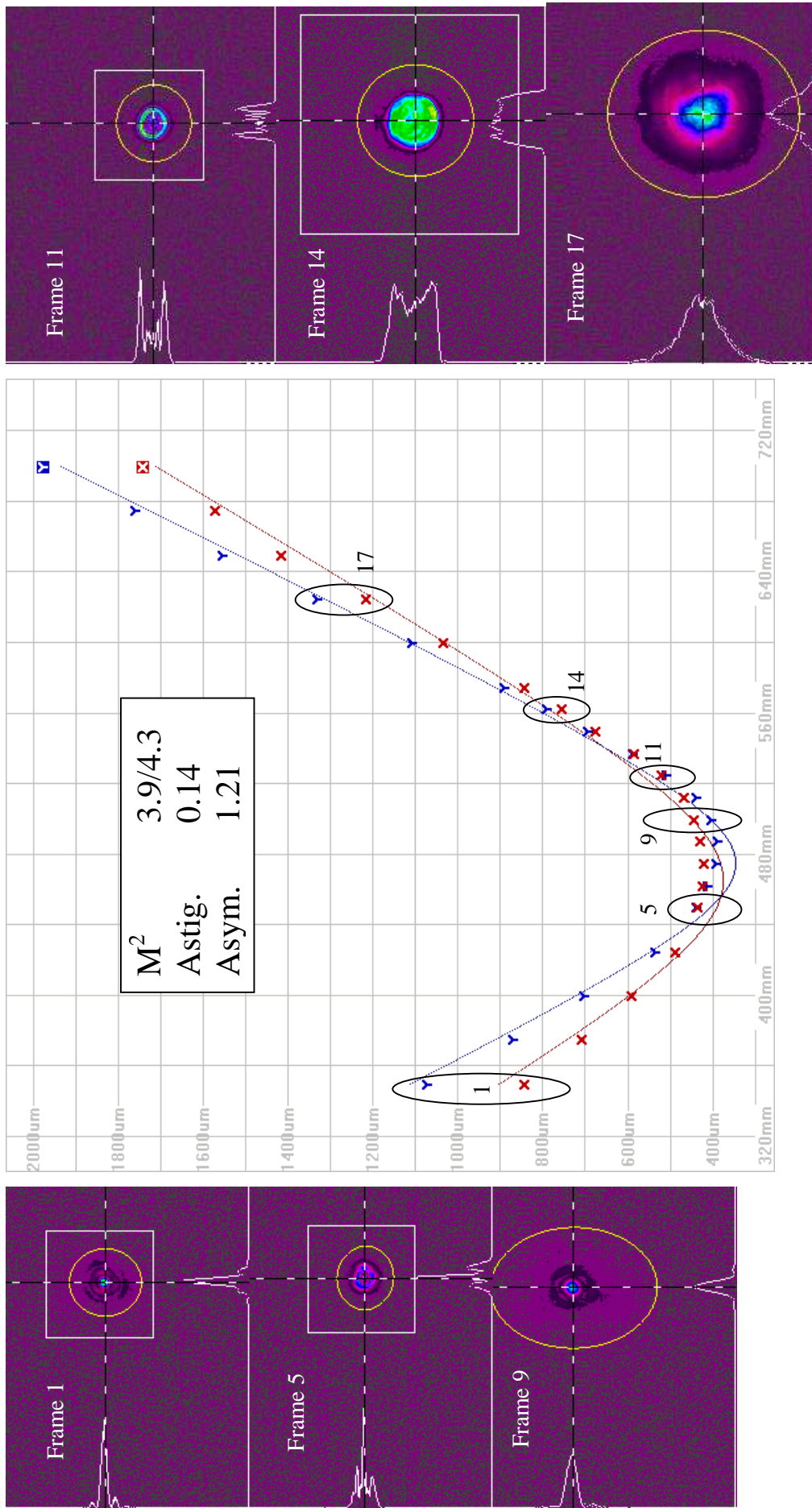
Fig.3.9 M²-measurement of the pump-laser beam in the configuration Pump-2 for the horizontal (X) and vertical (Y) plane, wavelength 532 nm, output power 47 W. Some of the frames are depicted as well, numbered from left to right.

To achieve a high yield of the TISA laser, a high pump power as well as a good spatial overlap between the pump beam and the resonator mode of TISA cavity is essential (see Subsection 5.2.3). With the Pump-1 a near-Gaussian energy distribution in the pump beam cross-section was obtained on the TISA-crystal (see Fig.3.7, left). With the Pump-2 the pump beam has worse overlap with the eigenmode of the TISA cavity and, therefore, yields a lower pump efficiency (see Fig.3.7, right). However, further improvement of the pump-beam energy distribution on the TISA crystal is possible (see Subsection 3.4).

3.3.2 Pointing stability

In both configurations the pump laser has a certain warm-up time. Unlike usual commercially available systems with time of 30 minutes, this one requires approx. three hours until drift of the laser beam becomes negligible. The source of the pointing instability is located in the MO: on the Fig.3.10 a trend of the beam position after the MO is depicted with a total walk-off of 80 μrad. No output power drift was observed for the MO.

Figure 3.11 shows a trend of the pump beam position in the plane of the TISA crystal. The vertical and horizontal planes are switched compare to Fig. 3.10 because of bending mirrors between the pump laser and the TISA. Obviously, the deviation of the outgoing pump beam mimics the behavior of the MO-output. The total displacement of the pump beam of ~0.5 mm in the TISA plane makes a long-term TISA operation impossible without sufficient preheating time. Even short switch-off of the laser affects the beam pointing: after a 20-minutes break the pump laser requires another hour to return to the steady-state position.

Although the output power of the pump laser at 1064 nm does not show any remarkable fluctuations, those are observed at 532 nm. It is caused by an alignment sensitivity of the LBO crystals of the SHG-converter. Considering a strong disparity of this sensitivity in two orthogonal directions, the crystals were mounted with their more sensitive axes horizontally where the beam drift is smaller. Nevertheless, the starting power of the laser at 532 nm is approx. 85% compare to the steady-state condition.

To avoid the warming-up time during intensive operation at a field campaign, the pump laser can be run continuously with the MO tuned to the full output power and the amplifiers delayed. The laser was operating in this mode during COPS measurement campaign (see Subsection 6.2). After the amplifiers are tuned for the full-power output the laser needs approx. 30 minutes to come in a steady-state operation mode.
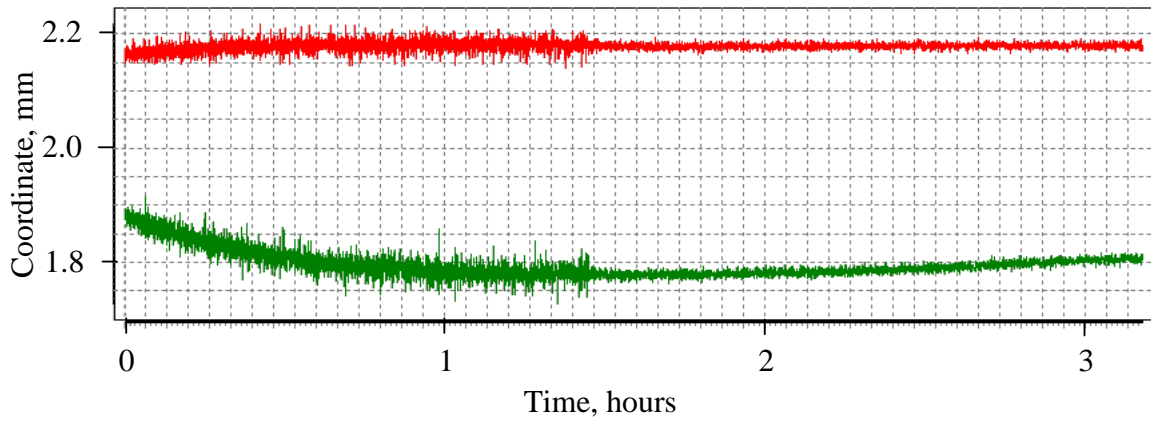
Fig.3.10 Spatial stability of the pump beam (after MO, IR); red – horizontal plane, green – vertical. Higher fluctuation first 1½ hour is caused by implementing of a single-shot acquisition, whereas later a 4-shot averaging was applied.
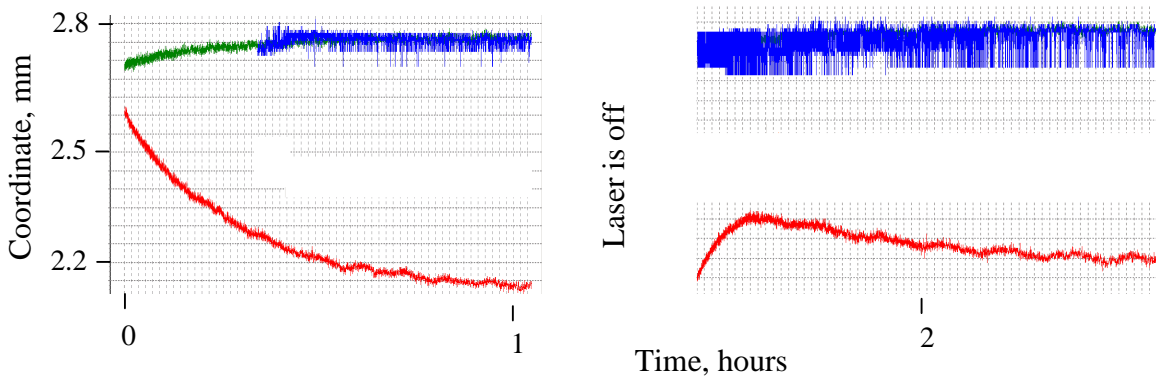
Fig.3.11 Spatial stability of the pump beam (on the TISA-crystal, 532 nm); red – horizontal plane, green(blue) - vertical plane. The overlapping blue trend is a momentary position of the beam peak in vertical direction.

3.4 Outlook

Being a state-of-the-art system, the pump laser required a lot of time for adjusting it to the required specifications. This included improvement of the driving electronics and software, modernization of the base frame of the laser head, optimization of the optical components. The components which caused the largest delay were the pump diodes in the amplifiers. The originally used "Monsoon-long" diode bars from Spectra-Physics had certain weaknesses in the construction: the water-flow channels had nondurable gold coating. It made the channels prone to galvanic corrosion, causing water leakage and operation break until next version of the pump chambers was developed. The overall delivery delay of the pump laser exceeded three years.

To improve the efficiency and stability of the laser operation, further optimization of the pump laser is necessary. In a first hand, the overlap between the pump beam and the eigenmode of the TISA-cavity has to be enlarged. The spatial distribution in the currently deployed pump beam corresponds the profile 1 (see Fig. 3.9). However, there are better cross-sections of the pump beam available (profiles 14-17). The current lens combination of negative and positive lenses in front of the TISA laser (a defocused Galileo-telescope) can not obtain imaging of the desired profiles without placing the beam waist on intermediate optics (see Fig. 5.28), causing its optical damage. To fulfill this imaging the beam shaper has to be modernized to the Kepler-scheme with two positive lenses. The latter was not implemented for experiments due to focusing of the high-power emission between the lenses of the beam shaper. Using of an evacuated cell with Brewster windows should allow for this modernization.

Furthermore, the long-term angular drift of the laser beam after the MO must be minimized. The major source for this drift is, likely, a temperature dependence of the elements of the MO: during the operation, the temperature in the lab raised several degrees up and came into a steady-state condition in several hours together with the pump beam position and the output power. Although the appearance of the temperature-induced spatial instability of the MO output is not fully revealed, some observations and the experience of the system maintenance marked the Q-switch and the pump chamber of the MO as probable sources of the disturbance.

The Q-switch build by a pair of RTP-crystals can be temperature stabilized the same way as it was done with the LBO crystals in the SHG. For this purpose the crystal mount has to be put on a Peltier-element, whose other side is fixed on a heat sink. An electronic circuit will provide the automatic control of the temperature using a semiconductor temperature sensor. This modification is currently under discussion.

The pump chamber of the MO has only 6 diodes, packed in a three-fold geometry (see Fig. 3.3), which makes illumination of the Nd:YAG rod not fully symmetrical. Likely, a long-term temperature drift in the constructive elements of the pump diodes causes drift of their wavelength and pump power. Hence, this causes deviation of the pump power absorbed in the Nd:YAG crystal and shifting of the thermal lens with the following drift of the output beam. There are different ways to solve this problem.

The current MO can be replaces with another one, build on two pump chambers with a 90° quartz rotator in between, as it was made in the construction of the amplifiers. Then thermal effects induced by the pump diodes will be self-compensated, improving both the spatial stability

of the laser beam and a depolarization compensation [Sträßer et al., 2007]. Furthermore, the two-rod layout allows to increase the MO output power.

This modernization requires additional funding and human sources. There is an easier solution available, when the propagation direction of the MO laser beam is actively stabilized. The first bending mirror can be finely tuned by piezo actuators to keep the outgoing beam on the same track. As a reference signal, the response of a quadrant detector can be used. Although this technique requires a test to define its boundaries, the solution is cheap and fast.

Another important task is installing the IS and all the equipment for injection-seeding technique, similar to one described in Subsection 4.1.3. No problem is expected as far as the similar system was build and specified at University of Potsdam [Ostermeyer et al., 2005]. The seeded Nd:YAG laser can be deployed to pump OPO-converters, extending the transmitter to another wavelength regions.

Chapter 4

Spectrum control of the

Ti:sapphire laser

Maintaining the spectral properties of the TISA laser on a short as well as a long-time scale is essential to perform high-quality DIAL measurements (see Table 2.1). The emission spectrum of the laser transmitter is defined by the gain spectrum of the active medium, the transmission spectrum of the intra-cavity optics and the resonator parameters, obtaining the mode structure. Generally, the resulting laser spectrum consists of a superposition of longitudinal and transversal modes. To obtain lasing on the single transversal, TEM_{00}-mode, no special spectral narrowing technique is required. With a properly designed resonator, the pump energy excites only the volume of the resonator eigenmode in the crystal. The appearing "gain-guiding" effect obtains an effective mode selection. However, to restrict the emission of the TISA to the only longitudinal mode, a set of spectral narrowing techniques has to be applied.

4.1 Spectral narrowing techniques

4.1.1 Coarse spectral narrowing by intra-cavity optics

The spectrum of spontaneous emission of the TISA is about 300 nm broad with the maximum at 800 nm. The reflectivity of a commercial HR laser mirror with a dielectric coating in this wavelength region is $R > 99\%$ within ± 50 nm from the maximum (for $0°$ incident angle) and ± 20 nm from the maximum (for $45°$ incident angle, p-polarization). Further purifying of the spectrum may be achieved using intra-cavity optics with narrow-band transmission, e.g. intra-cavity Fabry-Perot interferometers and prisms [Hodgson, 1997; Elsayed, 2003]. However, the efficiency of these techniques is not sufficient for operation in a high-power high-gain laser cavity, and a multimode lasing can not be prevented. Furthermore, these components are prone to optical damage and their transmission spectrums are temperature sensitive, which decreases

stability of the system for in-field operations. It is difficult to tune and to stabilize their spectrums regarding the wide tuning requirements of the DIAL system. For instance, tuning of a multi-prism configuration [Elsayed et al., 2003; Bruneau et al., 1994; Bruneau et al., 1996] will lead for a displacement of the outgoing beam.

The most appropriate intra-cavity element for a coarse definition of the emission spectrum of the TISA is a birefringent filter (BF). It is a set of retardation plates with the thickness ratio of two consecutive plates from 2 to 4. Optical axes of the plates in the set are aligned to be parallel. The plates are mounted in the resonator at a Brewster angle regarding the eigenmode propagation. Due to the birefringence, the ordinary and extraordinary polarization components of the laser beam experience different refractive indices when propagate through a plate, and thus have a different phase velocity. Therefore, the polarization state of the electro-magnetic emission, namely the ratio of energies in *p/s* components, will be modified after the passage of the plate. The degree of the energy redistribution is wavelength dependant. This causes losses on the Brewster surfaces of the intra-cavity elements for the whole spectrum of emission except a preferred wavelength. The wavelength of interest is defined by an angle between polarization direction of the incident beam and the optical axis of the retardation plate.

When on the entrance of the single retardation plate the field is linearly polarized and the vector $\vec{E}$ of the electric field is horizontal, the polarization on the exit is distributed between two orthogonal modes as

$$\begin{pmatrix} E_x \\ E_y \end{pmatrix} = M \begin{pmatrix} 0 \\ 1 \end{pmatrix} = \begin{pmatrix} M_{11} & M_{12} \\ M_{21} & M_{22} \end{pmatrix} \begin{pmatrix} 0 \\ 1 \end{pmatrix}, \tag{4.1}$$

M is the total Jones matrix of the set, accomplished with losses on the Brewster-surfaces of the plates for the *s*-polarization. In a right-handed coordinate system with the *z*-axis coaligned with the propagation direction of the EM-wave, *x*-axis directed vertical and *y*-axis directed horizontal, the Jones matrix of a birefringent plate with the retardation axis parallel to the entrance surface is defined as [Bloom, 1974; Preuss and Gole, 1980]

$$M(\varphi, \theta, \lambda) = \frac{1}{n_o^2 - \cos^2 \varphi \cos^2 \theta} \times$$

$$\times \begin{pmatrix} q^2(e^{i\delta_e} \cos^2 \varphi(n_o^2 - \cos^2 \theta) + e^{i\delta_o} \sin^2 \varphi\, n_o^2) & q \sin \varphi \cos \varphi (e^{i\delta_e} - e^{i\delta_o})\sqrt{n_o^2 - \cos^2 \theta} \\ q \sin \varphi \cos \varphi (e^{i\delta_e} - e^{i\delta_o})\sqrt{n_o^2 - \cos^2 \theta} & e^{i\delta_e} \sin^2 \varphi\, n_o^2 + e^{i\delta_o} \cos^2 \varphi(n_o^2 - \cos^2 \theta) \end{pmatrix}, \tag{4.2}$$

$$with \quad \delta_e(\varphi,\theta,\lambda) = \frac{2\pi d}{\lambda} n_e(\lambda) \frac{\left[1 + \frac{\cos^2\theta\cos^2\varphi}{n_e^{\,2}(\lambda)} - \frac{\cos^2\theta\cos^2\varphi}{n_o^{\,2}(\lambda)}\right]}{\sqrt{1 - \frac{\cos^2\theta\sin^2\varphi}{n_e^{\,2}(\lambda)} - \frac{\cos^2\theta\cos^2\varphi}{n_o^{\,2}(\lambda)}}},$$

$$\delta_o(\varphi,\theta,\lambda) = \frac{2\pi d}{\lambda} n_o(\lambda) \frac{1}{\sqrt{1 - \frac{\cos^2\theta}{n_o^{\,2}(\lambda)}}}, \quad q(\lambda) = \frac{2n_o}{1 + n_o^{\,2}(\lambda)},$$

$n_o(\lambda)$, $n_e(\lambda)$ ordinary and extraordinary (along the optical axis of the plate) refraction indices of the quartz, respectively, d thickness of the plate, φ angle between optical axis of the plate and incident plane, θ tilting angle between entrance surface plane and $z0$ (by the optimum alignment $\theta = 90°$-θ_B, θ_B – Brewster angle).

For the set of plates 1…k with coaligned optical axes the general matrix is $M_\Sigma = \prod_{i=k}^{1} M_i$. Defining the transmission of the BF as a fraction of energy left in the initial polarization on the exit of the last plate of the set, for the horizontal polarization it amounts for $T(\lambda,\varphi) = \left|M_{22}^\Sigma\right|^2$ (see Eq. 4.1). The energy transferred in orthogonal polarization is coupled out of the cavity on Brewster-tilt surfaces of the intra-cavity optics. The transmission of the single surface is $T_\perp^B = q^2 = \left(\frac{2n}{1+n^2}\right)^2$, and for a ring cavity with Brewster-cut TISA rod and the 4-plate BF the losses for the s-polarized EM-wave will exceed 81% for a round-trip.

Figure 4.1 depicts calculated transmission spectrum of the BF for different mounting order of the retardation plates in the set, plates thicknesses of 0.5 mm, 1 mm, 2 mm and 8 mm. The plate consequence 8 mm, 0.5 mm, 1 mm and 2 mm was preferred for the TISA laser, emitting at 820 nm.

The given BF obtains a bandwidth of the main peak of the transmission spectrum of ≈ 5 nm FWHM or ≈ 1.3 THz. Taking into account that in a 1-m ring resonator the free spectral range between the longitudinal modes is $FSR = 0.3$ GHz, further spectral narrowing of the TISA laser is required.
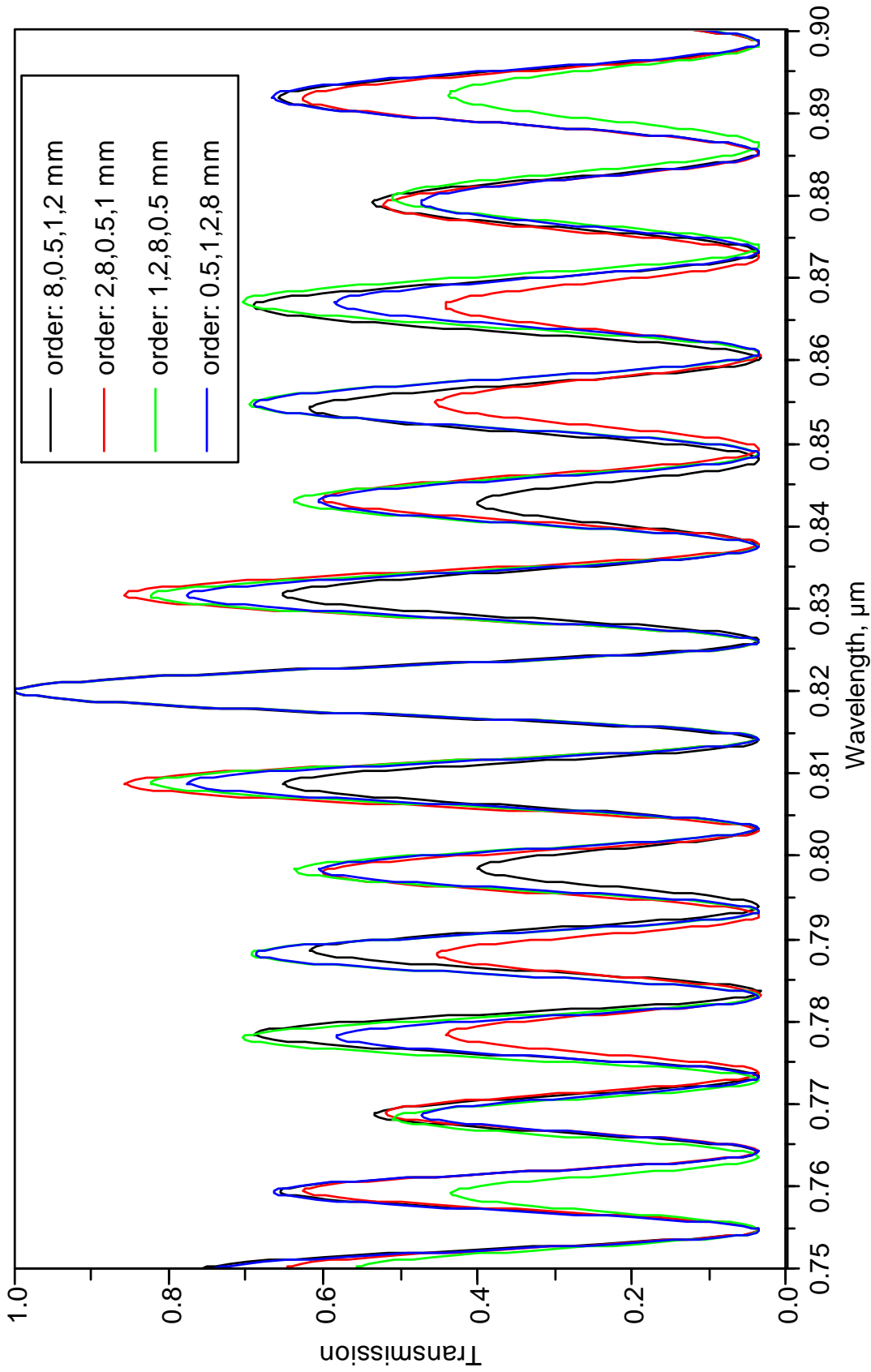
Fig.4.1 Calculated transmission spectrum of the BF for different mounting order of the retardation plates in the set, plates thicknesses of 0.5 mm, 1 mm, 2 mm and 8 mm. For every set transmission spectrum is the same for both directions of light propagation. The optimum plates order, when the peaks closest to the maximum are suppressed the best, is 8-0.5-1-2 (black trace)..

4.1.2 Fine spectral narrowing

Recently a new spectral narrowing technique was found to be very suitable for water-vapor DIAL transmitters, when a single-frequency operation together with a broad tuning range are required [Wulfmeyer and Bösenberg, 1994; Barnes and Barnes, 1993]. In this approach the beam of a weak cw laser, the so-called injection-seeder (IS) or master laser, is coupled in the cavity of a high-power pulse laser transmitter, also called slave laser.

When a Q-switch of the pulse laser opens or, as in the laser-pumped TISA laser, a pump pulse is absorbed in the active medium, the intra-cavity EM-field starts building up from initial number of photons. Due to a strong mode competition, the seeder frequency is preferred. If the cavity length is not controlled, the laser operates on a set of longitudinal modes in the vicinity of the IS wavelength [Barnes et al., 1993; Bruneau et al., 1994; Wulfmeyer et al., 1995; Wulfmeyer and Bösenberg, 1996]. The number of the modes depends on the ratio of the intensity of the injected field to the intensity of a natural seed, a fraction of fluorescence photons able to contribute laser emission (for further details see App. A.). When the ratio exceeds certain threshold, the laser spectrum is limited to two modes, closest to the IS wavelength. Below the threshold numerous modes will participate the pulse evolution.

A single-frequency operation is achieved when the seeder frequency coincides with one of the longitudinal modes of the slave cavity. In this case, the laser will operate just on one longitudinal mode. Among the existing techniques to maintain the cavity length of the slave laser in resonance with IS, passive and active ones can be distinguished.

With the passive control, drifts in the optical path of the slave laser resonator are used to detect a resonance and to fire the laser [Wulfmeyer, 1998]. An error signal from the slave cavity is sent to the control electronic. Using a feedback loop, a resonance length of the cavity regarding the seeder frequency can be maintained with a control element. Several approaches have been developed for the production of the error signal.

The laser pulse itself has been used to define a resonance position. In [Park et al., 1984] the laser frequency has been stabilized by monitoring simultaneously the transmission of the laser pulse and the IS through an external interferometer. An often-applied technique is the minimization of the pulse build-up time [Rahn, 1985]. A similar technique has been presented in [Grund et al., 2001]. The frequency offset between the laser transmitter and the IS is measured shot-by-shot using a beat-note signal. This offset is fed via a feedback loop to a piezo mirror to stabilize the optical path length in the slave resonator. Although these techniques are easy to incorporate, they

have several disadvantages. Their response time is limited by the repetition rate of the laser, making them too slow to remove acoustic vibrations in the cavity. Furthermore, their error signals are not sensitive to small frequency drifts and the adjustment of the cavity length can be performed only after emission of the laser pulse. The latter is especially critical for the DIAL technique with a pulse-to-pulse frequency alternation. Here the difference signal has to be produced and the cavity length has to be adjusted in the resonance with the IS before the transmitter fires out the pulse.

With respect to this requirement some more techniques have been examined. The speed and the accuracy of the frequency stabilization can be considerably improved, if the resonance of the seeder itself in the slave cavity is used as the control signal. Several approaches in this direction have been developed. The ramp-and-fire technique is based on the production of an artificial resonance with a fast piezo mirror [Henderson et al., 1986]. Though this technique seems to be reliable, the problem is the fast movement of the piezo mirror. As it continues moving during the pulse build-up time, an unwanted frequency chirp in the laser pulse occurs.

Similar problems are present in the side-of-fringe technique [Vassen et al., 1990; Wulfmeyer, 1998]. The cavity length is stabilized to the wing of the resonance, so that a frequency chirp also occurs during the Q-switch operation. The narrow resonance signal can easily be lost and additional normalization of the error signal with the seed power is required using another detector.

Among the techniques those should be preferred, which are minimizing the movement of cavity elements, thus avoiding limitations in the laser frequency stability and in the lifetime of the resonator elements. There are two techniques fulfilling all aforementioned requirements. The first one is based on a polarization sensitivity of the seeder resonance in the slave cavity [Hänsch and Couillaud, 1981]. The disadvantage of this method is lack of tunability: even for a minor wavelength tune, the layout of the controlling detectors has to be realigned.

4.1.3 Pound-Drewer-Hall stabilization technique

The other technique is based on the optimized Pound-Drever-Hall (PDH) technique [Drever et al., 1983; Wulfmeyer et al., 2000a; Ostermeyer et al., 2005]. The phase shift of the reflected slave cavity field is used to produce an error signal for the resonator length control. This approach has been applied for the first time in a coherent Doppler lidar transmitter in the master-slave configuration [Wulfmeyer et al., 2000a]. In that work a frequency stability of 0.2 MHz 1σ was achieved.
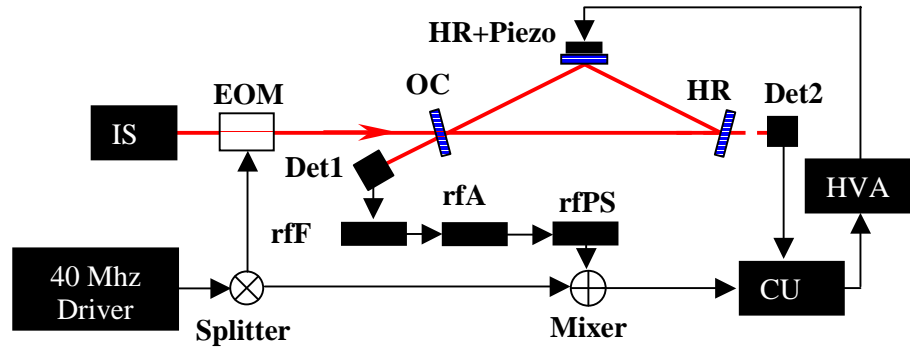
Fig.4.2 PDH stabilization scheme adopted for a ring cavity. Here EOM – electro-optical phase modulator, HR – high-reflecting mirror, OC – output coupler, Det1, Det2 – biased photodetectors, rfF – rf-filter, rfA – rf-amplifier, rfPS – rf-phase shifter, CU – control unit, HVA – high-voltage amplifier.

Figure 4.2 depicts the set-up of a feed-back loop used for the stabilization of the TISA laser in the experiment at 820 nm (see Subsection 5.5). An rf-generator produces a high-frequency signal for an electro-optical phase modulator (EOM, Quantum Technology REM-101-P). A high modulation frequency has to be preferred to obtain a high SNR in the slave cavity with a low finesse, but not exceeding a half of the free spectral range (FSR) of this cavity [Black, 2001]. Furthermore, a high frequency modulation broads the spectral bandwidth of the high-power laser as well. Therefore, a 40 MHz modulator was chosen for the experiment.

After propagation of the IS emission through the EOM, two sidebands appears in its spectrum at the frequencies 40 MHz from the carrier (see Fig.4.3). The modulation depth for the successful operation is defined experimentally. Theoretically, the optimum ratio of power in a sideband to the power in the peak is 42% [Black, 2001].

The PDH-technique deploys a length noise of the slave cavity with the circulated IS-emission to produce a correction signal. The cavity acts as a Fabry-Perot interferometer (FPI), yielding the transmitted and reflected EM-fields. The reflected field is detected with Det1 (Thorlabs DET210) and filtered with an rf-filter (rfF, Municom 5BP8-40/10-S) to select the information on the sideband frequency. The filter output is amplified (rfA, Miteq AU-4A-0110) and mixed with a fraction of the rf-generator signal in a phase detector (Municom ZRPD-1-BNC). To eliminate a phase shift of the two signals, a manual phase shifter (Municom MP-180-40-4-S) is deployed. The produced error signal is delivered to a control unit (CU), a specially designed circuit board (manufactured in NCAR, Boulder). Another input for the CU is the signal from the photodetector Det2, observing the transmitted field to bound the stabilization region to the vicinity of the cavity resonance. The correction signal from CU is amplified with a high-voltage
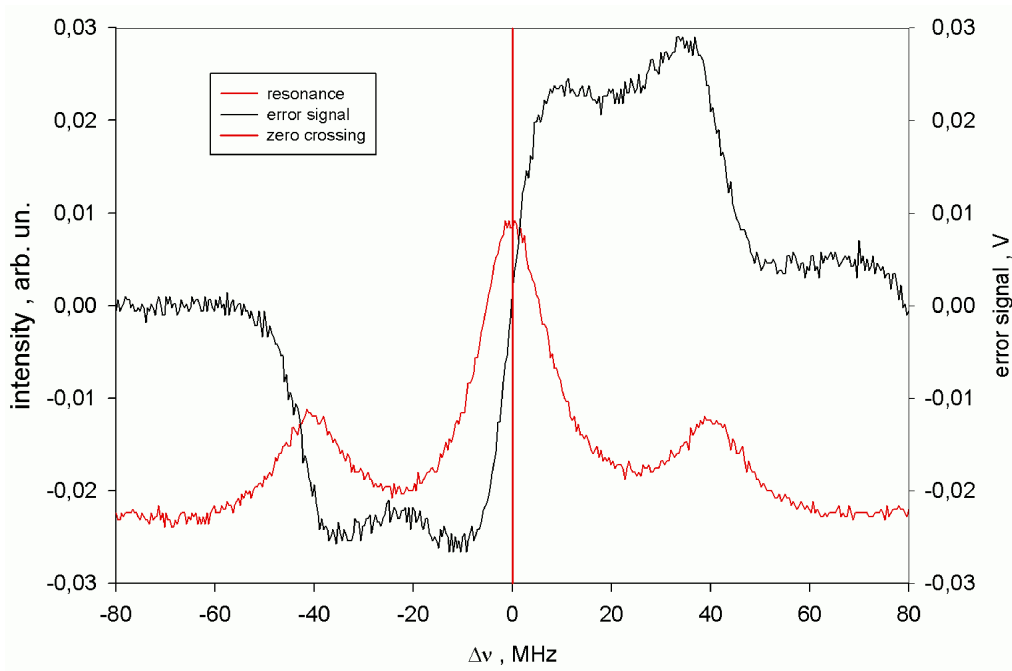
Fig.4.3 Signals in a PDH stabilization circuit: relative IS frequency with sidebands (red curve) and error signal (black curve). Resonance position is marked with a red line (regarding [Wulfmeyer et al., 2000a]).

amplifier (HVA, PI E-507) and used to drive a piezo actuator with a light-weight resonator mirror fixed on it, adjusting the cavity length. To minimize the response time, the fastest high-voltage piezo actuator (HVPA) available was preferred (PI P-010.00H) together with a ½"×1 mm HR-mirror from fused silica. The response frequency of the actuator with the glued mirror can be estimated as

$$f \approx \frac{1}{3} f_{res} = \frac{1}{6\pi} \sqrt{\frac{S}{\frac{1}{3} m_{PA} + m_{mirror}}} \approx 6.7 \text{ kHz} \qquad (4.3)$$

with f_{res} resonance frequency, $S = 2.7 \cdot 10^7$ N/m stiffness of the HVPA, $m_{PA} = 4.1 \cdot 10^{-3}$ kg and $m_{mirror} = 3 \cdot 10^{-4}$ kg mass of the HPVA and the mirror, respectively. On the other hand, the response frequency is limited by the amplifier and can be calculated as

$$f = \frac{i}{2CU_{pp}} = \frac{12 \cdot 10^{-3}}{2 \cdot 21 \cdot 10^{-9} \cdot 100} \approx 2.9 \text{ kHz} \qquad (4.4)$$

with i maximum average current of the amplifier, C capacity of the HPVA and U_{pp} peak to peak voltage of the output signal.

Summarizing, the following advantages of this technique are to be mentioned. First, the error signal is nearly continuously present, so that the feedback loop can be operated with a high bandwidth. This leads to an optimal reduction of frequency deviations. The error signal crosses zero exactly at the resonance, yielding minimization of the frequency chirp and optimization of the seeding efficiency. The slope of the error signal is large, leading to a high sensitivity of the error signal to frequency fluctuations. At last, the error signal is produced using an RF-technique, making the feed-back loop insensitive to sources of the electrical noise.

For the DIAL operation the stabilization technique has to allow for a pulse-to-pulse alternation between online and offline wavelengths. The feed-back loop has to readjust the cavity length for every pulse. The response frequency of ≈ 3 kHz is sufficient for cavity tuning at a repetition rate of the transmitter up to 1 kHz.

Nevertheless, this operation provides a high load on the actuator and significantly decreases its lifetime. It was shown [Wulfmeyer and Walter, 2001a,b] that the spectral purity of the offline signal is not critical for accurate water-vapor measurements with DIAL. Hence, stabilization of the cavity length while lasing offline can be omitted. For this operation mode, the PDH stabilization circuit has to be accomplished with an input gate. Triggered to the IS, this device send either error signal of the cavity when the transmitter is seeded with an online source, or zero, when the laser works 'offline'.

4.2 Injection seeder – experimental set-up

As a seeding source, a stabilized single-mode external cavity diode laser (ECDL) can be applied. An ECDL is smoothly tunable within few nanometers, which is sufficient to operate on a pre-selected band of absorption lines. In the following sections two IS used in the experiments are described. For the experiment in a wavelength region near 935 nm and for first measurements with the transmitter at 820 nm, an IS bases on a Toptica DL100 system was implemented. Providing a single-wavelength emission either at an online or an offline wavelength, the IS was applied for initial specification of the TISA laser. In both experiments the ECDL was tuned for a single-frequency operation, laser driver was optimized to achieve a widest possible mode-hop free tuning range. Description and specification are detailed in the Subsection 4.2.1.

For the TISA operation as a part of a water-vapor DIAL mobile platform (see Subsection 6.2), a custom made double-ECDL system was manufactured at DLR Oberpfaffenhofen. During its
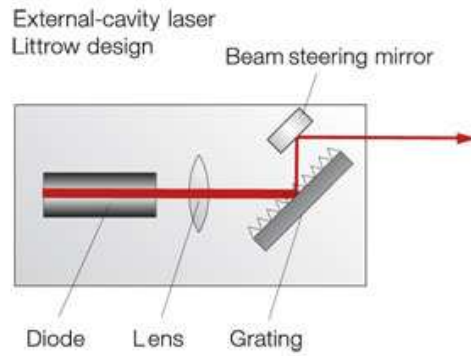
Fig.4.4 Principle design of an ECDL in the Littrow configuration (after www.toptica.com)

maintenance at IPM the IS was repaired including replacement of a fast fiber switch with following realignment of the lasers. Furthermore, some minor changes in a LabView driving program were introduced to optimize the operation. For details see Subsection 4.2.2.

4.2.1 Injection seeder based on a Toptica system

The Toptica DL100 system comprises an external-cavity diode laser and a driver. The ECDL is build in a Littrow design (see Fig. 4.4): emission of the laser diode in a standard 5.6 mm package passes through its AR-coated output surface, is collimated with a lens and directed to a grating. The grid reflects the energy of the -1st order of diffraction back to the laser chip, forming an external linear resonator with a high-reflective rear surface of the diode. Tilting the grating, the ECDL can be tuned to the desired wavelength within a gain profile of the laser diode. For a rough angle definition, an adjustment screw is used. The fine wavelength tune (within a mode-hop free range) is realized with a high-voltage piezo actuator.

The laser emission is coupled out with the zero-order diffraction of the grating. To preserve the propagation direction of the outgoing laser beam while tuning, an additional bending mirror fixed on the grating mount was applied. The temperature of the laser diode is measured with a thermal sensor and adjusted with a peltier element. To improve the mechanical stability, the ECDL was mounted on a 1 cm thick plate and sealed with a metal cover. The laser emission escapes the sealed volume through an output window, a glass plate tilted at a Brewster angle. The driver of the system comprises a temperature control unit DTC110, a current control unit DCC110, a scan control unit DSC110 for a fine HVPA steering and a diode control unit DC110.

Output of the ECDL is coupled with a fiber coupler (FCp, Schäfter+Kirchhof 60SMS-1-4-A15-02) in a single-mode polarization-maintaining fiber (Schäfter+Kirchhof PMC-850-5,4-NA012-3-APC-150-P) with angle-polished connectors (APC) (see Fig.4.5). This fiber showed a good
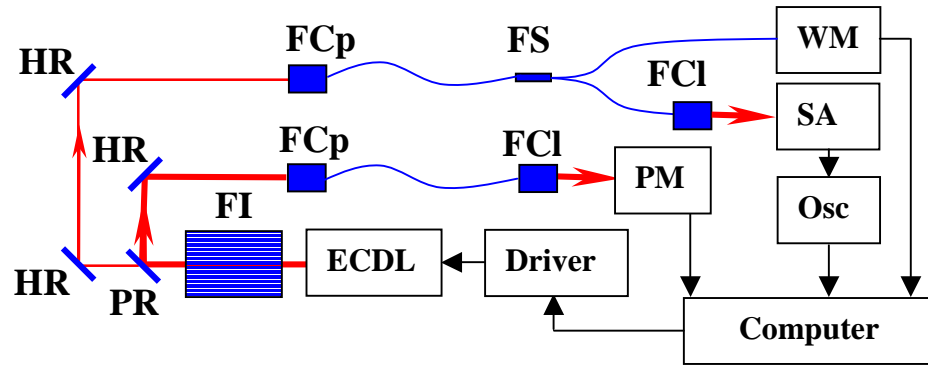
Fig.4.5 Set-up of the IS. Here ECDL – external-cavity diode laser, FI – Faraday isolator, PR – partially reflecting mirror, HR – high-reflecting mirror, FCp – fiber coupler, FS – fiber splitter, FCl – fiber collimator, PM – power meter, WM – wavemeter, SA – spectrum analyzer, Osc – oscilloscope.

performance at 935 nm as well as at 820 nm. On the exit of the fiber the beam is focused on a power meter (PM, Coherent LM2) using a fiber collimator (FCl, Schäfter+Kirchhof 60FC-4-A11-02). Although the fiber has an APC with an end-surface cut at 8° and the optics of the fiber coupler and fiber collimator has an AR-coating, a small fraction of the incident energy reflects back into the ECDL, increasing wavelength instability of the laser emission. To avoid this effect, a single-stage faraday isolator (FI, Linos FI-930-5SC and Linos FI-800-5SC for the experiment at 935 nm and 820 nm respectively) was mounted between the ECDL and the fiber coupler. Two bending HR-mirrors were installed between the ECDL and the FCp to obtain fine steering of the coupled beam for a better coupling efficiency.

The energy leak through the first bending mirror is coupled in the other fiber. This channel is used for the control and specification of the system, namely definition of the wavelength with a wavemeter (Burleigh WA-1500) and spectral properties with a spectrum analyzer (SA, Coherent Model 240) and an oscilloscope (LeCroy LC564DL). For a higher experiment flexibility the energy was multi-channeled using a fiber splitter (FS, Newport F-CPL-S12855), allowing for simultaneous measurements.

To stabilize the wavelength of the ECDL emission a feed-back loop was build. As a reference signal, the output of the wavemeter was used. A LabView program acquires the wavemeter via the COM-port of a computer. The correction signal is produced from comparison of the response with a predefined value. Via an ADC/DAC board (Meilhaus AB-BNC16) the discrepancy signal is converted into the analog form and transmitted further to the external voltage control of the piezo actuator in the ECDL. This feed-back loop was build in IPM by Armin Austerschulter,
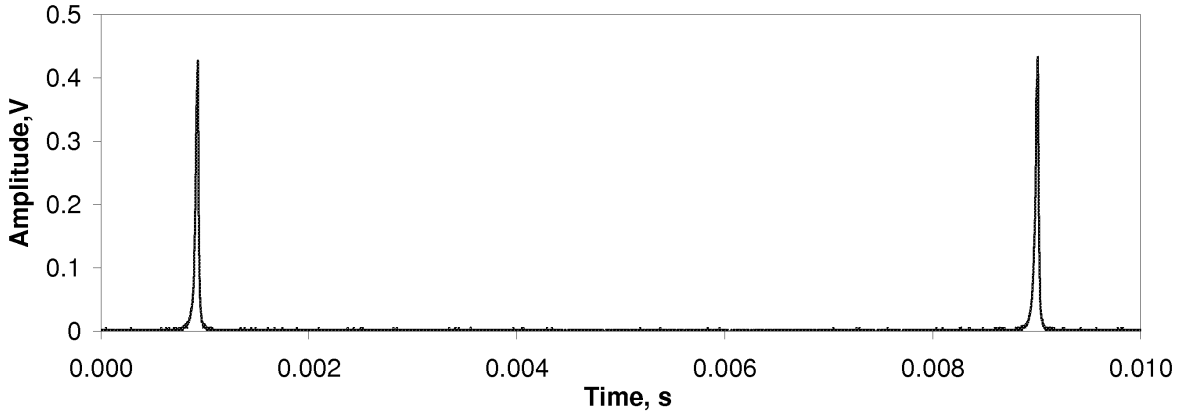
Fig.4.6 Spectrum of the IS at 935 nm, recorded with the spectrum analyzer. Having FSR = 7.5 GHz and finesse > 250, the SA defines the single-mode operation of the IS with an ucertainty < 30 MHz, limited by the resolution of the instrument.

LabView program was later improved by Christiane Wohlfahrt [Wohlfahrt, 2006].

This IS was implemented in both experiments, at 935 nm and 820 nm. To modify the layout to the other wavelength, the laser diode chip and the FR were replaced. The laser diode Toptica LD935-50-AR2 with a power of 50 mW (free running) and a tuning range of 910-970 nm was applied for the experiment at 935 nm. The output power on the exit of the ECDL and behind the fiber collimator did not exceed 33 mW and 20 mW, respectively. This corresponds the coupling efficiency of 60%, which is less than the maximum achievable value of 80% (see Schäfter+Kirchhoff, www.sukhamburg.de). The higher losses can be explained by lower coupling efficiency of the laser beam for a non-circular shape of the cross-section.

For the seeding at 820 nm the mirror set was replaced as well as the laser chip with a diode from Sanyo (DL7032-001) with the specified output power of 100 mW (free-running) and tuning range of 810-830 nm. Due to a small gain at 820 nm, the IS and the TISA laser operated at 825 nm. The maximum output power of the ECDL coupled out of the fiber was ≈ 16 mW at 825 nm. This ECDL was deployed for the initial specification of the TISA transmitter.

For the verification of the single-frequency operation and measurement of the spectral bandwidth of the seeding emission, the spectrum analyzer was used. It comprises a focusing lens with a focal length of 10 cm, a confocal Fabry-Perot interferometer with a mirror spacing of 10 mm, and a high-speed detector. The FSR of the FPI is 7.5 GHz. The signal from the detector is sent to an amplifier (HMS-Elektronik, Model 564) and displayed on the oscilloscope. Figure 4.6 depicts the spectrum of the IS at 935 nm. The measured finesse is ≈ 250, yielding the instrumental

uncertainty of ≈ 30 MHz. In the absence of a secondary spectrum the single-frequency operation of the IS was confirmed.

To verify a long-term stability of the IS, the 20-hour test was performed (see Fig.4.7). The ECDL was stabilized at 935.6846 nm, the strongest water-vapor absorption line in the region (see Table 5.1). The upper plot presents a wavelength trend of the IS, recorded with a 100 s time-step and 32 MHz resolution. The standard deviation of the data is < 20 MHz, limited solely by the resolution of the wavemeter. The wavelength offset in the beginning corresponds the stabilization time of the feed-back loop. The second plot shows the trend of the voltage on the piezo actuator, only a slow long-term drift of the ECDL was detected. The third plot presents temperature fluctuations in the laboratory (copied from a paper-record of temperature/humidity sensor). A trend of the power coupled out from the fiber is depicted on the last plot. The IS showed a good long-term stability in the stable environment. The specifications of the IS on the base of the Toptica DL 100 system are summarized in Table 4.1.

Table 4.1 Specification of the Toptica DL 100 system used in 820/935 nm experiments

Parameter	935 nm	825 nm	Notes
Tunability, nm	925…945	823… 850	
Mode-hop free range, GHz	< 10	< 10	
Linewidth, MHz	< 30	< 30	resolution limited
Frequency stability, MHz 1σ	< 20	< 20	resolution limited
Coupling eff.	> 60%	> 60%	
Output power, mW	20	16 (at 825 nm)	coupled out the fiber
Beam profile	1 mm	1 mm	
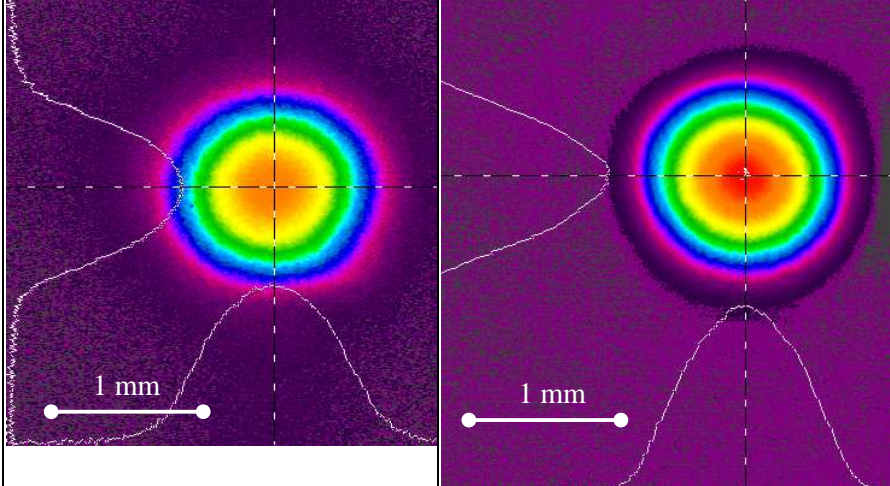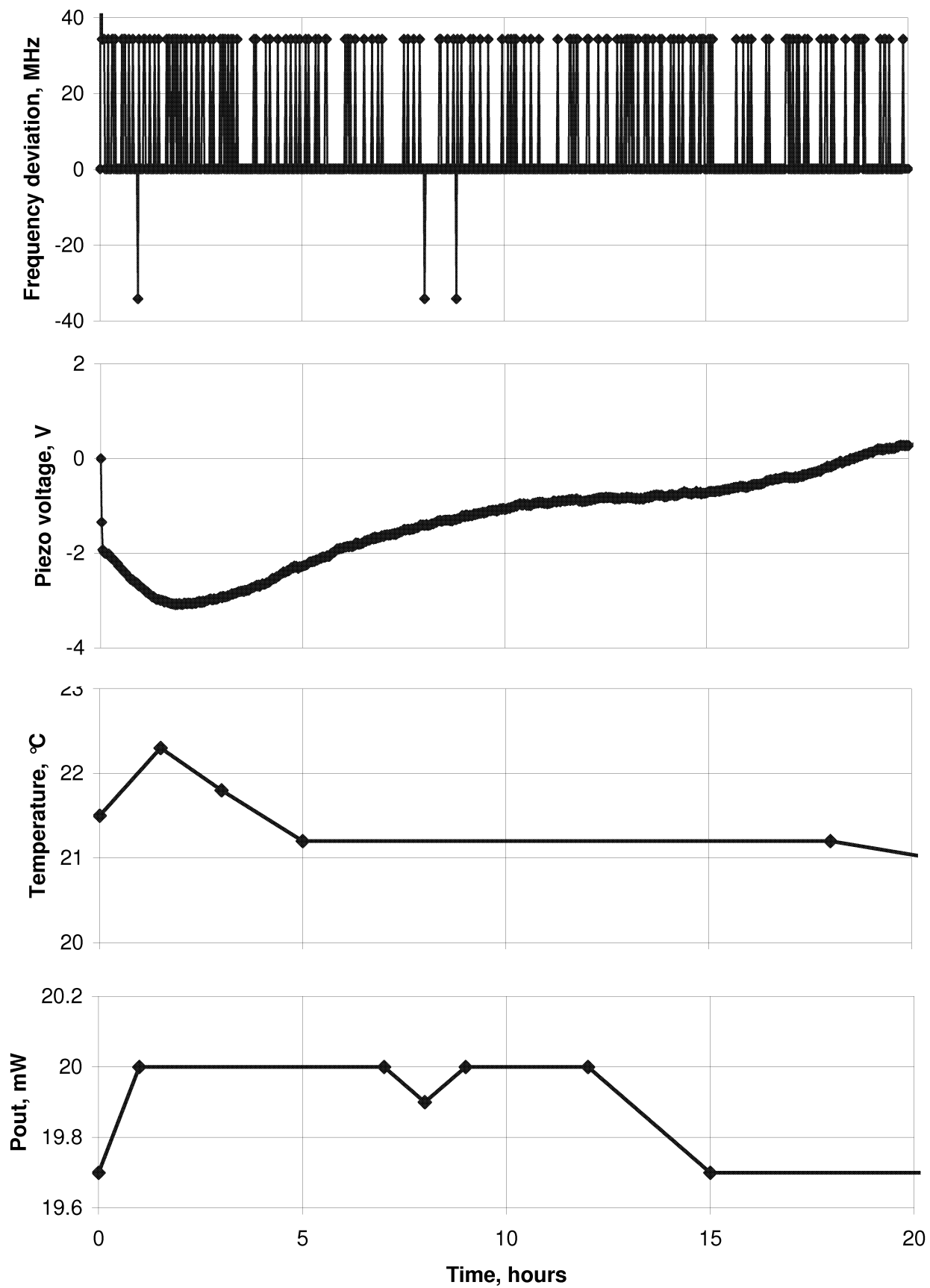
Fig.4.7 Long-term test of the IS on the base of the Toptica DL100 system at 935 nm. From top: IS frequency deviation, value of correction signal, temperature, output power.
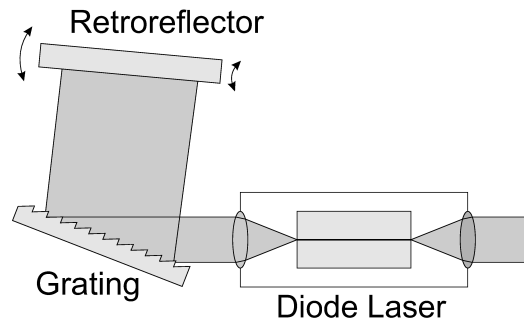
Fig.4.8 Principle design of an ECDL in Littman/Metcalf configuration (after www.sacher-laser.com).

4.2.2 Injection seeder developed at DLR Oberpfaffenhofen

In the final stage of the experiment, when the TISA transmitter was incorporated in the ground-base water-vapor DIAL (see Chapter 6), a dual-wavelength IS developed at Institute for Atmospheric Physics (IPA) of the German Aerospace Center (DLR) in Oberpfaffenhofen was implemented. The system is based on two stabilized ECDL's (Sacher Laser, TEC 500 Leon), one tuned at an online wavelength and other at an offline one. The lasers are build in a Littman/Metcalf configuration (see Fig.4.8).

The cavity of the laser is formed with a HR retro-reflector and the front facet of a laser diode as the OC. The emission of the tapered laser diode is collimated with a lens and directed to a grating. The -1st order of diffraction propagates further to the rear resonator mirror and then is reflected the same way back to the chip. By double propagation of the diffraction grating during a round-trip, side modes are better suppressed. The tunability is better and, hence, the mode-hop free range is broader then in the Littrow configuration. Using of a tapered laser diode chip allows for a higher output power referring to the Littman/Metcalf technique [Stry et al., 2006].

Tilting the grating, the laser wavelength can be smoothly tuned. A coarse adjustment over the whole tuning range of the ECDL is performed with a motor drive, for the fine steering of the grating a piezo actuator is applied. The motor and the piezo actuator are controlled either directly from a driver of the ECDL, or from any computer, connected to the driver via the universal serial bus (USB).

Figure 4.9 presents the scheme of the double-ECDL IS. The laser emission of both ECDLs is combined in a fast electro-optical switch (OMP2), allowing for the pulse-to-pulse alternation of the channels at repetition rates up to 1 kHz. The switch is triggered by the pump laser.
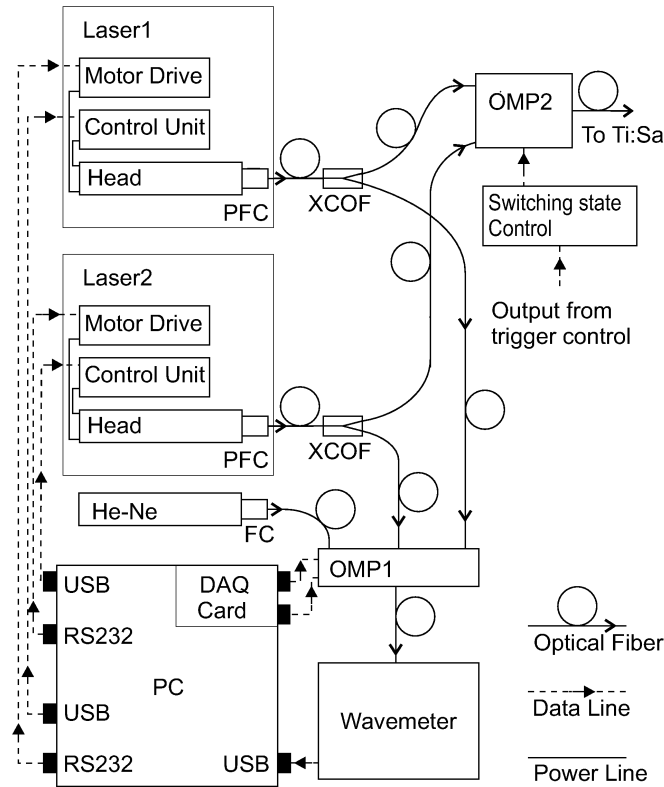
Fig.4.9 Principle scheme of the IS developed at DLR. Here FC – Fiber coupler, PFC – Precision Fiber Coupler, XCOF – Cross Coupled Optical Fiber, OMP – Optical Multiplexer, HeNe – helium-neon laser. Courtesy of DLR Oberpfaffenhofen.

Several percent of the emission of every ECDL is chopped off in a cross-coupled optical fiber (XCOF) and directed to a precise wavemeter (HighFinesse, Angstrom WS/7) via second multiplexer (OMP1). A stabilized HeNe laser (SIOS, Model SL 03, $\lambda = 632.9900894$ nm) is coupled into the wavemeter via the same OMP1. Switching the input channels, the wavelengths of both ECDLs and the HeNe laser are measured in a cycle. These measurements provide the information for a feed-back loop, organized on the base of a computer with a LabView program. The duration of the cycle is adjustable, 30 s was found to be optimal. Once in a round the wavemeter connects via the OMP1 to the stabilized HeNe for a recalibration. This is required because of continues temperature drift of the wavemeter and helps to keep the absolute measurement uncertainty < 5 MHz 1σ. The acquired frequency measurements are stored in a file and can be used later in a water-vapor retrieval for a fine data correction.

Although the system was completely specified in DLR in the optical lab, another specification for the work in the mobile ground-based platform for the DIAL was required. Figure 4.10 (a) depicts a 17-hour trend of a frequency deviation of IS, measured during an intensive operation period (IOP) of COPS measuring campaign [Wulfmeyer et al., 2008] on 1-2 August 2008.
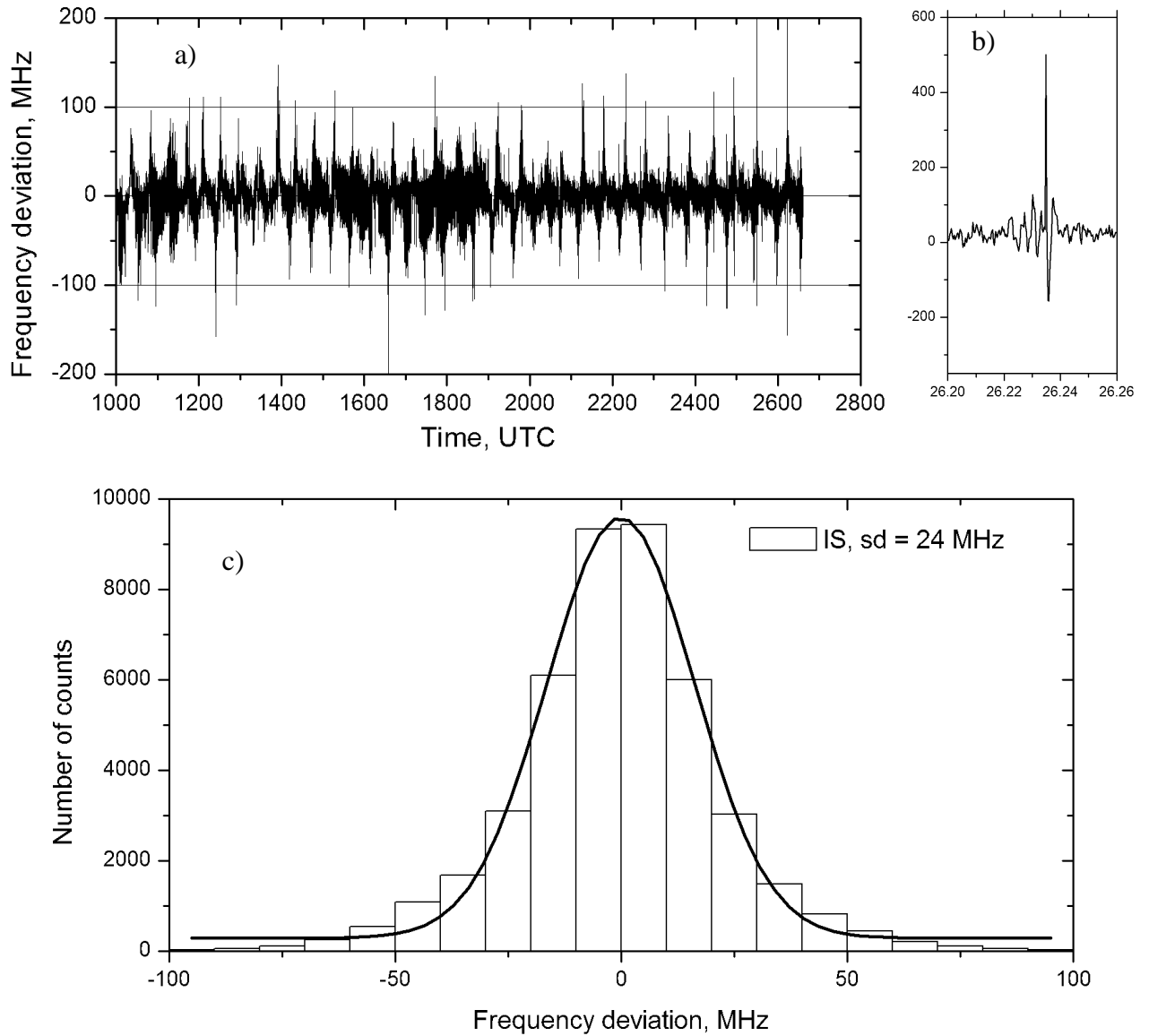
Fig.4.10 Frequency deviation of the IS during DIAL measurements on 01-02 Aug 2007: long-term trend (a), detailed picture of a mode hop (b) and statistical distribution (c). Here sd – standard deviation

This data set has a periodic structure due to temperature fluctuations in the trailer of the ground-based DIAL system, caused by an air cooling system (for the discussion see Subsection 6.3). At 1630 UTC and after the midnight there were several frequency jumps of $\approx 500\,$MHz (see Fig.4.10, b). They can be explained by lasing instabilities of the ECDL, when it approaches a limit of the mode-hop free zone. The spectrum of the emission starts jumping between two stable modes with an increasing amplitude. The frequency jitter of the ECDL decays with the further drift of the laser emission spectrum in the next stable zone.

A standard deviation of the given data set is 24 MHz (see Fig.4.10, c). Having an overall requirement of 200 MHz (1σ) for the accurate water-vapor measurement with a ground-based

DIAL (see Table 2.1), such a behavior of the IS can be accepted for measurements in the boundary layer as far as mode hops would be avoided. However, the requirement of the maximum frequency deviation of < 60 MHz, makes application of this IS rather challenging for water-vapor measurements in the upper troposphere. The specifications of the IS are summarized in Table 4.2 (regarding preliminary laboratory measurement and following in-field operation).

Table 4.2 Specification of the DLR IS based on TEC 500 modules (regarding initial specification and after the field experiment COPS).

Parameter	Value specified	Values measured during COPS
Tunability, nm	815… 840	815… 840
Mode-hop free range, GHz	>40	10-15
Linewidth, MHz (after Sacher-Laser)	<20	—[1]
Fiber out-coupled power, mW	20	<10
Frequency stability rms, MHz	<25	24
Channel cross-talk of OMP2, dB	<-65	-20
Response time of OMP2, µs	< 5	—[1]

1 – the value was not specified

For the water-vapor profiling of the atmosphere from the ground level up to the lowermost stratosphere, this IS has to be modified. The response time of the feed-back loop has to be decreased. When necessary, another stabilization technique has to be applied, for instance, stabilization on a wing of a resonance of a solid etalon. The revealed mode hops destroy the frequency stability as well as the spectral purity of the slave TISA laser. Further work for a better passive stabilization of the IS is required. If the long-term drift of the diode lasers can not be avoided for the in-field operation, the ECDLs may be replaced with more stable lasers with distributed feed-back (DFB) [Wirth et al., 2008].

Unfortunately, during the measurement campaign the fast optical switch OMP2 was damaged and was not able to obtain the specified value of the channel cross-talk. Therefore, the TISA transmitter of the DIAL system was operated with a single IS tuned at an online wavelength, whereas the unseeded output of the laser was taken for an offline signal (see Subsection 6.3).

4.3 Coupling of the seeding emission into the resonator

The output of the IS was coupled in the TISA resonator (see Fig. 4.11). The laser beam on the output of the fiber is collimated with the fiber collimator. Laser emission propagates the EOM and is coupled in the TISA cavity through an OC. To protect the fiber from an occasional high-
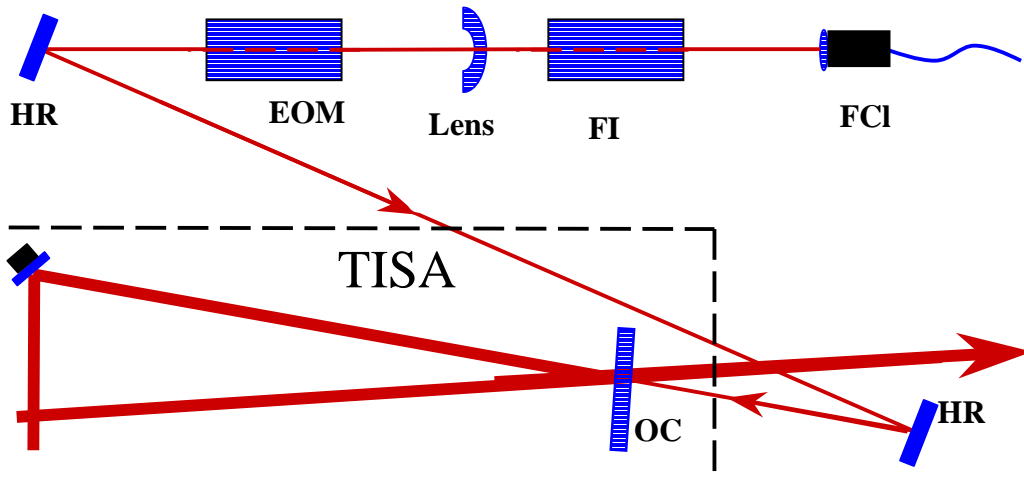
Fig.4.11 Coupling of the fiber output of the IS into the TISA cavity. Here FCl – fiber collimator, FI – Faraday isolator, Lens – negative lens of the beam shaper, EOM – electro-optical phase modulator, OC – output coupler, HR – high-reflective mirrors, CCD – CCD-camera.
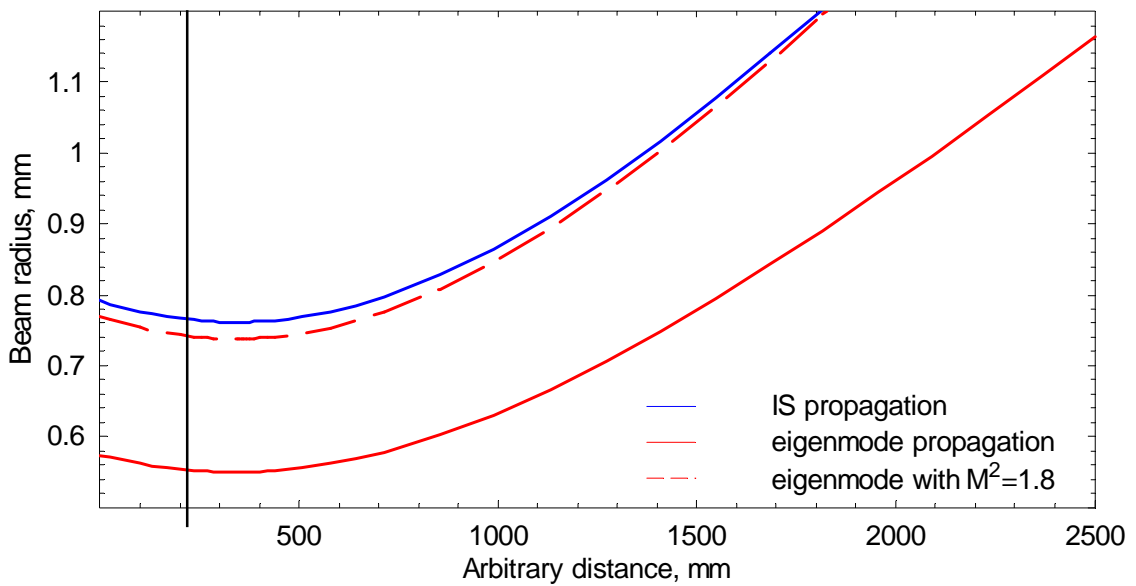
Fig.4.12 Fitting of the beam propagation of the IS (blue) to the eigenmode of the cavity (solid red). Dashed red line corresponds the intra-cavity mode with $M^2 = 1.8$. Waist position of the intra-cavity eigenmode is marked with a black line.

energy pulse from the TISA, a Faraday isolator was applied. The collimating lens in the collimator and a negative lens (with focal length of $f = -127$ mm) between FI and EOM build a beam-matching optics to fit the laser beam of the seeding emission to the intra-cavity eigenmode.

To coalign the IS-beam to the optical axis of the resonator, a propagation direction of the non-seeded TISA emission was marked, using an iris aperture and a CCD-camera. Ones defined, this

track can be used for the alignment of the IS beam. To simplify the tuning procedure, two HR mirrors were applied to realize a "beam walking" technique.

The propagation of the seeding beam was controlled with the CCD-camera to verify its fit to the cavity mode. Comparing the size and divergence of the laser beams, the best fit was found, assuming the beam quality of the seeder beam of $M^2 = 1.8$ (see Fig.4.12, dashed). The quality drop of the IS beam can be explained by its obscuration on a 2-mm aperture of the EOM crystal.

Chapter 5

Ti:sapphire transmitter

In the beginning of the TISA transmitter designing process, the performance of the laser was analyzed within boundaries of four models, considering certain properties of the laser.

- A model of thermal properties of the TISA crystal. When the laser operates at a high-average power, a significant part of the absorbed pump emission is dumped as heat in the crystal. This thermal load has an essential impact on the laser action. The crystal forms a thermal lens, affecting the eigenmode beam propagation in the cavity. The lifetime of the laser level is reduced with increase of the temperature. Thermal-induced aberrations influence the beam quality. Therefore, the thermal properties of the laser crystal must be carefully modeled and understood. A thermal model with a special concern of a Brewster-cut shape of the crystal was developed within [Wagner, 2009] (see Subsection 5.2).

- A resonator design model. It is necessary to define the cavity configurations allowing for a high-power operation. The thermal lensing must be considered, the laser has to operate close to a dynamically stable point, TEM_{00}-mode has to be preferred and the beam propagation has to be corrected for astigmatism (see section 5.3).

- A model for the laser pulse evolution. Applying of a rate equations approach allows to find an optimum output coupler reflectivity and to calculate a slope efficiency of the laser, a build-up time and duration of the pulse (see App. A). Comparison of the simulation and the experiment is presented in the Subsections 5.4.2 and 5.5.2 for measurements at 935 nm and 820 nm, respectively.

- Laser spectrum simulation. Spectral density of the stimulated emission cross-section of the TISA, spectral properties of the intra-cavity elements were taken into consideration to

optimize the transmitter for the wavelength of interest. The corresponding calculations are presented in Subsections 5.4.1 and 5.5.1 for the set-up of the airborne and the ground-based system, respectively.

In the following sections these models are detailed and applied to simulate the optimum TISA laser, matching the requirements for the DIAL transmitter (see Table 2.1). Taking the modelling results for a basis, the TISA transmitters for the airborne and the ground-based water-vapor DIAL systems were built and specified (see Subsections 5.4 and 5.5).

5.1 Ti:sapphire crystal

TISA is a solid-state laser material with a high thermal conductivity, chemical inertness and mechanical rigidity. First laser action was reported in 1982 [Moulton, 1982]. TISA is one of the most widely tunable lasers with a tuning range from 700 to 1100 nm (see Fig. 5.1), which can be operated continuous wave (cw) and in a pulsed mode. As a four-level system (see Fig. 5.2) a TISA laser provides a low lasing threshold and a high conversion efficiency. The transitions between the pump level and the upper laser level as well as between the lower laser level and the ground-state are significantly faster than the laser transition and can be neglected in the rate equations for TISA [Wagner, 2009]. However, the relaxation time of the upper laser level of $\tau = 3.2$ µs must be considered for the adequate simulations of the seeded and, especially, free-running laser operation of a pulsed TISA laser with a cavity length of L $\gtrsim$ 1 m (see App. A).

5.2 Thermal model

5.2.1 Crystal cooling

For experiments two crystal rods were grown using a heat-exchange technology with diameters of 7±0.001 mm and lengths of 20±0.01 mm. Their end-surfaces were cut at a Brewster-angle of 60.5° regarding the optical axis with the c-axis of the crystal parallel to the polarization plane of the propagating light. The doping level of Ti^{3+}-iones is $\approx 0.15\%$ (weight), absorption coefficient is $\alpha_{514} = 1.8…1.9$ cm^{-1} at 514 nm and figure of merit $FOM = 380$. The rods were manufactured in the company FEE GmbH, Idar-Oberstein, Germany.

To optimize the TISA laser for a high average pump power, special construction of the crystal heat sink was developed in collaboration with the National Centre of Atmospheric Researches.
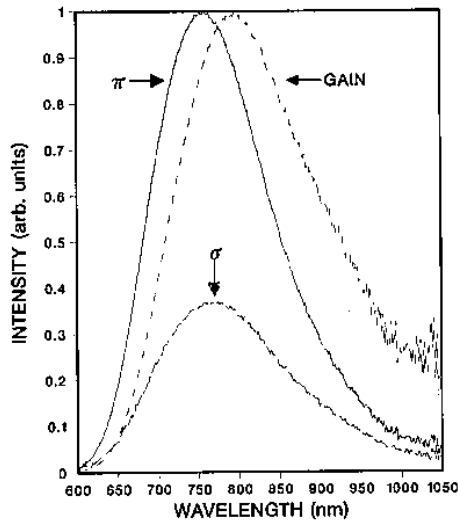
Fig.5.1 TISA polarized fluorescence spectra and calculated gain line shape [Moulton, 1986].
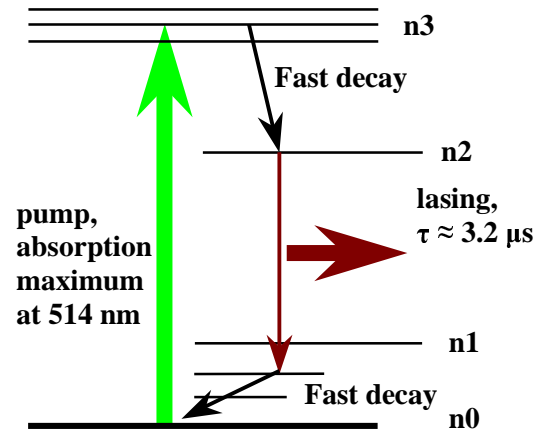
Fig.5.2 Energy level scheme in the TISA [e.g, Moulton, 1986].
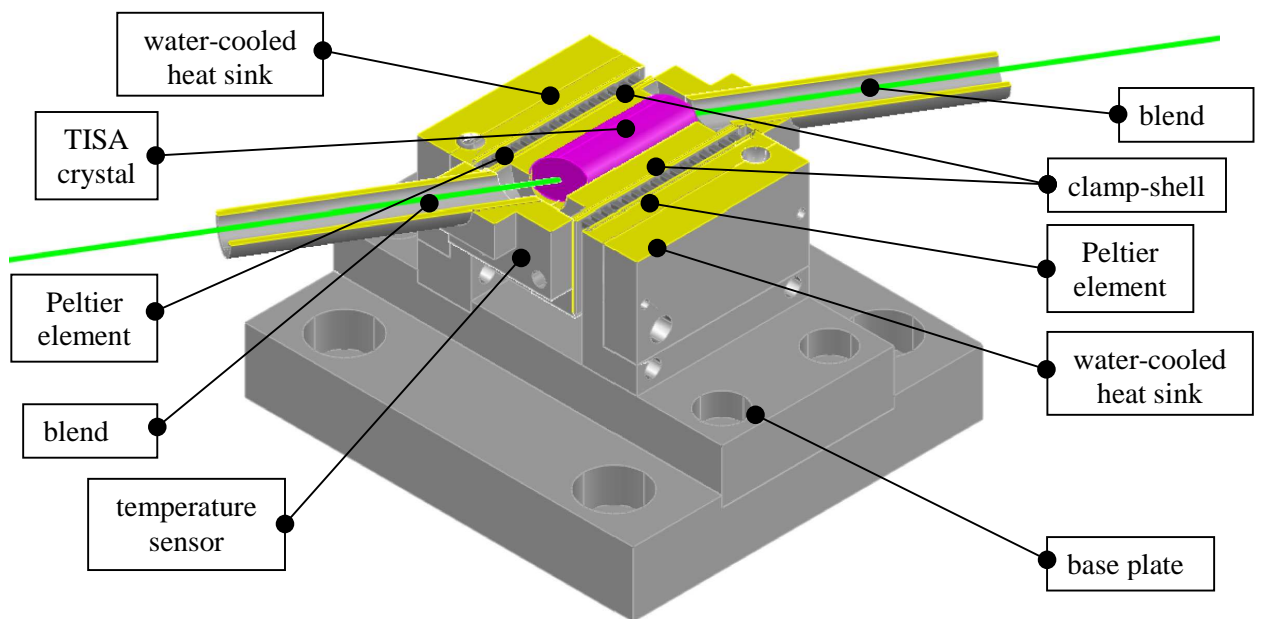
Fig.5.3 Scheme of the clamp-shelled TISA crystal mounted into the heat sink (courtesy of Gerd Wagner, IPM, Uni Hohenheim).

Its application significantly improved heat removal from the rod and allowed for the temperature control of latter with a precision better 0.1° Celsius. Here the crystal is mounted in an aluminium cooler, two aluminium plates with a cylindrical bore made with an uncertainty of ±5 μm. The bore diameter of each clamp-shell pair was measured using an etalon rod with a precision of ±1 μm. The bore surface was gold coated, and the layer thickness was calculated to obtain the best fit of the TISA rod. A high gold plasticity yields optimum mechanical and, therefore,

thermal contact between the clamp-shells and the crystal in spite of remaining surface irregularities.

Figure 5.3 presents the heat-sink schematic. The outer surfaces of the clamp-shells are in contact with peltier elements, and other surfaces are air-cooled. Temperature of the peltier elements is controlled by an external driver, using a sensor mounted in the clamp-shell. The outer surfaces of the peltier plates are pressed into aluminium water-cooled heat sinks. In the experiment temperature of the clamp shells was set to 15°C to keep the upper-laser-level lifetime long and, therefore, the laser efficiency high [Moulton, 1986]. Operation at lower temperatures was avoided to prevent condensation of atmospheric water vapor on the crystal surfaces.

For a better temperature control, the heat-sink module was mounted on an isolating plate. The 5 cm long blends are used to reduce risk of dust contamination: during operation at a high power even a tiny dust particle may cause a severe damage of the end-surface of the TISA crystal.

5.2.2 Building the thermal model

A fraction of the pump emission absorbed in the TISA material is utilized for its heating, causing spatially-inhomogeneous temperature increase over the rod. The refraction index grows proportionally to the temperature, building a so-called 'thermal lens' in the crystal. To define parameters of the thermal lens in the pumped rod, detailed spatial and temporal temperature distribution has to be derived first. The thermal model for the end-pumped Brewster-cut TISA crystal was build by Gerd Wagner, IPM [Wagner et al., 2005; Wagner, 2009]. The clamp-shells and the transition layer with their own properties were concerned for the calculation.

Figure 5.4 shows the calculated focal lengths of the thermal lens for different pump fluencies, for the laser operation at 820 nm and at 935 nm, assuming difference in the fraction of the pump power converted into heat. The simulation for a Brewster-cut TISA rod was performed in a parabolic approximation separately for two orthogonal planes: tangential, defined by the rod axis and the end-surface normals, and sagittal. The pump beam radius is 1.05 mm (at the energy level of $1/e^2$ from maximum). The modeling shows clear difference of the thermal lens strength in sagittal and tangential plane, caused extensively by the Brewster-cut shape of the rod. Although the TISA birefringence contributes the astigmatism of the thermal lens as well, its impact is far too low. The astigmatic thermal lens causes deformation of the eigenmode of the cavity, forming elliptical cross-section of the laser beam and decreases an overlap between the pump beam and the TEM_{00} in the crystal.

The theoretical investigations were complemented with an experiment (see Subsection 5.2.4).
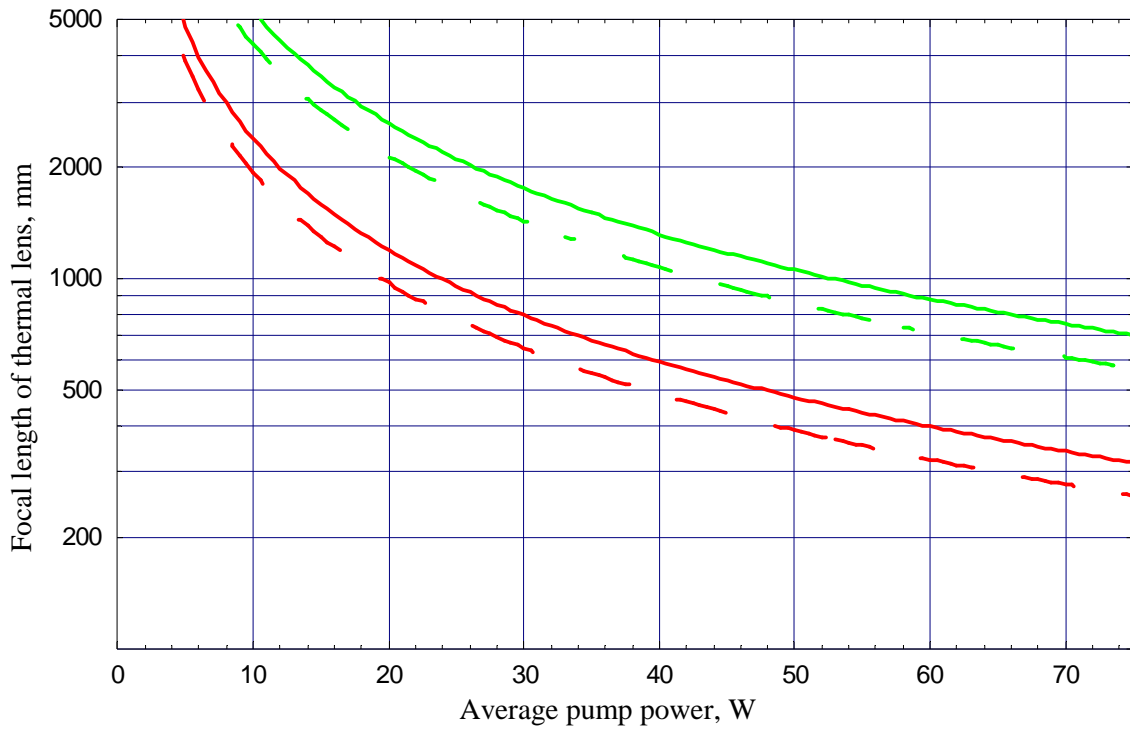
Fig. 5.4. Calculated focal lengths of thermal lens for Brewster-cut crystal [Wagner, 2009]. Pump beam diameter 2.1 mm. Values in tangential plane marked red, in sagittal – green. With a solid curve are plotted results for simulation of the laser operation at 820 nm, with a dashed curve – at 935 nm.

5.2.3 Optical damage threshold of the Ti:sapphire

For optimum energy conversion the size of the pump beam on the crystal should fit the size of the resonator eigenmode. While designing the cavity configuration, spot size has to be chosen as small as possible to obtain the highest gain in the pumped volume. The minimum beam diameter is limited by laser-induced damage thresholds (LIDT) of the high-reflective mirrors with dielectric coatings (HR) and the TISA crystal at the wavelengths of the pump and TISA laser emissions.

The best commercial HR-mirrors are specified for a surface LIDT of 10 J/cm^2 (532 nm, pulse length 10 ns (FWHM), pulse repetition rate 10 Hz). For the TISA crystal, the value of this parameter differs from one producer to another about factor of ten, from 20 to 100 J/cm^2 for the same measurement conditions. The value of 20 J/cm^2 was taken for the estimation. In the current system, the pump laser provides pulses of a near-Gaussian shape with a maximum pulse energy of $\approx$ 180 mJ, pulse length of 20 ns at a rate of 250 Hz (see Table 3.1). Inside a ring resonator, one pulse at the wavelength of the transmitter contains $\approx$ 60 mJ of energy (at the output energy of 20 mJ and an output coupler with reflectivity of 70%).

The pump laser has the repetition rate higher then 10 Hz. Hence, the expected value of the LIDT has to be decreased in $\sqrt[4]{f/f_r}$ times [BVG, 1997], or even in $\sqrt{f/f_r}$ times [Fix, 2006], with f – repetition rate of the experiment laser, f_r – rate of the reference laser. On the other hand, a longer pulse of the current pump laser gives the 2-times advantage. Thus, the values of the surface LIDT of the optics in the experiment has to be read as 4 J/cm^2 for HR-mirrors and 8 J/cm^2 for TISA crystal.

While choosing the optimum pump beam size, some other issues has to be considered. The HR-mirrors directing the pump beam are affected only by the energy at 532 nm from the pump laser, and the intra-cavity HR-mirrors are interacting only with the near-IR TISA emission. The TISA rod is irradiated with both pump and resonator beams with a high temporal and spatial overlap. Pumping of the crystal from both sides yields halving the incident pump energy per surface. When the waist of the pump beam locates on the TISA crystal and the energy density on the HR-mirrors is significantly smaller, the optimization of the pump beam and the eigenmode parameters can be performed only solely with respect to the damage threshold of the laser rod.

The lasing was assumed safe at the energy density of the pump beam at a half of the LIDT of the TISA crystal, the Brewster-angle cut of the rod was concerned, and the minimum pump beam size was calculated regarding the peak energy density. The beam radius of 0.85 mm (at 1/e^2 level of energy from maximum) was calculated for the pump pulse energy of 90 mJ pumping from both sides, 0.8 mm was used in the experiment. The intra-cavity pulse has a smaller energy, is temporary separated from the pump and, therefore, can be neglected in a first approximation. Nevertheless, it must be considered for resonator design calculation with respect to a LIDT of the intra-cavity optics.

5.2.4 Thermal lens measurements

The set-up for the thermal lens measurement in the TISA crystal is similar to one used later for lasing operation of the transmitter (see Fig.5.5). To measure the focal length of the thermal lens, a probe beam from the ECDL was sent through the pumped laser rod and its further propagation was recorded with a CCD-camera, mounted on a rail. Moving the camera along the rail, around 20 shots of the beam cross-section were recorded; the region around the beam waist and at least double Relay range in each direction was mapped for the confident definition of beam parameters. The location of the beam waist depends on the pump power level. To constrain waist position for a certain area, an additional positive lens with $f = 570$ mm was applied. The waist position of the initial probe beam locates in the rod (waist radius 0.4 mm, divergence $\approx$ 1 mrad).
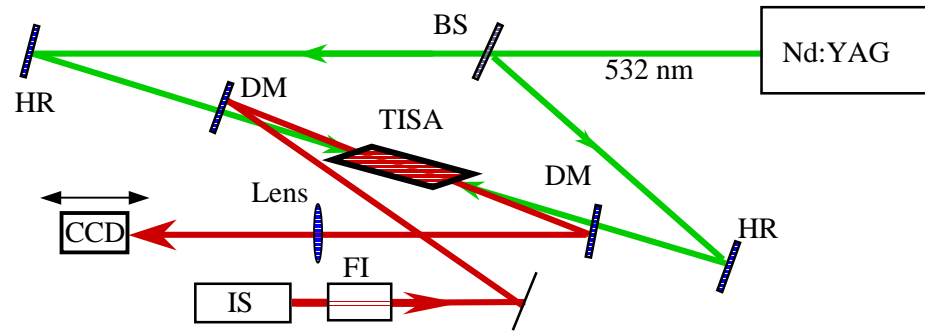
Fig.5.5 Scheme of the set-up for a measurement of the thermal lens. Here BS – beam splitter, HR – high-reflective mirror, DM – dichroic mirror, IS – injection seeder, FI – Faraday isolator, CCD – CCD camera.
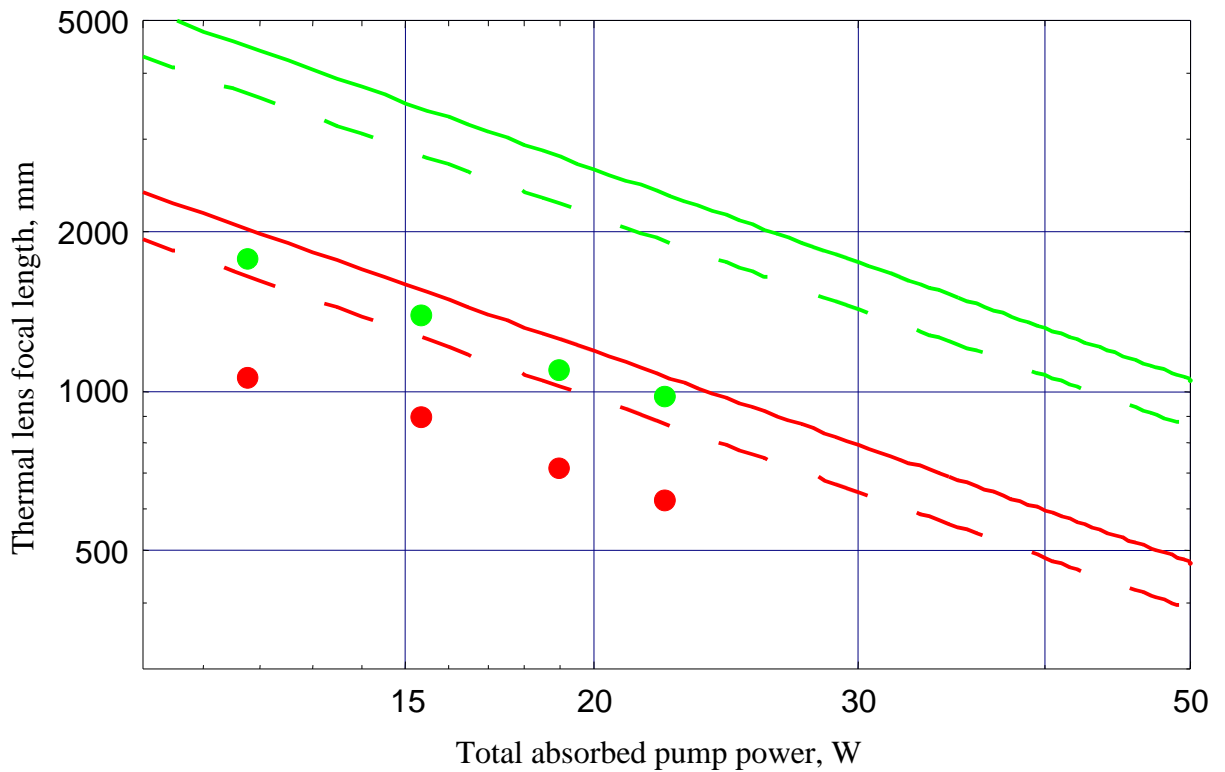
Fig.5.6 Experimental and theoretical values of the thermal lens focal length in a Brewster-cut crystal rod vs. absorbed pump power. For the pump laser in configuration Pump-1, measured values marked with points, theoretically derived values [Wagner, 2009] are drawn with curves. Values in tangential plane marked red, in sagittal – green. With a solid curve the results for simulation of the laser operation at 820 nm are plotted, with a dashed curve – at 935 nm. Beam diameter 2.1 mm.

The stored profiles were loaded in a "Beam Analyzer" program (TU Berlin) to define the waist position and the relay range. Comparing these beam parameters for each pump power level with corresponding parameters of the probe beam, propagating the rod without a thermal load, the strength of the thermal lens was derived.

Figure 5.6 presents experimental values of the thermal lens focal length in the TISA rod regarding total pump power, absorbed in the crystal. The plot is drawn in a log-log-scale. The experimental results can be approximated with a potential function within a measurement uncertainty. The measurements were performed for the power levels of 12, 15, 19 and 23 W in pump laser configuration Pump-1 with pump beam diameter 2.1 mm (at the level $1/e^2$) and maximum energy density in the peak of 2.6 J/cm^2. No special measurement for the configuration Pump-2 was performed. For the last one some weaker values of the TL for the same pump level as in Pump-1 were expected due to a worse overlap with the eigenmode of the cavity (see Fig. 3.7 for the pump beam cross-sections). Theoretical values from Fig. 5.4 are also depicted here.

The experiment confirmed the theoretically predicted discrepancy between thermal lens values in tangential and sagittal plane of the TISA rod. The slope of the dependency is the same as in the simulation, though a clear shift of the experimental data toward the shorter focal lengths has to be mentioned. This can be explained by difference in operation conditions in the experiment and assumed for the simulation. In the model a lasing operation is simulated with a 20-40 % conversion of the absorbed power into laser emission, whereas no lasing was allowed during the experiment and, obviously, a large fraction of the pump energy was converted into heat. Limitations of the model due to the applied parabolic approximation of the temperature profile and coefficients uncertainties, may also contribute the difference.

From the other side, the energy distribution in the cross-section of the pump beam in the experiment differed from the ideal Gaussian one. Having a higher energy density in the center, the real beam may yield a higher thermal load in the axial zone. An increased thermal resistance between the rod and the clamp-shells may cause a smaller heat flow and, hence, a higher temperature of the crystal. The size of impact of these factors is currently under investigation.

5.3 Resonator design

The certain features must be taken into consideration while design the laser resonator of the DIAL transmitter. First, operation at a high peak power and high energy density has to be allowed. The principle mode, TEM$_{00}$, should be preferred for operation. Thermal lensing must be

Fig.5.7 Principle scheme of the TISA ring-resonator, evoluted. Here L1 – the air gap which beam propagates from TISA to the lens, L2 – the air gap which beam propagates from lens to the TISA, closing the loop. L1+L2 gives roughly the resonator length.

considered with respect to the dynamical stability of the resonator eigenmode. The beam propagation has to be corrected for astigmatism. Single-frequency operation and injection seeding has to be allowed. Therefore, an unidirectional single-rod ring cavity with a cylindrical lens was selected. Resonator parameters were calculated in a paraxial approximation using a matrix formalism, which yields sufficient precision [Hodgson, 1996, p.76].

The intra-cavity beam propagation is described by two ABCD-matrixes, comprised by corresponding propagation matrixes of the resonator components separately for tangential and sagittal plane. For the ring resonator depicted on the Fig.5.7 with a Brewster-cut crystal with an axial length l and a refraction index n, with a thermal lens focal lengths ft_t and ft_s, with air gaps $L1$ and $L2$, with an astigmatic lens with focal lengths f_t and f_s, the matrixes are:

$$M_t = M_{L2} M_{f\_t} M_{L1} M_{TISA\_t} = \begin{pmatrix} 1 & L2 \\ 0 & 1 \end{pmatrix} \begin{pmatrix} 1 & 0 \\ -1/f_t & 1 \end{pmatrix} \begin{pmatrix} 1 & L1 \\ 0 & 1 \end{pmatrix} \begin{pmatrix} 1 & Lc/n^3 \\ -1/ft_t & 1 \end{pmatrix} = \begin{pmatrix} A_t & B_t \\ C_t & D_t \end{pmatrix}$$

$$\tag{5.3}$$

$$M_s = M_{L2} M_{f\_s} M_{L1} M_{TISA\_s} = \begin{pmatrix} 1 & L2 \\ 0 & 1 \end{pmatrix} \begin{pmatrix} 1 & 0 \\ -1/f_s & 1 \end{pmatrix} \begin{pmatrix} 1 & L1 \\ 0 & 1 \end{pmatrix} \begin{pmatrix} 1 & Lc/n \\ -1/ft_s & 1 \end{pmatrix} = \begin{pmatrix} A_s & B_s \\ C_s & D_s \end{pmatrix}$$

The resulting propagation matrixes depend on the first component of the round-trip and the propagation direction. This represents the variation of the beam fundamental parameters (w_0, zr, z) along the resonator. In the given matrixes the round-trip starts from left principle plane of the crystal through the rod toward the air gap $L1$, thus describing the eigenmode behavior between the lens and the rod in the air gap $L2$.

To define the cavity parameters, namely $L1$, $L2$, ft_t and ft_s, the constraints of the eigenmode propagation and the dynamic stability has to be applied to the resonator matrix. Regarding [Hodgson, 1996, p.76], the principal mode of a Laguerr-Gaussian beam in a free space at a position z can be extensively described in a paraxial approximation via the q-parameter:

$$\frac{1}{q(z)} = \frac{1}{\pi w_0^2 \frac{\lambda}{\lambda}\left(\frac{z\lambda}{\pi w_0(z)^2} + \frac{\pi w_0(z)^2}{z\lambda}\right)} - i\frac{1}{\pi w_0^2 \frac{\lambda}{\lambda}\left(1+\left(\frac{z\lambda}{\pi w_0(z)^2}\right)^2\right)} = \frac{1}{R(z)} - i\frac{\lambda}{\pi w(z)^2}, \tag{5.4}$$

where $R(z)$ and $w(z)$ are the phase and beam radius at the position z, respectively, w_0 is the waist radius of the eigenmode. An optical system, described by an ABCD-matrix, transforms the q-parameter of the beam from q_1 at the input plane to $q_2 = (Aq_1 + B)/(Cq_1 + D)$ at the output plane. Handling the reproducibility of the beam parameters in the stable resonator after a round-trip: $q_2 = q_1 = q$, – one gets the eigenmode propagation constraint for the ABCD-resonator:

$$\frac{1}{q'} = \frac{D-A}{2B} - i\frac{\sqrt{4-(A+D)^2}}{2B} \tag{5.5}$$

with q' – the q-parameter of the eigenmode at the intra-cavity element, where the round-trip of an ABCD-matrix calculation was started. From Eqs.5.4, 5.5 the beam waist radius $w_{0,i}$, the distance from the beam waist position regarding starting point of the round-trip z_i, and the eigenmode size on the crystal $w_{c,i}$ are

$$w_{0,i} = \sqrt{\frac{\lambda}{\pi} \frac{2B_i/\sqrt{4-(A_i+D_i)^2}}{1+(D_i-A_i)^2/(4-(A_i+D_i)^2)}}, \tag{5.6}$$

$$z_i = \frac{2B_i/(D_i-A_i)}{1+(4-(A_i+D_i)^2)/(D_i-A_i)^2} \tag{5.7}$$

$$w_{c,i} = \sqrt{\frac{\lambda}{\pi} \frac{2B_i}{\sqrt{4-(A_i+D_i)^2}}}, \tag{5.8}$$

with $i = t,s$ for tangential and sagittal plane, respectively. To obtain the dynamical stability of the resonator, a configuration has to be found when dependence of the eigenmode size on the rod from the value of the thermal lens $w_{c,i}(f_t)$ has its minimum. Then the variation of the pump power does not influence the size of the cavity mode. This boundary can be formalized as $\frac{\mathrm{d}w_{c,i}(f_t)}{\mathrm{d}f_t} = 0$.

In a ring resonator with a single crystal this condition fulfils when $A_i + D_i = 0$ and, therefore,

$$w_{c,i}\Big|_{f_t = f_{t,optim}} = \sqrt{\frac{\lambda}{\pi}B_i}. \tag{5.9}$$

5.4 Ti:sapphire transmitter for airborne and space borne measurements

5.4.1 Ti:sapphire set-up

The band of lines around 935 nm was found optimum for the operation of an air-borne water vapor DIAL, regarding boundaries summarized in Subsection 2.2: here are present the absorption lines with a large absorption cross-section for water-vapor profiling of the upper troposphere as well as the lines with a small absorption cross-section for measurements in a lower troposphere (see Table 5.1).

Table 5.1 Suitable water-vapor absorption lines in region of 935 nm (by Hitran database). Here S – intensity of the absorption line; γ_{air} – air broadened width of the line (HWFM); γ_{self} – self broadened width of the line (HWFM); E'' – lower-state energy.

Wavenumber vacuum, cm^{-1}	Wavelength vacuum, nm	S, cm^{-1}/cm^{-2}	γ_{air}, cm^{-1}/bar	γ_{self}, cm^{-1}/bar	E$''$, cm^{-1}	Notes
10684.8292	935.9064	3.81E-24	0.0878	0.4654	383	weak
10688.7726	935.5611	4.70E-23	0.0844	0.3500	488	medium
10687.3630	935.6845	5.42E-22	0.0912	0.5000	137	strong
10685.3200	935.8634	7.39E-26	0.0916	0.0000	226	offine

Using the information on the absorption lines from [ESA, 2000] they were checked for applicability in different atmospheric conditions regarding the procedure formalized in Subsection 2.2. An absorption cross-section of each line was calculated and offline zones were defined. The cross-section of the ith line is $\sigma_i = S_i(T)V_i(\tilde{\nu}, p, T)$, where V – Voigt function, the convolution of the area normalized Lorentzian-shaped water-vapor absorption line and the area-normalized Gaussian-shaped Doppler line [Di Girolamo et al., 2004]. Figure 5.8 depicts spectrum distribution of the water vapor absorption cross-section in the vicinity of 935 nm for US Standard atmosphere conditions at the sea level ($T = 288.2$ K, $Rh = 45.88\%$, $p_{H20} = 7.8$ hPa).

To comply the demand of the narrow-bandwidth lasing, spectral properties of all the components of the laser has to be considered, namely the reflectivity spectrums of the coatings of HR-mirrors, an output coupler (OC), an intra-cavity lens, as well as the gain spectrum of the TISA. Ideally, the superposition of these spectrums should allow for a small-signal round-trip intra-cavity signal amplification of $G > 1$ only for a single longitudinal mode.

After [Moulton, 1986] the gain spectrum of the TISA is approx. 300 nm broad with its maximum at 800 nm (see Fig.5.9, black). The reflectivity spectrum of a commercial HR laser mirror with a
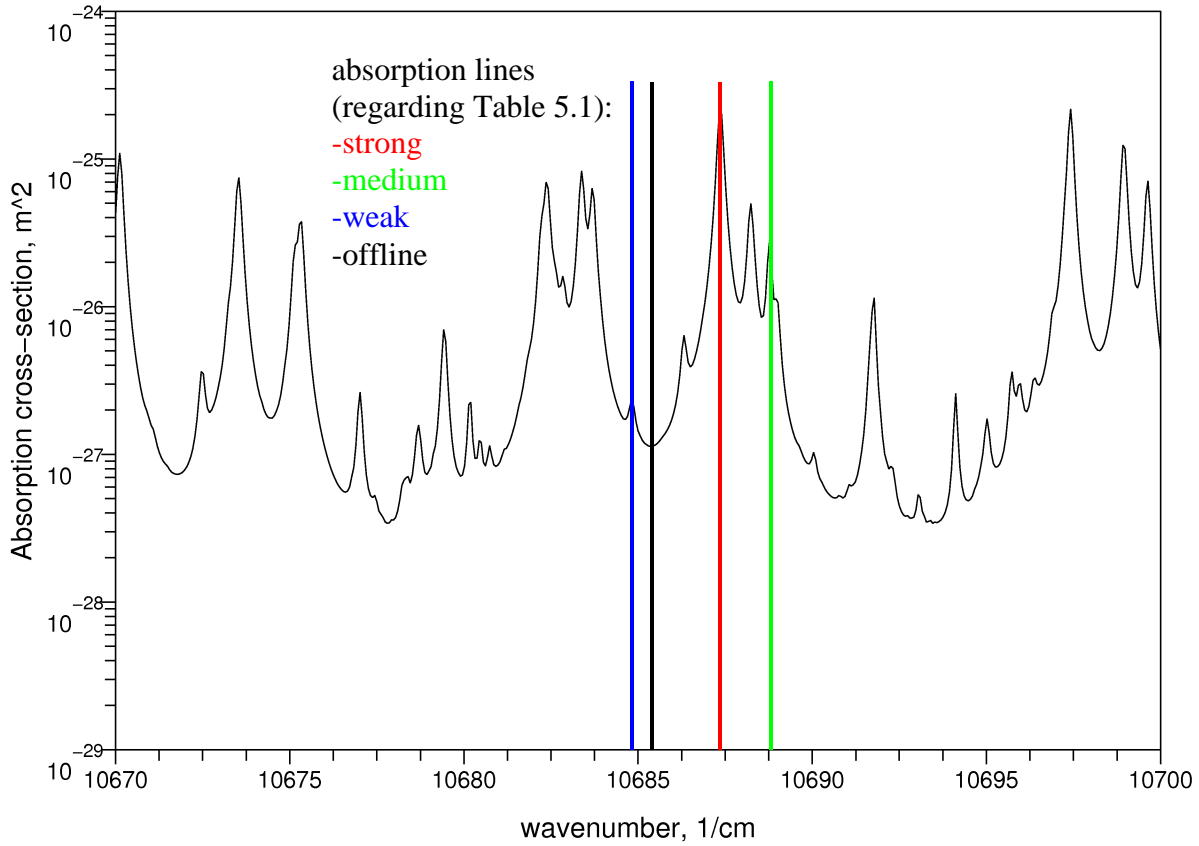
Fig.5.8 Spectrum of the water-vapor absorption cross-section for US Standard atmosphere on the sea level for the absorption lines around 935 nm.
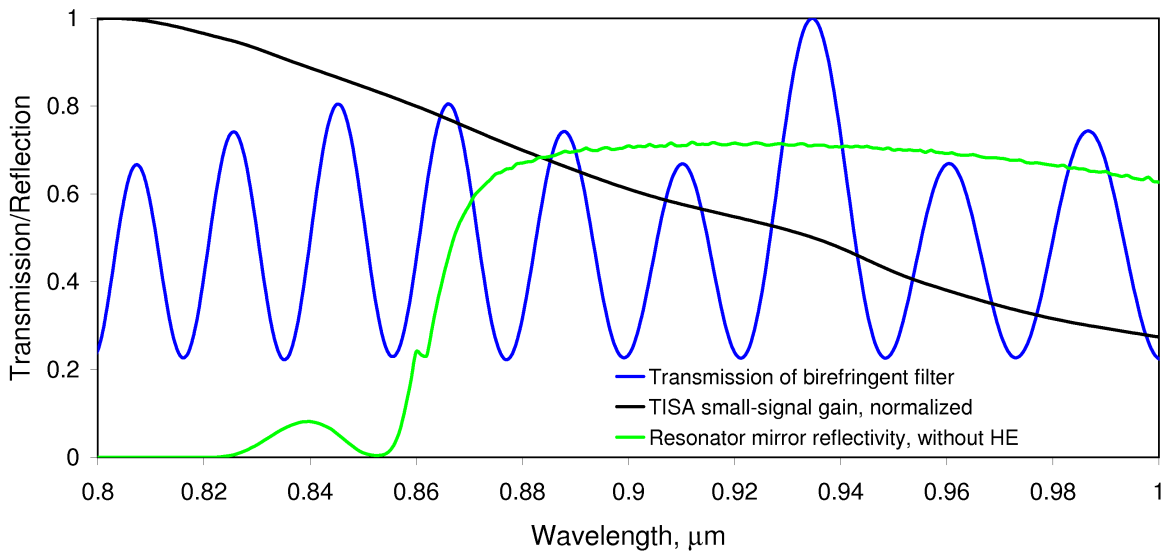
Fig.5.9 Calculated spectral efficiency of the intra-cavity elements of the TISA set-up at 935 nm: TISA small-signal gain, normalized (black); calculated transmission spectrum of the 3-plate BF, optimized for 935 nm (blue); round-trip reflectivity of the three HR and 70% OC of the Z-shape ring cavity (green).
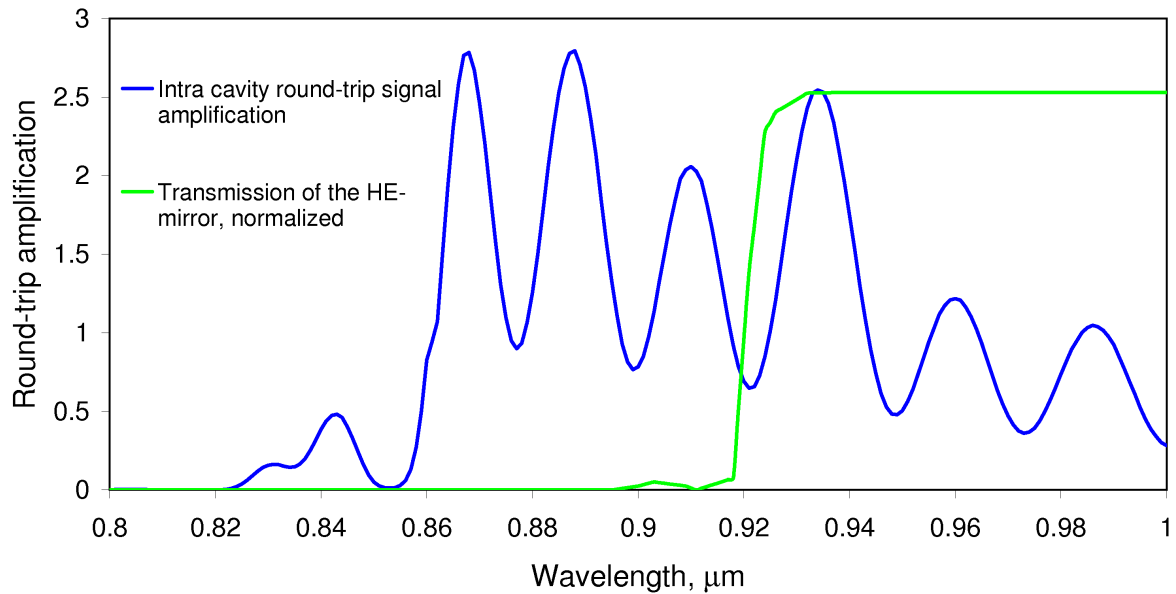
Fig.5.10 Calculated spectrum of the small-signal intra-cavity round-trip amplification in the TISA laser at 935 nm. Cavity round-trip amplification without HE-mirror (blue), reflectivity of the HE-mirror, normalized to the peak of round-trip amplification (green).

dielectric coating optimized for a 0° incident angle obtains $R = 99,5$ % at the maximum at 935 nm, $R = 99\%$ at 885 nm and then drops within next 30 nm to 5-6%. Without additional spectrum-defining intra-cavity components such a TISA laser will operate at 870-880 nm (see Fig.5.9, green, includes 70% OC).

Further spectral narrowing was performed using a birefringent filter: a set of flat crystal quartz plates of different thicknesses, mounted in the cavity at a Brewster-angle to the eigenmode (see Subsection 4.1.1). For the experiment at 935 nm, a 3-plate BF with thicknesses of the plates of 0.85, 1.7 and 3.4 mm was applied. Using Eq. 4.3, a transmission spectrum of the BF was calculated (see Fig.5.9, blue). To obtain the maximum transmission of the BF at 935 nm, the angle between the optical axes of the plates in the set and the polarization plane was set to 55°.

Figure 5.10 (blue) depicts the estimated spectral distribution of the small-signal round-trip amplification in the TISA-laser cavity with the BF. The peak amplification was calculated with Eq. A.7 for the maximum gain cross-section of $\sigma = 2.7*10^{-19}$ cm^2, the absorbed pump pulse energy of 95 mJ, the pump beam radius of 0.8 mm and the 90% overlap efficiency (see App. A). The spectrum of the laser emission is limited to the region with a round-trip amplification $G > 1$.

The amplification at 935 nm is > 2, but in the region 870-890 nm it is > 2.5. To suppress the short-wave spectrum, a resonator mirror with a specially designed dielectric coating, the so-

called 'hard-edge' mirror (HE), was applied (see Fig. 5.10, green). The reflectivity spectrum of this mirror has a 'step', so that it acts as an HR mirror for the wavelengths beyond 930 nm, providing $> 97\%$ losses in the region < 920 nm. Changing the incident angle, the reflectivity 'step' can be shifted as close as possible to the 935 nm to obtain the required wavelength selection. The optimum incident angle was found at $\approx 15°$.

For the fine wavelength selection, the injection seeding technique was implemented (see Subsection 4.1). This method is especially effective for ring lasers, where the seeding emission can be coupled in a cavity of a slave laser not through the HR-mirror but through the output coupler, thus increasing the coupling efficiency. At a high seed power and sufficient spatial overlap of the eigenmode and the IS beam, the slave laser will run either single or dual longitudinal mode, depending on the offset of the IS frequency from the closest cavity resonance. In the experiment the ECDL Toptica DL100 with an output power of 20 mW cw was implemented.

For the measurements at 935 nm, only the first modification of the pump laser Pump-1 with maximum output energy of 100 mJ in a pulse was available (see Chapter 3). Taking into account energy losses between the pump laser and the TISA crystal caused by, e.g., leak through HR-mirrors, reflection on the lenses of the telescope and on the dichroic mirrors, transmission through TISA-crystal, only around 90 mJ of the pump energy was absorbed in the rod. This corresponds to a focal length of the thermal lens of 600 mm and 920 mm in tangential and sagittal plane, respectively (see Fig.5.6). The ring cavity with a length of 1350 mm was chosen.

Figure 5.11 depicts the radius of the TEM_{00}-mode along the resonator, obtained using Eqs. 5.6-5.8. In this configuration, the eigenmode radius in the TISA crystal is 0.65 mm. It is less than the pre-selected pump beam radius of 0.8 mm, derived with respect to the damage threshold of the resonator components. The smaller radius is caused by the selection of the shorter cavity length to improve the stability of the resonator.

To compensate the astigmatism, induced by the thermal lens in a crystal with Brewster-cut end-surfaces, an intra-cavity cylindrical lens is required. However, in the current experiment using of the lens was omitted to reduce the passive losses and increase the conversion efficiency. It does not affect the overlap with the pump beam, because the eigenmode cross-section in the rod is circular (see Fig. 5.11).

Figure 5.12 depicts the stability zone of the resonator: the eigenmode size on the rod with respect to the thermal lens focal length (solid curves) and absorbed pump energy (dashed curves).
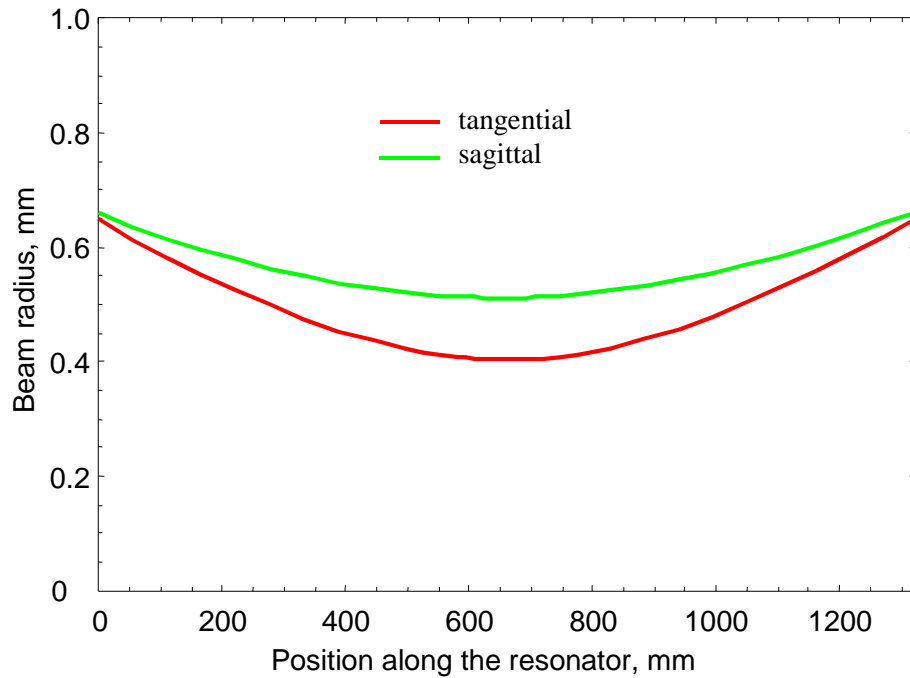
Fig.5.11 Calculated radius of the eigenmode along the resonator in tangential (red) and sagittal (green) plane, respectively. The 0-position corresponds the first principle plane of the TISA.
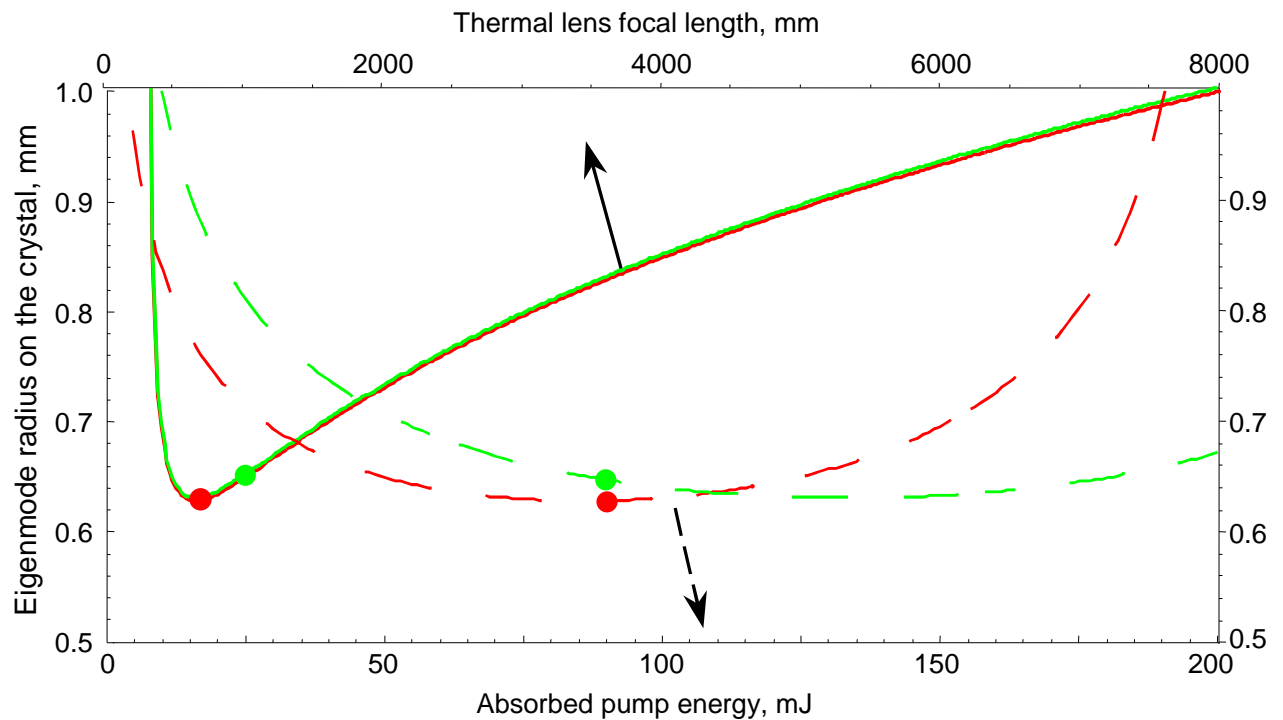
Fig.5.12 Calculated radius of the TEM_{00} in the crystal rod with respect to the thermal lens focal length (solid curves) and absorbed pump energy (dashed curves) in tangential (red) and sagittal (green) planes. The radii values corresponding the maximum pump power are marked with disks. The correlation between the thermal lens values and the pump power was established regarding the experiment described in Subsection 5.2.4.

The dynamic stability of a resonator is obtained, when the eigenmode size in a crystal – and therefore the spatial overlap with a pump beam – does not depend on variation of a pump power or, in terms of a functional dependence of the mode size from the pump power, in the extremum of this function. Varying the cavity length, a laser can be optimized with respect to the given strength of the thermal lens in both planes. In a single-crystal cavity without intra-cavity lenses the shape of stability zone with respect to the thermal lens values is similar in the tangential and sagittal plane.

Temperature variations as well as mechanical instability of the resonator elements have to be minimized to obtain the strict stability requirements for the DIAL transmitter (see Table 2.1). The passive stabilization was obtained using a rigid optical bread-board and optical mounts with a low temperature expansion coefficient At the online wavelength a strong water-vapor absorption induces for a building-up laser pulse additional ~10% dissipative losses per round-trip (see App. A). Hence, for a stable laser operation the cavity volume was sealed and purged with nitrogen.

Considering all requirements and limitations, the following layout of the TISA laser was built for the experiment in the wavelength region around 935 nm (Fig. 5.13). Here the beam from the pump laser propagates to a 50%-beam splitter (BS) through a lens combination, obtaining the optimum overlap of this beam and the eigenmode of the resonator in the crystal rod. Reflected by two high-reflective (HR) mirrors, the pump emission enters the laser rod from both sides. The first lens in this beam shaper enlarges the beam while the second focuses it on the rod. This configuration forms a convergent beam with the waist locating in the crystal plane and a large spot size on the bend mirrors, avoiding their optical damage. To obtain the similar energy distribution on both surfaces of the TISA rod in this layout, distances from the BS to the crystal in the both branches must be kept equal, decreasing the flexibility of the set-up.

Using an energy leak through one of the HR-mirrors, position and size of the pump beam is monitored continuously with a CCD-camera, verifying its overlap with the intra-cavity eigenmode.

A z-shape ring cavity comprises two dichroic mirrors (DM), the HE mirror, glued on a piezo actuator for the resonator length adjustment, and an output coupler (OC). To provide an unidirectional cavity propagation, a combination of a 15° Faraday rotator (FR) and a halfwave plate ($\lambda/2$) was implemented. A birefringent filter (BF) for a coarse spectral selection was applied.
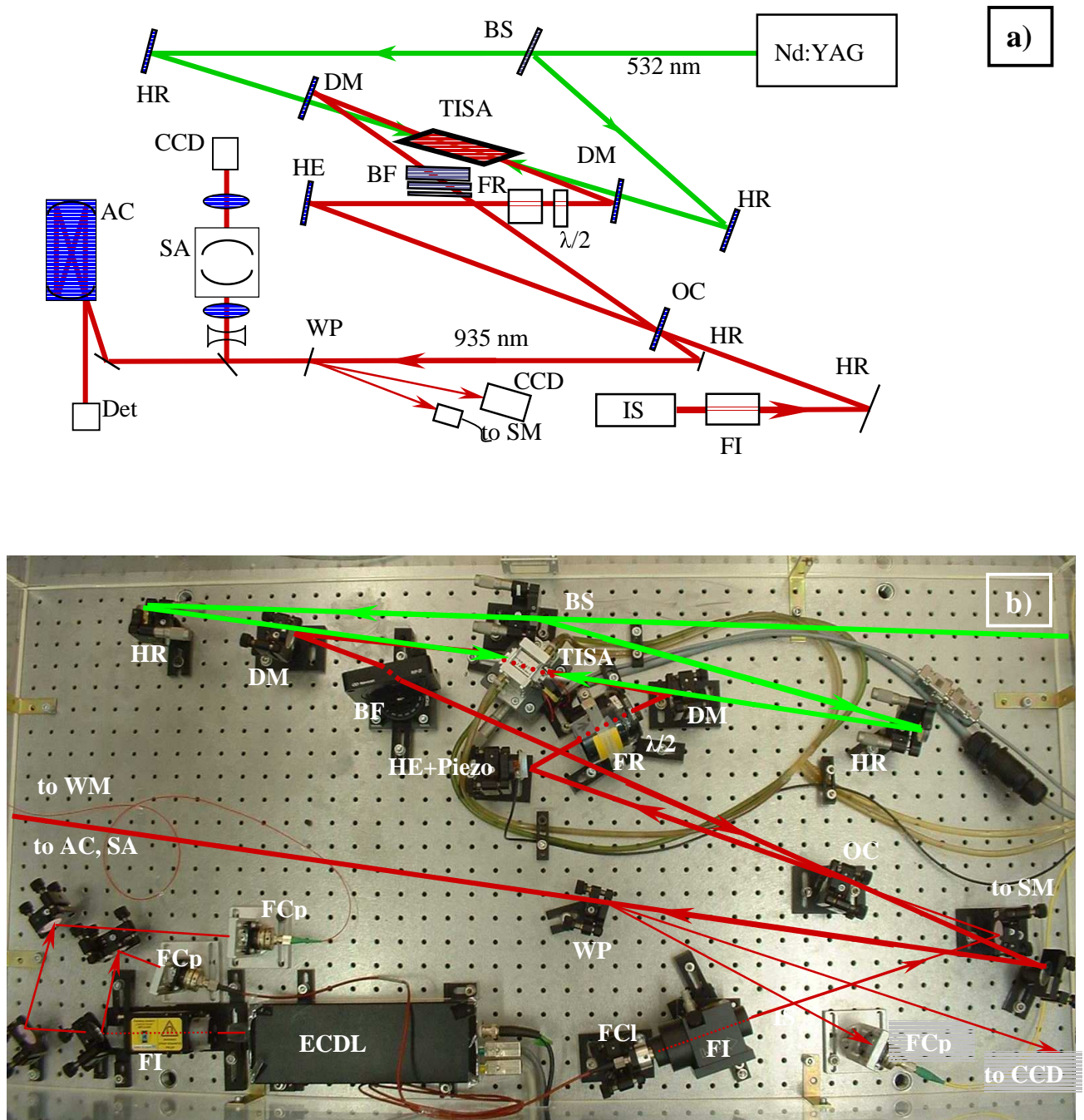
Fig.5.13 Scheme of the TISA set-up for 935 nm (a) and the photo of the experimental layout (b). Here BS – beam splitter, HR – high-reflective mirror, HE – 'hard-edge' mirror, DM – dichroic mirror, L – cylindrical lens, FR – faraday rotator, λ/2 – halfwave plate, BF – birefringent filter, OC – output coupler, IS – injection seeder, FI – faraday isolator, WP – wedge plate, Cam – CCD camera, SA – spectrum analyzer, AC – absorption cell, WM – wavemeter, SM – spectrometer, Det – biased photodetector, ECDL – external-cavity diode laser, FCp – fiber coupler, FCl – fiber collimator.

The DMs provide a high transmission for the pump emission and a high reflection for the emission of the TISA. In the first version of the TISA layout using of these mirrors was omitted to reduce the pump losses (around 4%). The pump and TISA beams propagated coaxially through the rod. Due to a significant refraction index dispersion of the TISA, at the 50 cm remote from the rod the spatial separation of the beams yields 5 mm, allowing to avoid propagation of the pump beam through the aperture of a resonator mirror.

At the final stage of the experiment, the intra-cavity energy density approached the damage threshold of the most sensitive elements, namely the HE and the halfwave plate. They were moved as close as possible to the TISA crystal, in the zone of a larger eigenmode (see Figs. 5.11, 5.13), forcing to use the DMs in the resonator. The achieved safe operation and decrease of the misalignment sensitivity of the cavity, owing to a reduced cavity length from 2.5 m to 1.5 m, was found to be a good trade-off for a smaller pump power.

The fine spectral tuning is obtained with the injection seeder (IS), coupled in the resonator through the OC. To prevent the optical damage of the IS by an occasional contra-propagating ring-cavity emission, a Faraday isolator (FI) was applied. Considering the severe atmospheric absorption at the online wavelengths, the external cavity diode laser (ECDL) was mounted together with the TISA laser, on the breadboard inside the sealed volume. For a higher alignment flexibility of the set-up and to round the IS laser beam, the output of the ECDL was coupled in the resonator with an optical fiber.

For a continuous monitoring of the laser parameters, several devices were implemented apart the CCD-camera for the overlap control. The beam of the TISA emission was directed through a wedge plate (WP) to a power-meter (PM, not shown) Coherent LM100. The first reflex from the WP was sent to a CCD-camera for the beam imaging, the second was coupled in an optical fiber and connected to a spectrometer (SM, SPEX, Model 1302) for a coarse spectrum definition. For some tests, the PM was removed as on the given picture, and the beam was sent partly to a spectrum analyzer (SA, Coherent, Model 240) to observe fringe pattern with the following CCD-camera for a fine mode-structure definition. Another part was coupled in a 30-m multipass absorption cell (AC) for the spectral purity specification.

5.4.2 Output energy and efficiency

The TISA-laser slope efficiency was measured using the pump laser in the configuration Pump-1: 250 Hz repetition rate and 100 mJ pulse energy. The eigenmode radius on the crystal was 0.65 mm (see Fig. 5.11), whereas the radius of the pump beam was kept 0.8 mm to prevent the
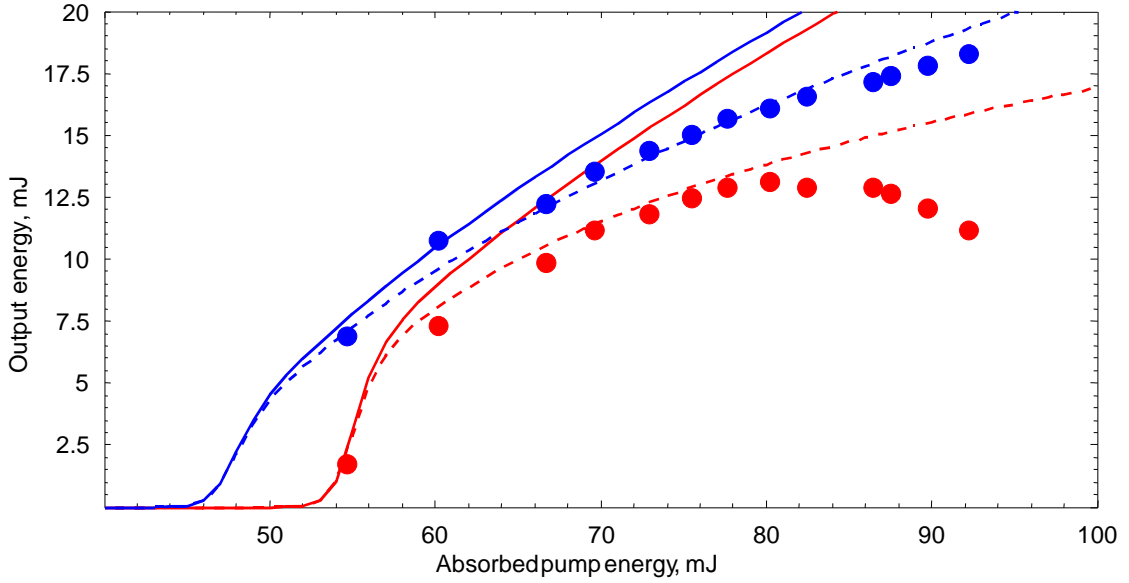
Fig.5.14 Slope efficiency of the TISA laser at 935 nm. The results for the free-running mode marked red, for the seeded – blue. Experimental data marked with dots, numerical solution – with solid lines, numerical solution with intensity-dependant losses – with dashed lines.

optical damage of the TISA. The overlap of the beams was $\approx 77\%$, calculated as the energy fraction of the pump beam inside the eigenmode diameter (at the level $1/e^2$) and normalized to 86.5%. Nevertheless, the pump beam has a near-gaussian cross-section profile, obtaining a gain-guiding effect for the laser pulse evolving in the TISA rod (see Fig.5.15 a).

The optimum reflectivity of the OC was calculated with respect to maximum output energy of the TISA E_{TISA}, using Eq. A.12. For maximum pump energy of 95 mJ and the passive losses in a range 8-20%, the optimum reflectivity is $R \approx 75\%$. The couplers with reflectivities of 60%, 72% and 80% were tested. The output energy of < 12 mJ was achieved using the 80% OC, whereas with the 60% OC ≈ 15 mJ were obtained.

Finally, the 72% OC was preferred. Figure 5.14 shows the measured output pulse energy of the TISA laser, free running (red points) and injection-seeded (blue points) at an offline wavelength, as a function of the absorbed pump energy at 532 nm. The slope efficiency of the laser was $\approx 40\%$ with the lasing threshold at 44 mJ seeded and 52 mJ not seeded. The maximum output pulse energy was 18 mJ with the optical energy conversion efficiency of almost 20% from 532 nm to 935 nm. Although the pump energy in this experiment did not exceed the value of 50 mJ from each side, further reduction of the pump beam size for a better overlap with the TEM_{00} of the resonator was not possible. The limitation was caused by a low LIDT of the optics,

namely the HE-mirror. Further reduction of the eigenmode size and/or increase of the pulse energy led to it immediate damage.

The TISA laser showed a more efficient operation in the seeded mode than in the free-running mode. This effect can not be explained within usual rate-equation model [e.g., Koechner, 1999], based on an analytical solution of balance equations (see App. A). However, a numerical solution of these equations yields discrepancy of the slope efficiency between the seeded and free-running modes of the TISA-laser operation. The numerical solution of the rate equations A.7-A.9 for the amount of passive losses of $B = 0.08$ for the seeded and free-running mode is depicted on the Fig.5.14.

The TISA has a laser transition of $\tau = 3.2$ μs at 300 K [Moulton, 1986], yielding the depopulation of the upper laser level of $\approx 3.5\%$ and corresponding gain drop of $\approx 7\%$ within the first 100 ns after the pump pulse. The seeded operation obtains a shorter pulse build-up time then the free-running mode with a difference of > 200 ns at the lasing threshold (see Fig.5.16). Thus, the seeded pulse enjoys higher gain, which allows for lower threshold and higher efficiency. With increase of the pump power, the build-up time decreases down to 100 ns at maximum and the difference of the output powers in the seeded and not seeded modes is significantly smaller.

Although the presented model yields a good coincidence with the experiment in a sense of the lasing threshold and revealing the discrepancy between the seeded and the free-running modes, the real slope efficiency is smaller than the simulated one. This difference is particularly strong for the not seeded mode, presenting even a negative slope at a high pump power. The lower slope efficiency in the experiment can be explained by a decrease of the energy extraction efficiency from the TISA crystal due to distortion of the cavity mode. The rate of distortion is proportional to the power density of the intra-cavity EM-field.

Figures 5.15 (b) and (c) present the energy distribution in the cross-section of the TISA beam for a circulating intra-cavity energy (average power) of 40 mJ (10 W) and 54 mJ (13.5 W). The beam on the Fig.5.15 (c) has a lower peak intensity because of the stronger filter used in front of the CCD-camera. Regarding these observations the TISA beam has a distortion in the horizontal plane, which becomes stronger at a high power density.

The largest part of the distortion is likely induced by the HE-mirror. Comparing Fig.5.15 (c) with Fig.5.30 (c) for the TISA beam operation at 825 nm, significantly better beam quality of the latter can be mentioned for the same intra-cavity power density. The layouts are similar, and the only principle difference is implementation of the HE-mirror for the experiment at 935 nm.
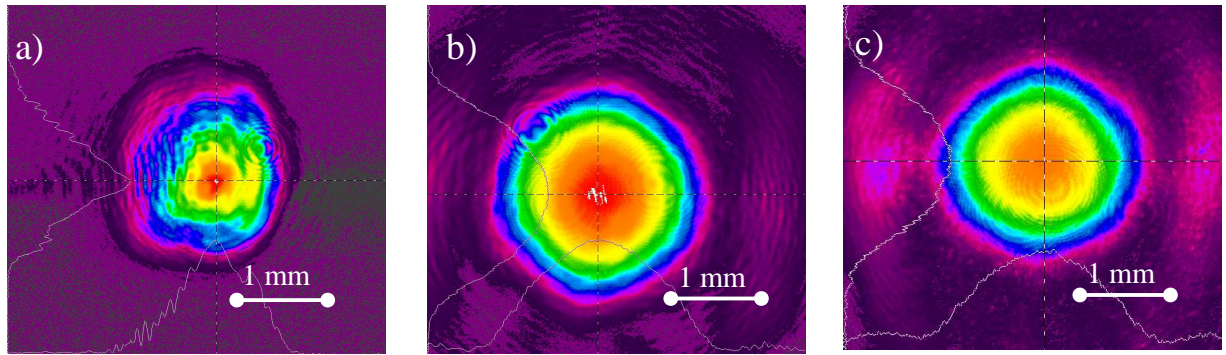
Fig.5.15 Cross-sections of the pump beam (a) and the outcoupled cavity mode of the injection-seeded TISA at 935 nm: 68 mJ pump, 11 mJ output (b) and 75 mJ pump, 15 mJ output (c).

However, the real nature of such a behavior of the HE-mirror is unclear. The thick multilayer dielectric coating of this mirror may bulge at a high intensity of the EM-field, causing its lower damage threshold and, probably, deformation of the wavefront. The beam distortion in the horizontal direction was higher due to the larger radius of the eigenmode on the HE-mirror in this plane, 0.6 mm (considering an incident angle of 17°) vs. 0.5 mm in the vertical plane. The elliptical shape of the pump beam on the Brewster-cut end-face of the TISA rod (two times larger in the horizontal direction) contributes the distortion of the eigenmode as well. Although there were no special measurements performed to study the operation of the HE-mirror at high energy densities, the summary of the practical experience allows to confirm its influence on the distortion of the eigenmode.

These dissipative losses can be considered in the pulse evolution model as the intensity-dependent ones. The numerical solution gives a good fit for the seeded mode with 4% of these losses at the maximum pump power starting from 0 at the laser threshold (see Fig.5.14, blue dashed curve). Including the losses in the model of the not-seeded lasing gives a better fit to the experimental results from the lasing threshold up to 75 mJ of the pump energy, though it does not explain the negative slope at the higher energy levels (see Fig.5.14, red dashed curve).

The energy decay in the free-running mode is due to the observed contra-propagating wave in the cavity. The Faraday rotator used for this experiment, rotates polarization plane for only 15°, yielding in total a 30°-rotation for the "wrong" direction and, hence, only 19% round-trip losses more on all intra-cavity Brewster-angle surfaces. At a high pump power the gain exceeds the round-trip losses for the contra-propagating wave. The appearing lasing in the contra-direction depletes the total gain and decreases of the output in the main direction. However, when the

cavity is seeded, the wave in the seeding direction starts to evolve earlier and extracts all the gain before the contra-propagating emission can exceed the lasing threshold.

The laser operation in the seeded mode on the maximum pump power was possible in the current set-up for only a few minutes until damage of the coating of the HE-mirror. The peak energy density of the eigenmode on this mirror was 15.5 J/cm^2 (at 935 nm, rate 250 Hz, pulse width 40 ns). Taking into account the distortion of the beam, the value of the laser induced damage threshold for the HE-mirror may be estimated at $\approx$ 10 J/cm^2.

Measurements of the beam quality were performed for the output pulse energy of 12 mJ to avoid the optical damage, yielding $M^2 = 1.75$. Due to the additional beam distortion on the higher intensities, the value of $M^2 \approx 2$ was estimated for the maximum pump power.

5.4.3 Build-up time of pulses

To define the temporal characteristics of the transmitter emission, pulses were monitored with a high-speed photo diode and their build-up times, measured peak-to-peak, were recorded. Figure 5.16 shows the build-up time of the TISA laser for different pump energies in seeded (blue) and free-running (red) modes. The experiment conditions were the same as for the Fig.5.14.

The analytical solution of the rate equations A.7-A.9 (see Eq.A.14) and their numerical solution present the similar results. Further detail of the model with the intensity-dependent losses (see Fig.5.16 dashed curves) leads to a negligible change.

The fit between simulation results and the experiment for the free-running mode is within a measurement uncertainty, whereas in the seeded mode a $\approx$40% underestimation of the build-up time is observed. The source of this bias is still not known and further improvement of the pulse-evolution mode is required.

There is an obvious build-up time reduction by seeding. Nevertheless, the measured pulse width does not depend on the presence of the seeding emission, confirming the model (see Eq. A.15). At the maximum pump power the width of $\approx$ 40 ns (FWHM) was measured.

5.4.4 Spectral properties – single mode lasing and emission bandwidth, seeding efficiency

To fulfill the strict parameters of the water-vapor DIAL transmitter, the TISA laser must operate at one or two longitudinal modes. Applying only the passive spectral-selection components, a TISA bandwidth of approx. 1 nm can be obtained. Figure 5.17 depicts the IS and the TISA emission spectrums, coupled via a multimode fiber in a 2-graiting spectrometer (SPEX Model 1302) and recorded with a line CCD-camera (Thorlabs LC-1).
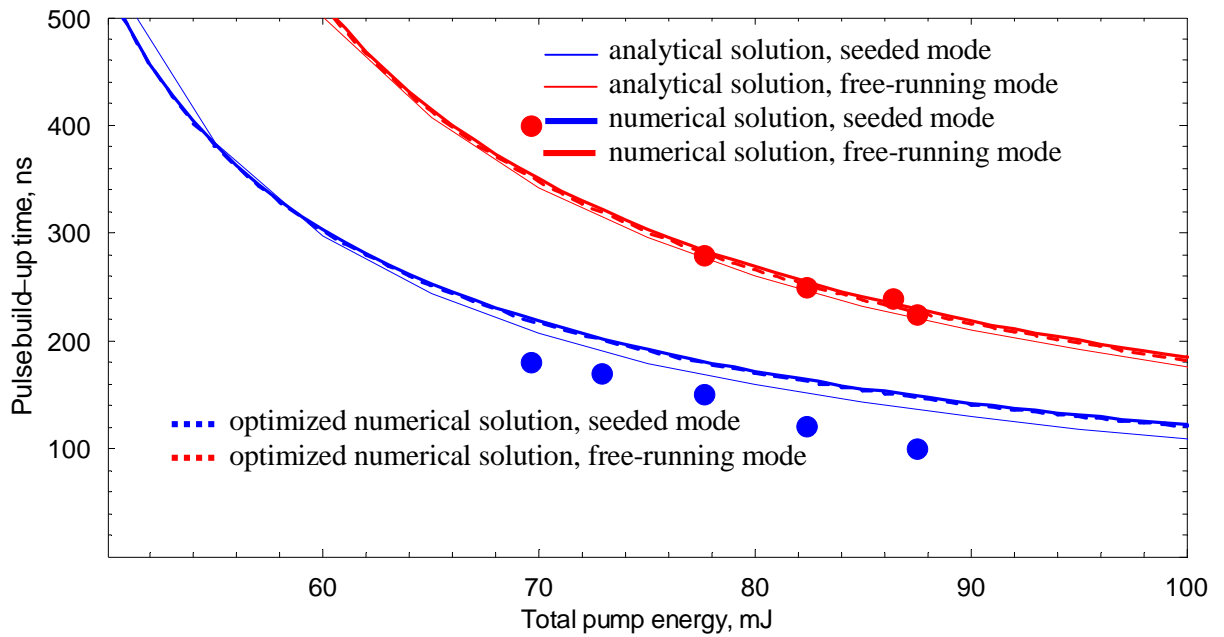
Fig.5.16 Pulse build-up time of the TISA laser at 935 nm vs. absorbed pump energy, measured for seeded (blue dots) and not seeded (red dots) operation. Result of the modeling is drawn with thin, thick and dashed curve for the analytical, numerical, optimized numerical solution, respectively. Conditions of the experiment and assumption of the calculations were the same as for the slope efficiency (see Fig. 5.14).
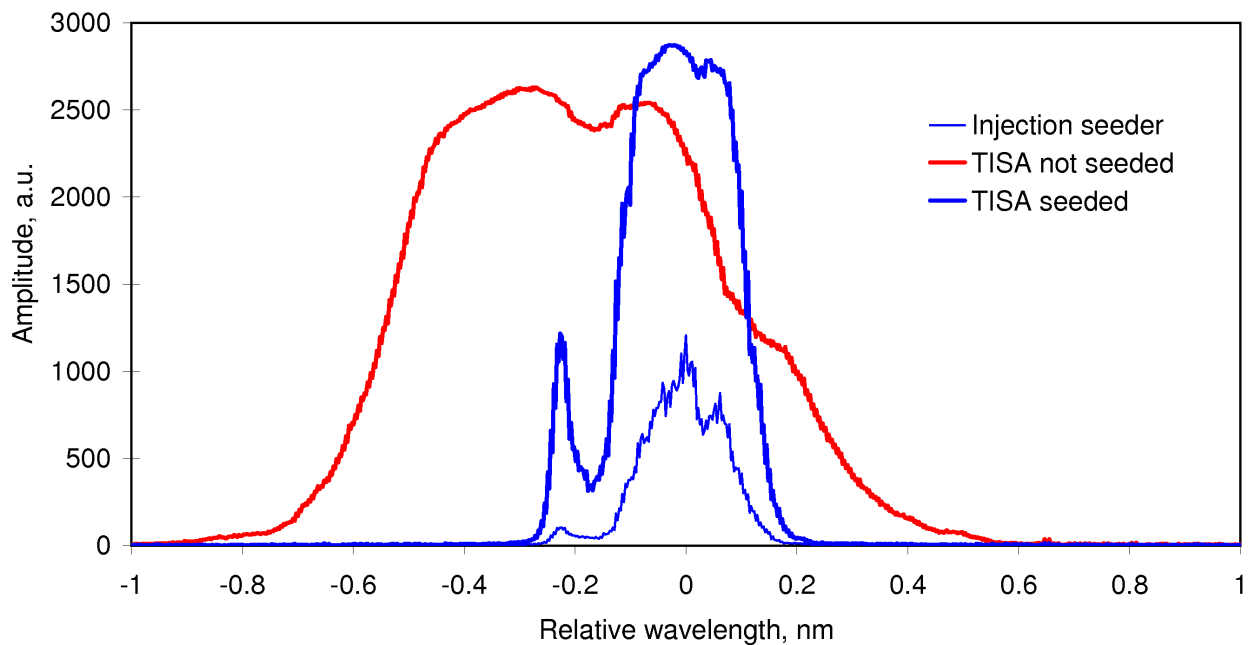
Fig.5.17 Coarse spectrum of the IS and the TISA laser, seeded and not seeded, obtained with the grating spectrometer SPEX 1302 (resolution ≈ 0.2 nm @ 930 nm). The subpeaks are due to misalignment of the coupled laser beam.

The free-running laser operated with a bandwidth of ≈ 0.8 nm (red curve). Using the IS (blue thin curve) allowed to decrease the bandwidth of the TISA laser to the value comparable with the bandwidth of IS itself (blue thick curve). The bandwidths of the seeder and the seeded laser were measured to be ≈ 0.2 nm, limited by the resolution of the spectrometer. The sub-peaks on the spectrums of the IS and the seeded TISA laser are caused by misalignment of the coupled beam.

For the fine specification of the longitudinal-mode structure and the bandwidth of the TISA the spectrum analyzer (Coherent Model 240) was applied. For its specification see Subsection 4.2.

To work with the pulse signal, the SA was set in a 'fringe' mode, when the photodetector and the lens are removed, ramp generator is switched off and the SA works as an FPI. The incoming laser beam from the transmitter is expanded and collimated to fill the whole aperture of the FPI. The generated energy pattern from between the mirrors is imaged with a lens to a CCD-camera. Figure 5.18 (a) shows such a pattern of the partially seeded TISA, when the frequency of the IS does not match the cavity length and two neighbor modes are lasing simultaneously (two sets of rings), while part of the emission stays unseeded (non structured spot in the center of the shot). When the IS frequency is close to one of the resonator longitudinal modes, lasing of the transmitter is performed only on this frequency (see Fig. 5.18 b). Some multiple sub-patterns on the pictures were caused by diffraction on the 5 mm aperture of the mirrors of the FPI and aberrations of the imaging lens.

The width of the fringes can be used to define the bandwidth of the TISA. Regarding [Hercher, 1968], the frequency separation of two points within the same FSR is correlated with radii of their fringes as

$$\Delta v \equiv v_2 - v_1 = \frac{<v>}{4r^4}\left(\frac{\rho_2^4 - \rho_1^4}{M^4} + 4r\varepsilon\frac{\rho_2^2 - \rho_1^2}{M^2}\right),$$
(5.10)

where $<v>$ – mean optical frequency of the signal, r – radius of curvature of the interferometer mirrors, ρ – radii of the fringes, M – magnification of the imaging optics and ε – departure of the FPI mirrors from the confocal separation r. For the given values of ε and r, the magnification can be derived from the distance between two fringes, separated by one FSR.

Figure 5.19 displays the intensity distribution in the fringe pattern of the emission of the injection-locked TISA laser along the horizontal main axis of the fringes (it corresponds the horizontal dashed line on the Fig. 5.18, b).

For the confocal FPI with the mirror separation of r = 10 mm and the departure of ε = 15 μm, an
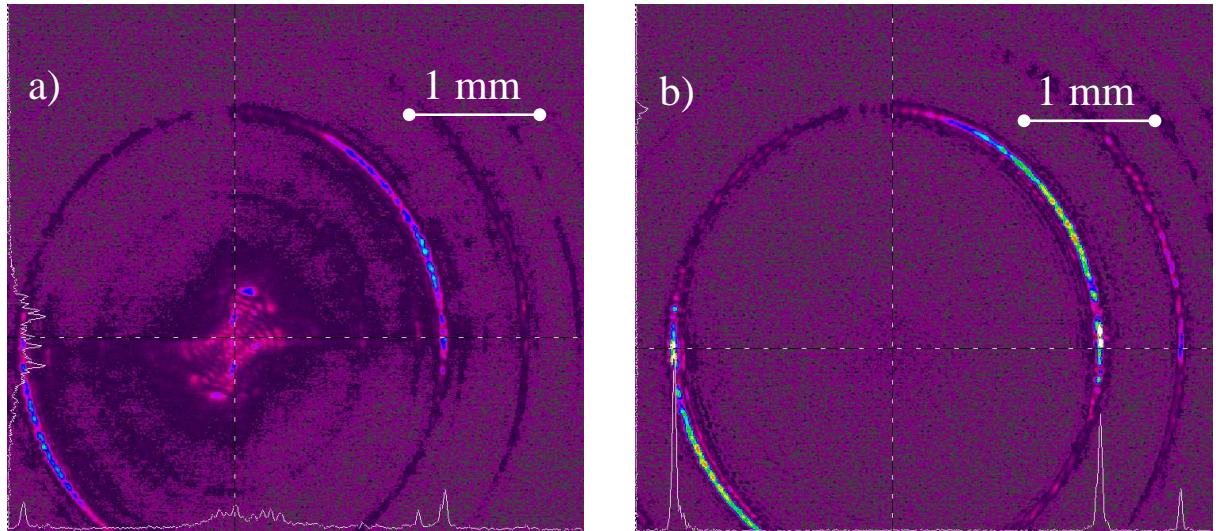
Fig.5.18 Fringe pattern formed in the confocal FPI and recorded with a CCD-camera for a) partially seeded TISA and b) injection-locked TISA at 935 nm.
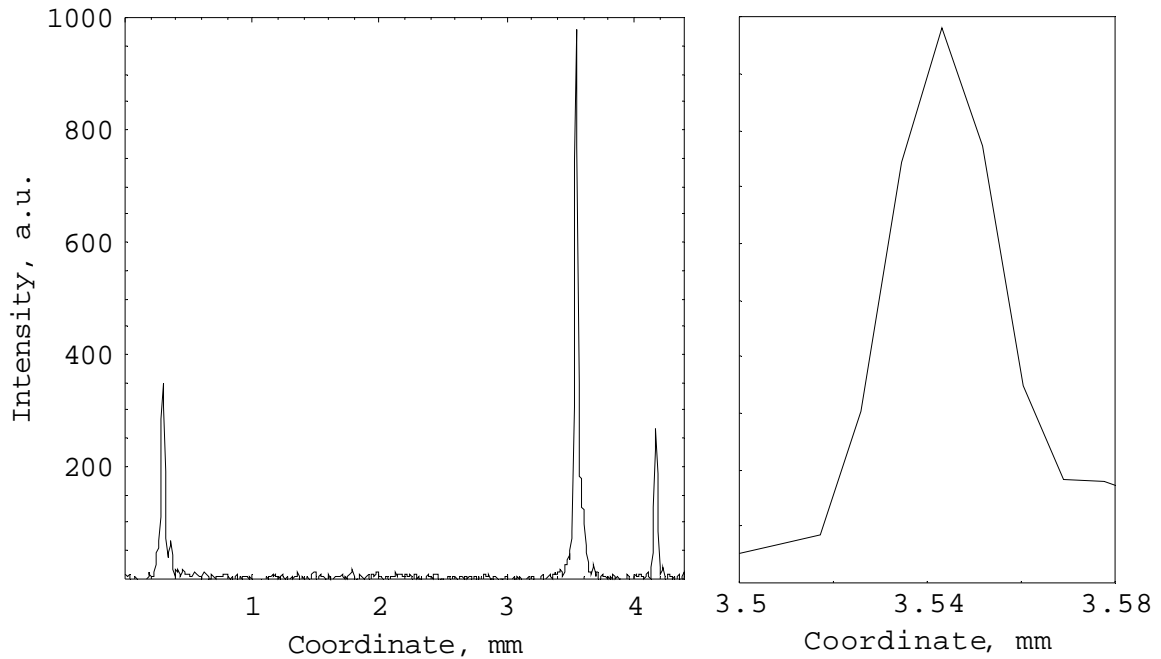
Fig.5.19 Intensity distribution in the fringe pattern of the injection-locked TISA along the horizontal main axis of the fringes (left); corresponds the horizontal dashed line on the Fig. 5.18 (b). Scaled cross-section of the first-order ring is imaged on the right, cell width of the CCD-array is 8.6 μm.

observed fringe width of $\Delta\rho \approx 21$ μm of the first fringe with a radius of $\rho \approx 1.62$ mm results in a bandwidth of $\Delta v \approx 173$ MHz. Considering the resolution limit of the FPI of 35 MHz (for the finesse of 200), imperfection of the imaging system – defocusing and aberrations of the lens – and limited resolution of the CCD-array, the real bandwidth of the TISA emission was < 160 MHz, fulfilling the requirements for the airborne operation (see Table 2.1).

The same SA in the 'fringe'-mode can be used for a coarse estimation of the seeding efficiency. As it is well known, the seeding efficiency depends on the ratio P_{IS}/P_{TISA} [Barnes and Barnes, 1993]: for the same output power of the TISA laser, a higher master-laser power yields more efficient seeding. When the IS power is very weak, the successful seeding can be performed only when frequency of the seeded beam fits one of the resonator longitudinal modes. Increasing the power of the IS, the seeded operation becomes possible also when the IS is slightly away from the cavity resonance. When intensity of the seeding emission exceeds a certain threshold, an efficient seeding is obtained regardless the cavity length. The seeding is efficient if spectral purity of the slave laser is $SP > 99.7\%$.

To perform a measurement of the seeding efficiency, the CCD-camera in the previous set-up was replaced with an iris aperture, blocking all the fringes and, therefore, all seeded part of the laser emission. The unseeded part in the center of the pattern was focused on a sensor of a bias detector (Thorlabs 210) behind the aperture. During the experiment the length of the TISA cavity was kept constant and IS frequency was scanned: a ramp voltage of the 'triangle' shape was applied to the piezo actuator of the grating in ECDL. Every time when the cavity length approached the whole number of wavelengths of the IS, the seeding efficiency increased and the non-seeded fraction of the output emission became negligible. Figure 5.20 depicts the measurements for the 16 mW seeding power and the TISA laser output of 1.8 W (left) and 2.8 W (right). The TISA was successfully seeded within the region ±0.23FSR and ±0.17FSR around the slave cavity resonance, respectively.

The value of the FSR of the resonator was calculated from the plot as the distance between two neighbor minimums in the detected signal. The signal in the minimums differed from zero due to a background noise on the detector. Strong fluctuations of the measured values outside the locking regions were caused by a frequency beating between the laser repetition rate and the acquisition rate of the oscilloscope. Nevertheless, this method is applicable to define the width of the locking regions as long as they are detectable.

For a more accurate estimation of the seeding efficiency a multipass absorption cell (AC) filled with water vapor at a low pressure can be deployed. The measurement principle is similar; the FPI is substituted with the AC and the IS is tuned to a high-absorption water-vapor line. A sensitive detector is mounted behind the AC. When the emission of the TISA cavity is locked to the frequency of the IS, the transmission of the AC is negligible. Outside the locking zone the unseeded part of the TISA emission experiences smaller attenuation and contributes the detector
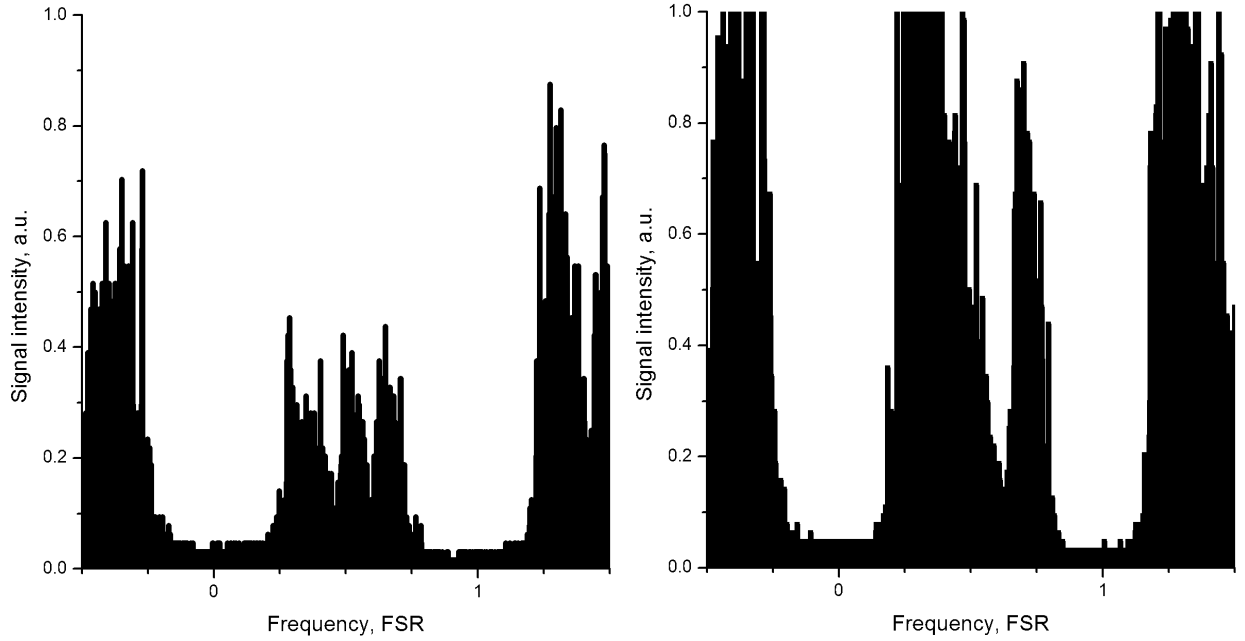
Fig.5.20 Intensity of the unseeded TISA emission while scanning the IS frequency over the range of several FSRs of the slave cavity. Measurements made with IS power of 16 mW and TISA output of 1.8 W (left) and 2.8 W (right). The multiple subpeaks are due to a frequency beating of the acquisition system of the oscilloscope and the pump laser repetition rate.

irradiation. This measurement is less sensitive for the background noise and temperature drift of the FPI. However, the smallest detectable offset of the unseeded fraction is limited by the absorption-line width (≈ 0.5 GHz).

5.4.5 Spectral properties – spectral purity

The spectral purity of the TISA laser can be specified, using a multipass absorption cell filled with water vapor at a low pressure. For this purpose, the 30-m multipass absorption-cell Toptica, filled only with water vapor at the pressure of 16 hPa and temperature 15°C (saturation pressure for this temperature is 22 hPa) was implemented. The simulation shows that for this conditions the water-vapor absorption at $10687.383 \text{ cm}^{-1}$ on a 30-m track is $> 99.99\%$. The offline measurement was performed at $10686.870 \text{ cm}^{-1}$ with transmission on a 30-m track $> 99\%$.

To estimate the spectral purity value, the intensities of the online and the offline signals transmitted through the AC must be compared: $SP = 1 - P_{on}/P_{off}$ (here absorption losses offline are neglected). For the measurement a fast silicon photodetector Thorlabs 210 was used. To decrease the optical noise occurred during scattering of the beam on the input and output windows and on the mirrors of the AC, the detector was mounted 1 m away from the escape window of the AC with a 2-mm aperture in front. The size of the aperture was set to obtain the
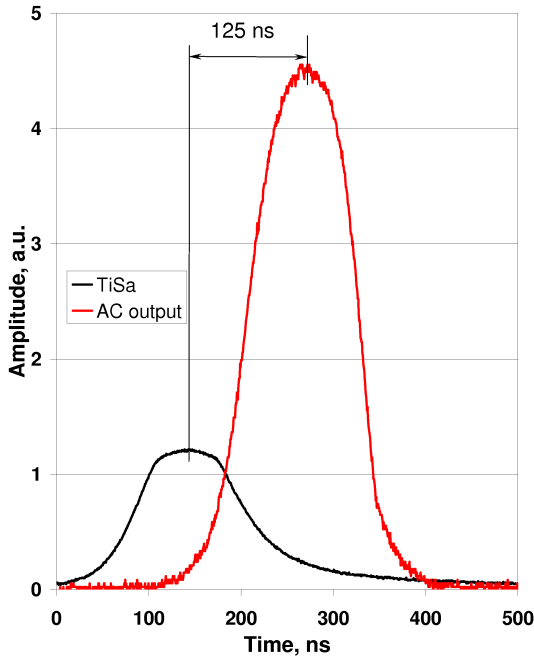
Fig.5.21 Temporal shape of the TISA pulses before and beyond the AC, offline frequency. The signal intensity ratio is accidental.
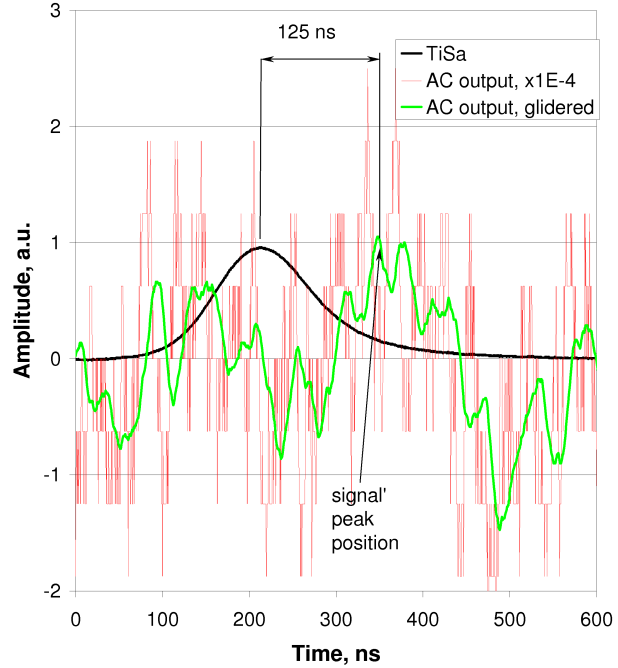
Fig.5.22 Temporal shape of the TISA pulses before and beyond the AC, online frequency. The TISA signal is glidered to increase the SNR.

maximum non-saturated detector response on the offline emission.

Figure 5.21 depicts the signal recorded with this sensor while the laser was operated at the offline wavelength (red curve). The TISA pulse behind the OC was observed with another detector and is shown for the a reference (black curve). The amplitude ratio of these signals is accidental. Due to an optical path difference of > 30 m between the detectors, the signal after the AC has a 125 ns delay.

Figure 5.22 shows the same signals for the TISA laser operating at the online wavelength. The signal after AC is at the detectivity threshold. To extract the pulse profile from the signal, a glidering average of the data was performed (green curve). Comparing the signal intensities (4.4 V online and < 0.1 mV offline) and taking into account some output power drop online (2.4 W 'online' vs. 2.7 W 'offline'), the spectral purity is $SP > 99.99\%$.

5.4.6 Summary of the 935 nm experiment

In the following table the measured transmitter parameters are summarized. In this experiment no active stabilization of the resonator cavity was applied: the cavity length was tuned manually using a HR-mirror glued on the piezo actuator. Hence, the frequency stability was not included into the summary. The PDH feed-back loop was applied in the 820-nm experiment.

Table 5.2 Summary of the requirements for the reference water-vapor DIAL and parameters of the experimental device.

Parameter	Specification	Experiment
Wavelength, nm	935	935
Average power, W	10	4.5
Pulse energy, mJ	> 40-10	18
Repetition rate, Hz	250-1000	250
Pulse duration, ns (FWHM)	< 200	40
Pulse linewidth, MHz	< 160	< 160
Tunability, GHz	±10	> ±10
Beam quality, M^2	< 2	≈ 2
Spectral purity, %	> 99.7	> 99.99

Although the final goal of 10 W output power was not achieved, the power of 4.5 W of the transmitter is the highest average power obtained with a single-crystal TISA laser at 935 nm, emitting single-mode with a near-Gaussian beam profile. To increase the output power the single-rod transmitter can be expanded in a MOPA configuration (see Subsection 7.2.2 for a discussion).

The applicability of the HE-mirror for spectrum narrowing was tested in this work. The mirror performed perfect high-band pass, so that the spectrum of the laser emission was restricted for the vicinity of 935 nm. However, it was found that flatness of the multi-layer dielectric coating of the mirror experience an elastic deformation at a high power density. Although the damage threshold of this mirror of ≈ 10 J/cm^2 is comparable with characteristics of the usual HR-mirrors with ≈ 14 J/cm^2, it was found that the heat-induced deformation of the coating may be a reason for spatial distortions of the reflected beam. For a damage-free operation with a low level of the heat-induced distortions at a high intra-cavity field intensity, another spectrum filter, e.g. set of Brewster prisms, has to be preferred.

5.5 Ti:sapphire transmitter for ground-based measurements

For optimum operation of the TISA transmitter as a part of a ground-based water-vapor DIAL, the lasing wavelength has to be tuned to 820 nm. This spectral region was preferred to 935 nm, because the water-vapor absorption lines in the vicinity of 935 nm are too strong for ground-based measurements (see Subsection 2.2 for the requirements). Furthermore, the doubled TISA gain and an order of magnitude weaker water-vapor absorption coefficient at 820 nm allow for lasing with considerably higher efficiency and better stability even with non-sealed cavity.

To optimize the cavity configuration, results of the thermal and resonator design models were implemented (see Subsections 5.2-5.3). The components of the laser transmitter have been optimized regarding the same procedure as it was shown in Subsection 5.4. Two series of experiments were performed for both pump laser configurations Pump-1 and Pump-2 with a maximum pump power of 25 W and 45 W, respectively.

5.5.1 Ti:sapphire set-up

In the vicinity of 820 nm there are water-vapor absorption lines with large and small absorption cross-section, useful for vertical and horizontal water-vapor profiling of the atmosphere under all standard atmospheric conditions (see Table 5.3). For the simulation of the absorption spectrum information from the ESA database [ESA, 2000] was deployed: here the water-vapor data for the wavelength region around 820 nm is derived more accurate than in [HITRAN, 2005]. Figure 5.23 depicts spectral distribution of the water-vapor absorption cross-section in the vicinity of 820 nm, calculated for US Standard Atmosphere.

Table 5.3 Suitable water-vapor absorption lines in the region of 815-820 nm (after [ESA, 2000]). Here S – intensity of the absorption line; γ_{air} – air broadened width of the line (HWFM); E'' – lower state energy.

Wavenumber vacuum, cm^{-1}	Wavelength vacuum, nm	S, cm^{-1}/cm^{-2}	γ_{air}, cm^{-1}/bar	E'', cm^{-1}	Notes
12190.7435	820.294513	1.10E-23	0.1023	37	G5
12193.2465	820.126125	4.63E-24	0.0997	225	G4
12195.1906	819.995384	4.16E-23	0.1012	24	
12202.0284	819.535877	3.29E-23	0.1027	42	G3
12207.7517	819.151658	4.86E-23	0.0977	79	
12212.0701	818.861988	1.77E-23	0.0979	70	
12218.8296	818.408988	2.26E-23	0.0936	135	
12223.0047	818.129441	1.65E-23	0.0913	142	G2
12223.8401	818.073528	7.54E-24	0.0951	136	
12224.6670	818.018192	1.43E-23	0.101	95	
12226.1012	817.922233	5.25E-23	0.0933	137	G1
12228.7400	817.745737				Offline
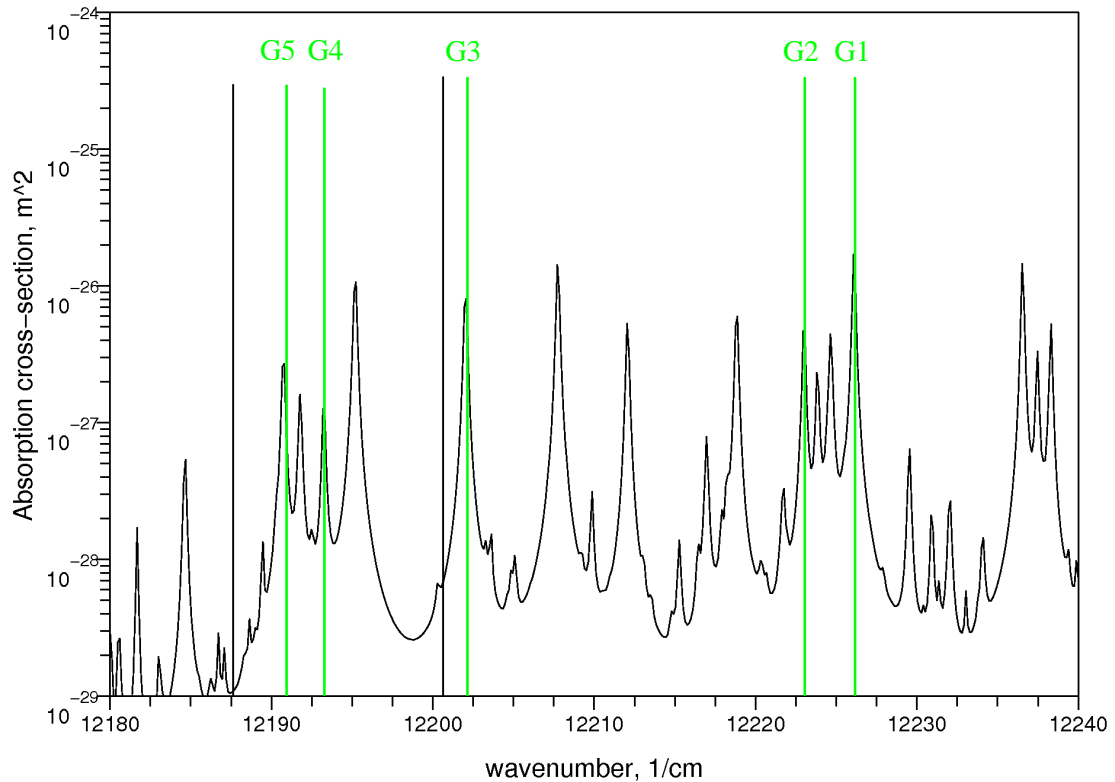
Fig.5.23 Spectrum of the water-vapor absorption cross-section for standard atmosphere conditions around 820 nm. Locations of the strong absorption lines and the offline zones are marked with green and black lines, respectively.

For the defined spectral region the anti-reflective (AR) and high-reflective (HR) coatings of the intra-cavity elements were optimized correspondingly. The final goal of the optimization is to provide a value of the small-signal round-trip amplification in the cavity $\gg 1$ at the wavelength of interest and < 1 at the other wavelengths. After [Moulton, 1986], the gain spectrum of the TISA is around 300 nm broad with maximum at 800 nm (see Fig.5.24, black). An HR laser mirror with a dielectric coating centered at 820 nm and designed for 0° incident angle obtains a reflectivity $> 99\%$ within ± 50 nm from maximum. Using HR-mirrors optimized for 45° incident angle allows to restrict the laser emission to > 790 nm, but provides no advantage in the region 800-820 nm. For a better suppression of the shorter wavelengths, the OC with reflectivity of 52% at 820 and 40% at 790 was implemented (see Fig.5.24, green).

Further spectral narrowing was performed using a birefringent filter (BF) (see Subsection 4.1.1). For this experiment a BF with plates thicknesses of .5, 1, 2 and 8 mm was applied (see Fig.4.1). The plate sequence 2 mm, 1 mm, 0.5 mm, 8 mm was chosen, the angle between optical axis of the plates and the polarization of the intra-cavity field was tuned to 28.8° (see Fig.5.24, blue).
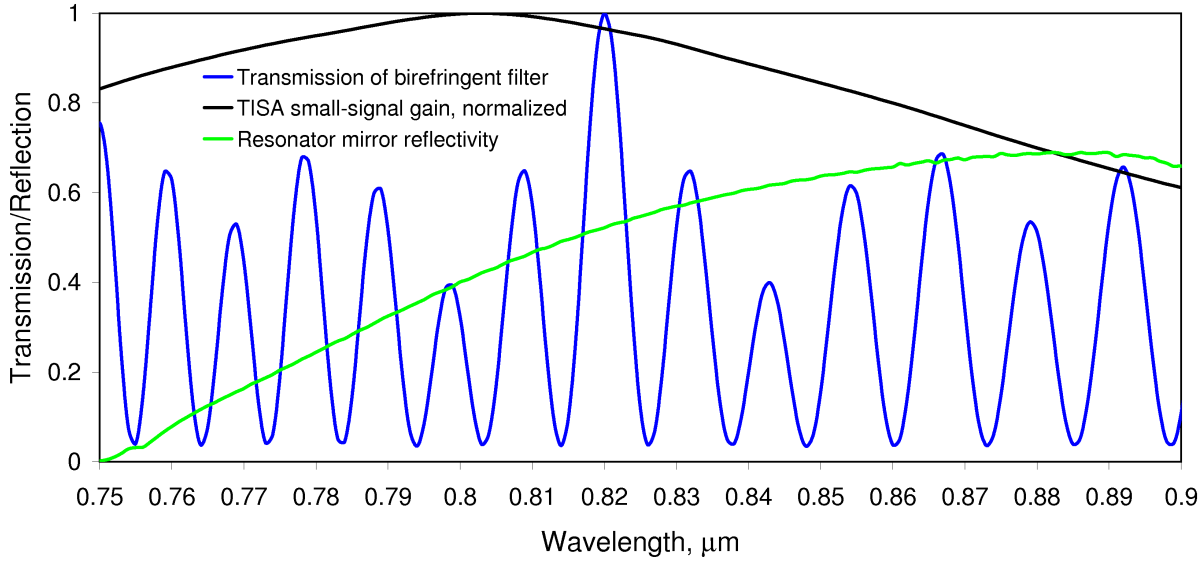
Fig.5.24 Calculated spectral properties of the intra-cavity elements of the TISA set-up at 820 nm: TISA small-signal gain, normalized (black); calculated transmission spectrum of the 4-plate BF, optimized for 820 nm (blue); round-trip reflectivity of the three HR and OC of the z-shape ring cavity (green).
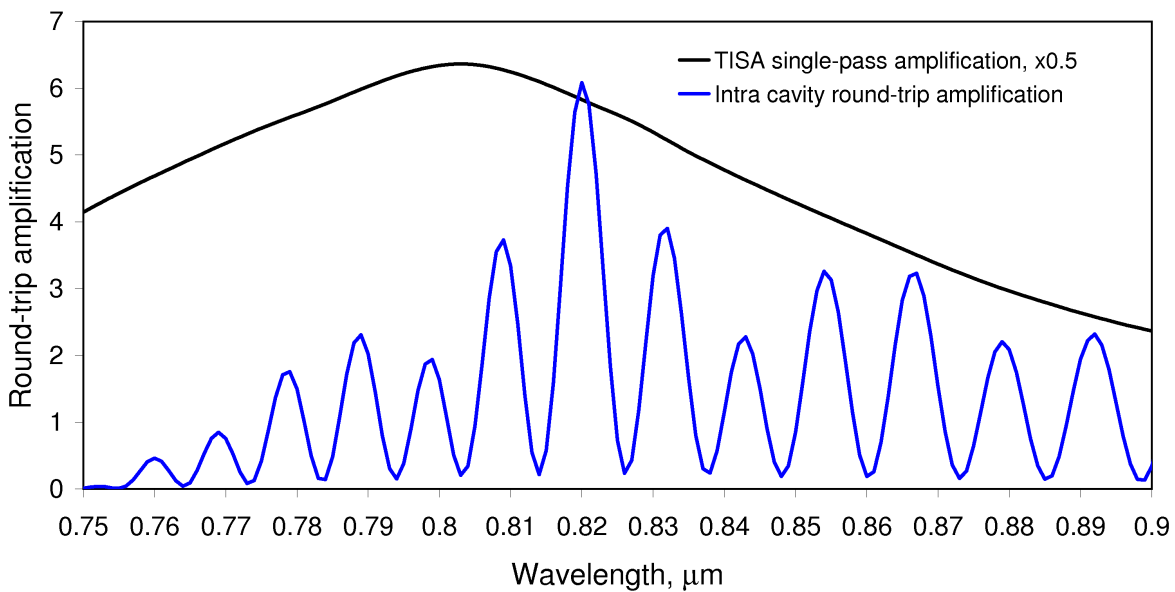
Fig.5.25 Calculated spectrum of the small-signal intra-cavity round-trip amplification in the TISA laser at 820 nm. TISA small-signal single-pass gain (black) scaled 0.5, cavity round-trip amplification (blue).

Considering the spectral properties of the resonator components, the estimated spectral distribution of the small-signal round-trip amplification in the laser cavity was calculated (see Fig.5.25, blue). Its peak value of $\approx$ 13 @ 800 nm corresponds the maximum pump pulse energy of 90 mJ and 140 mJ with the pump beam radius of 0.8 mm and 1.1 mm for the pump laser in the configuration Pump-1 and Pump-2, respectively(see Eq.A.7). The scaling of the pump beam size

in the configuration Pump-2 was performed to preserve for a higher pulse energy the same peak energy density on the end-face of the TISA crystal, avoiding it optical damage.

With the BF and the OC with reflectivity of $R = 52\%$, the laser operates at 820 nm with a round-trip amplification of ≈ 6. However, there is still too much gain in the neighbor peaks. It was assumed that no additional passive spectral filters is required. First, for the calculation no losses on the FR, the halfwave plate, and no depolarization losses were considered. Hence, the real amplification is less than modeled, and the emission at undesired wavelengths does not exceed the lasing threshold.

Furthermore, for the fine selection of the wavelength the injection seeder was used. For the initial specification, the ECDL Toptica DL100 tuned to 825 nm with an output power of 15 mW cw was deployed. Operation at 825 nm instead of 820 nm was caused by limited tunability of the laser diode, which had a maximum emission at 830 nm in a free-running mode. For the final specifications and in-field measurements the double-ECDL IS build at the DLR Oberpfaffenhofen was implemented (see Subsection 4.2). Due to a high average power of the TISA laser and the strict spectral purity requirements for the transmitter, an active cavity length stabilization was implemented. A feed-back loop regarding modified Pound-Drewer-Hall technique was built (see Subsection 4.1.3).

Taking into account the losses of the pump beam between the pump laser and the TISA crystal, maximum 140 mJ of the pump emission was absorbed in the rod in the experiment with the pump laser in the configuration Pump-2. This corresponds to the thermal lens focal length of 440/640 mm in tangential/sagittal plane, respectively (see Fig.5.6).

The calculated intra-cavity mode shape of the TISA laser in the experiment with the Pump-1 was the same as in the 935 nm experiment (see Fig. 5.11). To optimize the cavity for the higher pump power of the Pump-2, the resonator length was increased to 1500 mm and a thin cylindrical lens with a focal length of $f = -980$ mm in tangential plane was applied. The lens was mounted 70 mm away from the surface of the TISA rod. Using Eqs. 5.6-5.8, the TEM_{00}-mode radius along the resonator can be calculated, separately in the tangential and sagittal plane (see Fig.5.26). The intra-cavity beam propagation without the lens is depicted on the picture as well (dashed lines). The lens provides round shape of the eigenmode on the crystal and increases the beam waist size in the tangential plane, preventing damage of the resonator optics. Using of the lens does not affect the beam propagation in the sagittal plane.
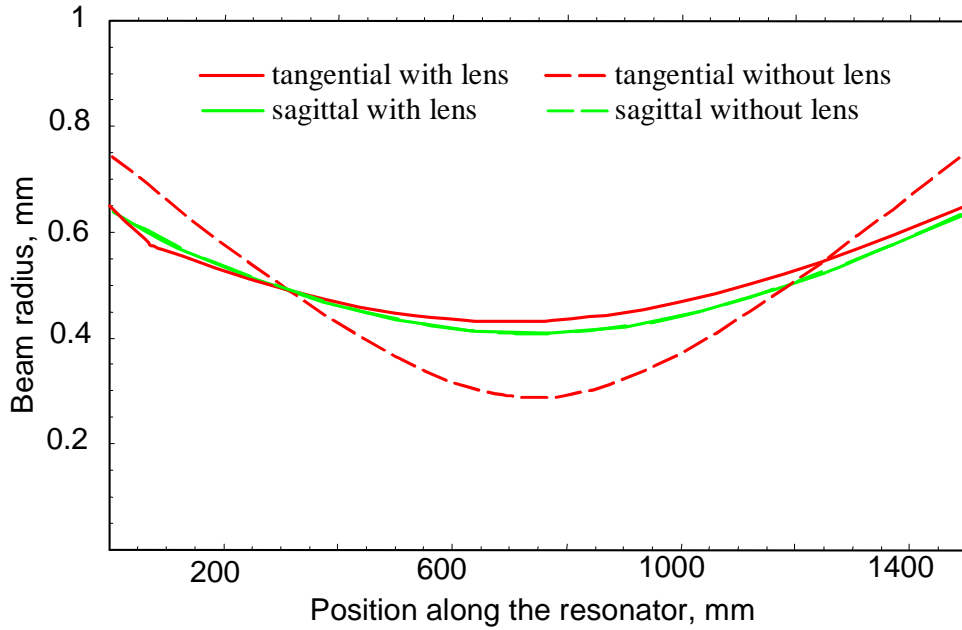
Fig.5.26 Calculated radius of the eigenmode along the resonator of the TISA set-up at 820 nm in the tangential (red) and sagittal (green) plane. Beam propagation along the cavity with the lens is marked with a solid line, without the lens with dashed line.
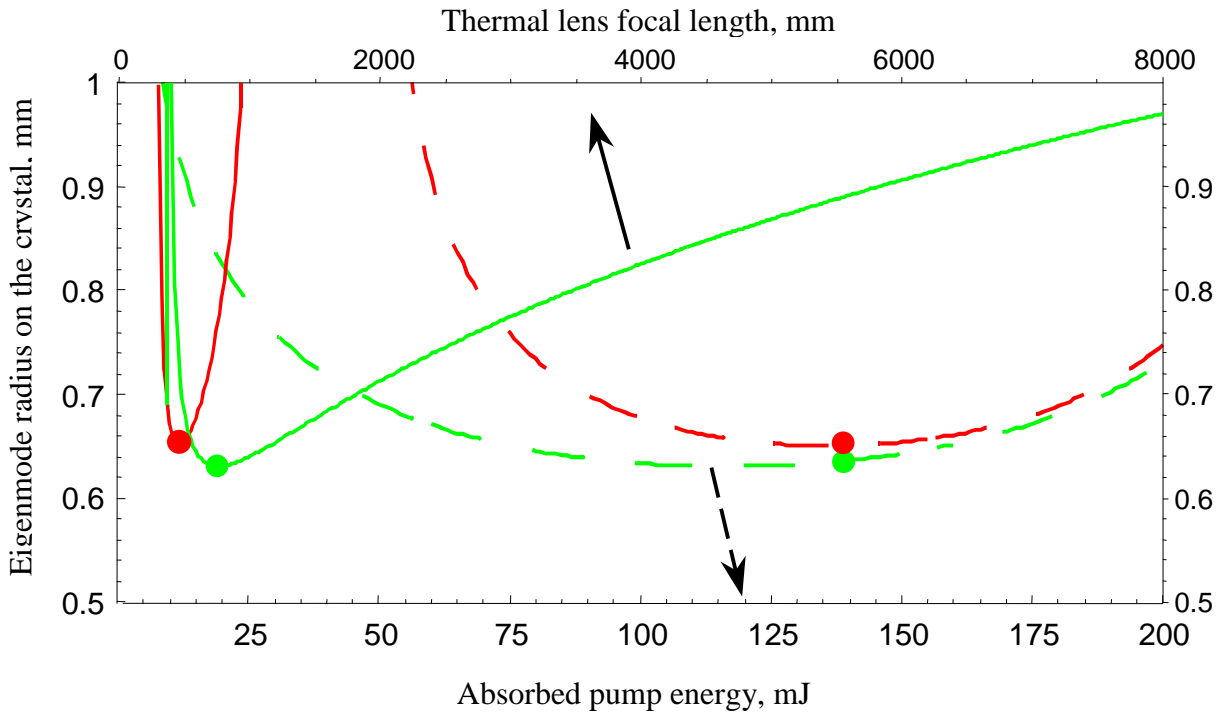
Fig.5.27 Calculated radius of the TEM_{00} in the crystal rod with respect to the thermal lens focal length (solid curves) and the absorbed pump energy (dashed curves) in tangential (red) and sagittal (green) planes. The radii values corresponding the maximum pump power are marked with disks.

Figure 5.27 presents the stability zone of the cavity: the eigenmode size on the TISA rod with respect to the thermal lens focal length (solid curves) and absorbed pump energy (dashed curves). Using of the cylindrical lens affects only the tangential plane of the stability range, whereas in the sagittal plane size of the stability zone stays unchanged.

Figure 5.28 shows a scheme and an experimental layout of the TISA laser optimized for operation at 820 nm. A beam from the pump laser propagates to a 50% beam splitter through the lens combination, fitting the pump energy distribution in the crystal rod to one of the eigenmode of the resonator. Bending on HR-mirrors, the pump beam excites the TISA crystal from both sides. Both path lengths from the BS to the corresponding crystal surface are kept equal to obtain the symmetrical beam propagation. The dispersion of the refraction index in TISA between 532 nm and 820 nm is significantly lower than one between 532 nm and 935 nm. This makes the spatial separation of the pump beam and the eigenmode on the resonator mirrors rather challenging. The dichroic resonator mirrors (DM) with a high reflectivity at 820 nm and a high transmission (around 96%) at 532 nm were applied.

The ring cavity was assembled of 3 HR-mirrors and an output coupler. A low-weight HR-mirror was glued on a high-voltage piezo actuator (HVPA), allowing for a fast-respond cavity stabilization. To provide an unidirectional cavity propagation, a combination of a 45° Faraday rotator (FR) and a halfwave plate ($\lambda/2$) was implemented. The birefringent filter for a coarse spectral selection was used. The fine spectral tuning was provided by the injection seeder (IS), coupled with an optical single-mode fiber in the resonator through the OC. A beam shaper comprised by a lens of the fiber collimator and a negative lens L2 fits the fiber output to the eigenmode of the cavity. A Faraday isolator (FI) was applied for the protection of the fiber from an occasional counter-propagating pulse from the TISA laser.

For the compensation of the short thermal lens in the tangential plane, the cylindrical lens was mounted as close as possible to the TISA crystal. The FR and the halfwave plate were put close to the lens where the size of the eigenmode is large and the energy density is low to avoid their optical damage.

The equipment of the stabilization circuit was mounted on the breadboard together with other components, including an electro-optical phase modulator (EOM) and fast detectors (D). To monitor continuously the transmitter parameters, there were a CCD-camera (CCD) for the pump beam control, a wavemeter (WM) and the spectrum analyzer (SA) implemented.
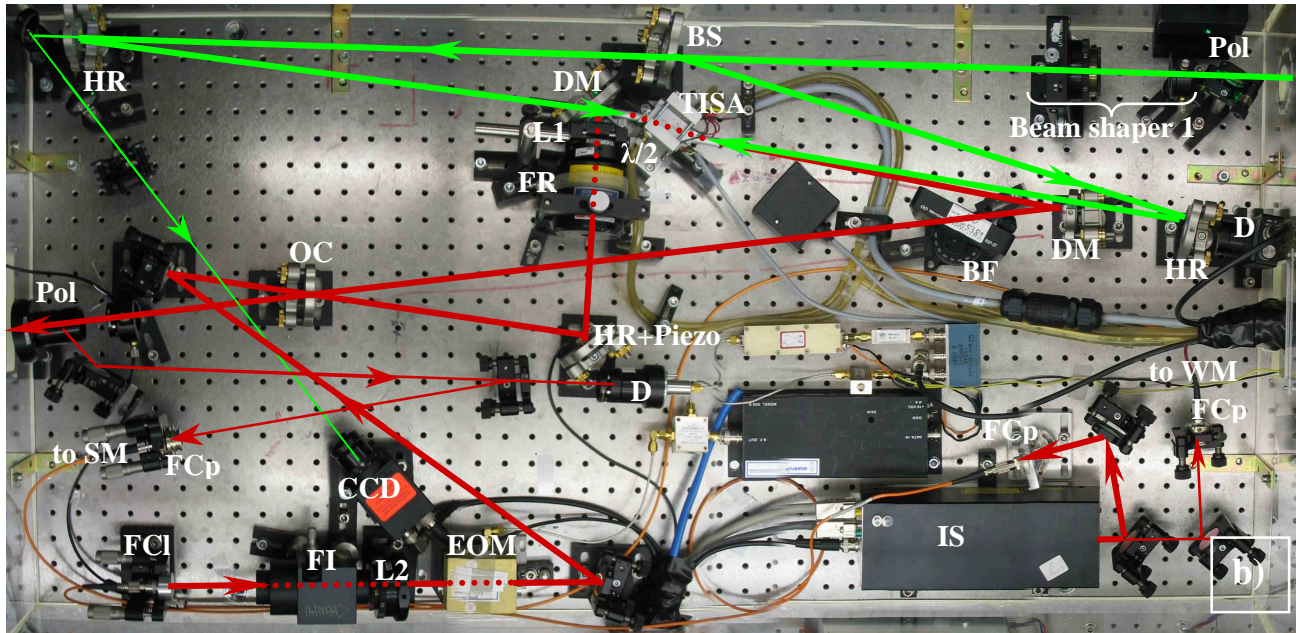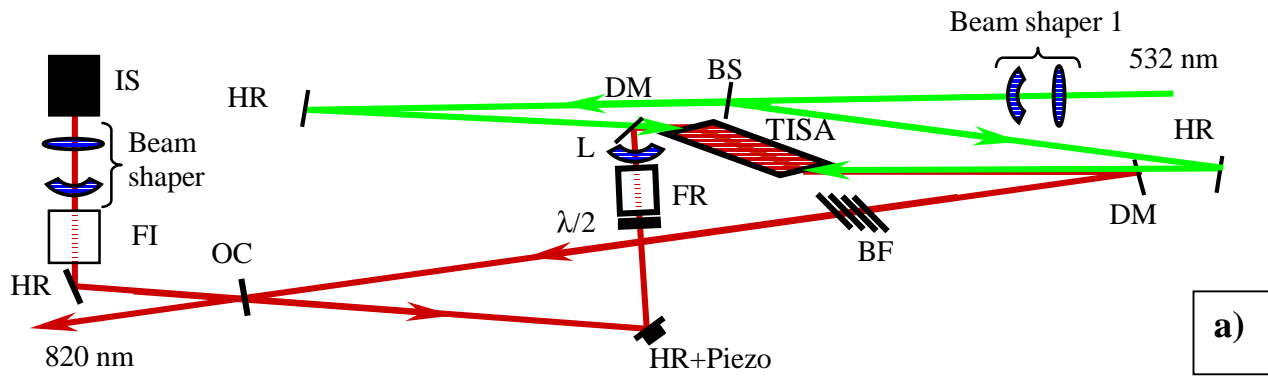
Fig.5.28 Scheme (a) and experimental layout (b) of the TISA transmitter at 820 nm, optimised for the Pump-2. The cavity length is 1500 mm, the cylindrical lens L1 with the focal length of –980 mm in the tangential plane was mounted 70 mm away from the end-surface of the TISA rod. Here BS – beam splitter, HR – high reflection mirror, DM – dichroic mirror, FR – faraday rotator, λ/2 – halfwave plate, BF – birefringent filter, OC – output coupler, Piezo – high-voltage piezo actuator, IS – injection seeder, FI – faraday isolator, L2 – second lens of the beam shaper of the IS, EOM – electro-optical phase modulator, D – biased photodetector, Pol – polarizer, CCD – CCD-camera, Piezo – piezo-actuator, FCp – fiber coupler, FCl – fiber collimator, WM – wavemeter, SM – spectrometer.

5.5.2 Output energy and efficiency, pointing stability

For the measurements at 825 nm the pump laser was implemented in configuration Pump-1 with maximum output of 100 mJ and Pump-2 with 180 mJ, corresponding maximum energies absorbed in the crystal of 90 mJ and 140 mJ, respectively. The cylindrical lens was deployed in the layout of the TISA laser only when it was pumped with the Pump-2.

For a high-gain operation at 825 nm the laser-induced damage threshold (LIDT) of the polished surface of the TISA crystal becomes a limiting factor for the size of the pump beam on its end-face, especially for operation with the Pump-2 with the higher pump power. The value of the surface-LIDT for the TISA was not specially measured, but estimated during the experiment. The threshold was reached during seeded operation of the transmitter with the pump laser in configuration Pump-1. The peak energy density of $\approx 2.5\ \mathrm{J/cm}^2$ in a 25 ns pump pulse and $\approx 2\ \mathrm{J/cm}^2$ in a 30 ns TISA pulse on the Brewster-cut surface of the TISA crystal was recorded. Figure 5.30 (a) depicts the profile of the pump beam. The damage of the surface occurred when the cavity length was set in a resonance with the seeding emission and the build-up time decreased to < 100 ns. The given values of the energy density are significantly lower than the estimated one of $8\ \mathrm{J/cm}^2$ (see Subsection 5.2.3). Such a behavior of the TISA can be explained by an effect of a severe reduction of the surface-LIDT under a pulse train with a short delay between the pulses [Canova et al., 2005].

The measured slope efficiency of the TISA laser in the same configuration but without injection seeding is drawn on the Fig.5.29 (a). Here the transmitter was running broadband: the axis of the BF was tilted horizontally, tuning it to a 100% transmission for all wavelengths. The slope efficiency in this experiment was 37%, maximum output pulse energy 25 mJ at 95 mJ pump obtained a 26% conversion efficiency. The optimum reflectivity of the OC was found to be 55%. Having the eigenmode radius on the rod of 0.65 mm, its overlap with the pump beam of 77% was obtained. The pulse evolution model gives the best fit for the experimental data at the level of the passive losses of 27% (see Fig.5.29, green curve) and 14% (see Fig.5.29, red curve) for analytical (see Eq. A.12) and numerical solution (see Eq. A.7), respectively. The given discrepancy of the results is due to neglecting the effect of the depopulation of the upper laser level in the TISA in the analytical solution. The 14%-losses can be caused by a non-optimized alignment of the cavity during the first measurements at 825 nm.

After the value of the LIDT of the TISA crystal was experimentally defined, the size of the pump beam on the rod was enlarged. For a long-term safe operation, the pump beam with 1 mm radius
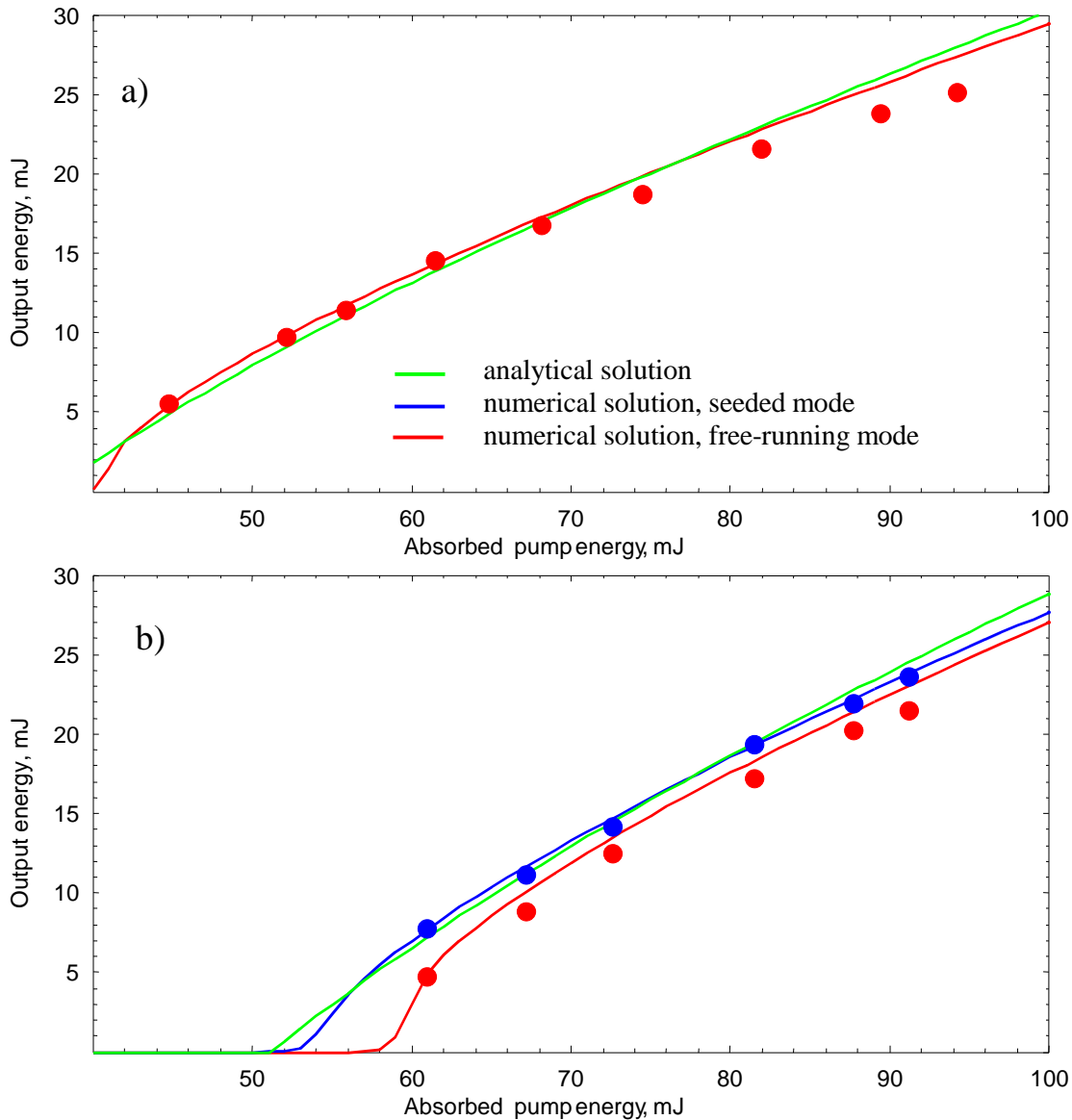
Fig.5.29 Slope efficiency of the TISA laser at 825 nm, operating near gain maximum with the pump source in configuration Pump-1, for a broad-band operation, without BF (a) and for narrow-band operation, with BF (b). Experimental results are marked with dots, numerical solution of the pulse evolution model are drawn with curves of red and blue color for free-running and seeded mode, respectively. With a green curve the analytical solution of this model is drawn.

and a maximum pump energy density on the surface of the TISA rod of 1.4 J/cm^2 was preferred (see Fig.5.30, b). Figure 5.29 (b) shows the measured output pulse energy of the TISA laser at 825 nm, free-running (red) and injection-seeded (blue) in the same cavity but with the new pump beam size. The slope efficiency of the laser was > 50% with a laser threshold of 54 mJ free-running and 50 mJ seeded. The maximum output pulse energy was 24 mJ with an optical energy conversion efficiency of > 26% from 532 to 825 nm.
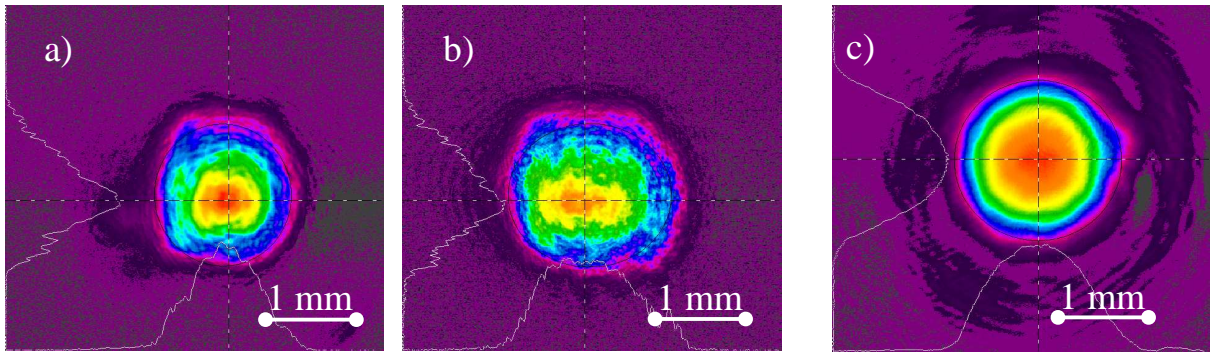
Fig.5.30 Cross-section of the pump beam and TISA beam at 825 nm with the pump laser in the cofiguration Pump-1. Pump beam for the experiment without BF (a) and with BF (b), TISA beam(c).

The difference between conversion efficiencies in the seeded and free-running modes was due to an additional decay of the upper laser level during the longer build-up time of the TISA pulse without seeding, as it was shown in Subsection 5.4.2. The maximum absorbed power was less than in the previous experiment due to a fluctuation of the pump laser output and because of using the TISA crystal with a smaller absorption (96% in the second experiment vs. 98% in the first).

Having a radius of 1 mm, the pump beam excited the larger cross-section of the active medium then it was required for the eigenmode operation (0.65 mm) but not large enough to obtain lasing at the first transversal mode with a radius of 1.13 mm. The simulation using the pulse evolution model gives the best fit for the radius of the intra-cavity field on the rod of 0.78 mm, fitting to the M^2-specification and corresponding the overlap with the pump beam of 74%, and level of passive losses of 5%.

Figure 5.30 (c) depicts the cross-section of the TISA beam at the maximum output energy of 24 mJ, corresponding the intra-cavity pulse energy of 53 mJ. The profile has a near-Gaussian shape and, unlike the output at 935 nm (see Fig.5.15 c), its distortion is negligible. Measurement of the M^2-parameter obtained values of 1.6 and 1.5 in tangential and sagittal plane, respectively. It was performed using a lens with a focal length of $f = 341$ mm. More than 20 beam shots were made with a CCD-camera at certain positions, the same way as for measurements of the thermal lens. Processing the data with a program "Beam Analyzer" (TU Berlin), the main beam parameters were estimated. The trend of the cross-section size of the beam is shown on the Fig. 5.31, separately for the tangential and sagittal plane.
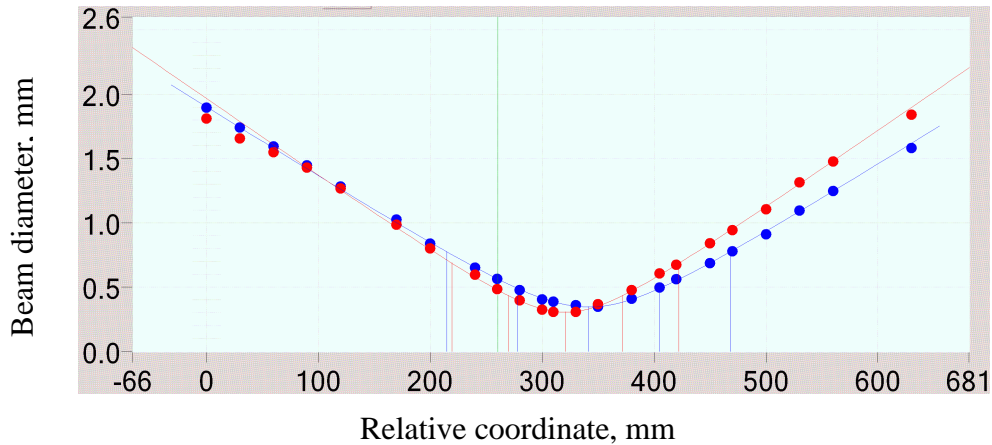
Fig.5.31 M^2-measurement of the TISA beam at 825 nm with the pump laser in configuration Pump-1, red points correspond to the beam cross-section in tangential plane, blue – in sagittal.

The output of the "Beam Analyzer" strongly depends on presets of the program. From several calculated sets of the beam parameters (w_0, z_R, z, M^2), the one was preferred obtaining by the back propagation through the lens the best fit to the waist position of the eigenmode. The back calculation of the preferred solution gave the waist radius of the intra-cavity mode of 0.50/0.60 mm. Comparison with the eigenmode yielded a beam quality of $M^{2\prime} = 1.56/1.44$ in tangential/sagittal plane, respectively. This shows a good fit to the $M^2 = 1.6/1.5$, derived in the program. The values of the corresponding mode size on the TISA rod of 0.81/0.78 mm in tangential/sagittal plane, respectively, were implemented in the simulation of the laser operation (see Fig.5.29, b).

The second set of measurements was made using the pump laser in the configuration Pump-2 with the higher pump energy and the lower beam quality (see Fig.5.33, a). Figure 5.32 demonstrates the output pulse energy of the TISA laser at 825 nm, free running (red) and injection-seeded (blue), as a function of the pump energy at 532 nm, absorbed in the rod. The slope efficiency of the laser was > 60% with a laser threshold of 98 mJ free running and 95 mJ seeded. The maximum output pulse energy was 27 mJ with an optical energy conversion efficiency of $\approx$ 20% from 532 to 825 nm. The simulation using the pulse evolution model gives the best fit to the measured slope efficiency, assuming the radius of the intra-cavity mode on the rod of 0.8 mm and the level of passive losses of $\approx$ 6.5%. This mode size corresponds overlap with the pump beam of $\approx$ 50% at 140 mJ pump energy
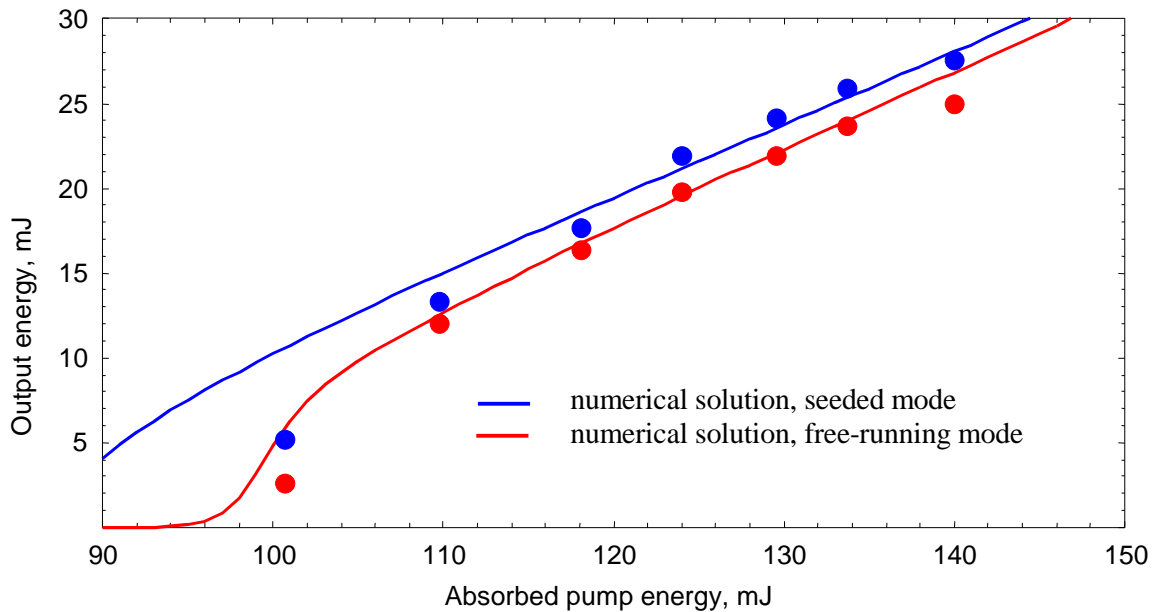
Fig.5.32 Slope efficiency of the TISA laser at 825 nm with the pump laser in configuration Pump-2 in seeded (blue) and free-running (red) modes. Experimental results marked with circles, results of simulation with solid curves of the corresponding colors.
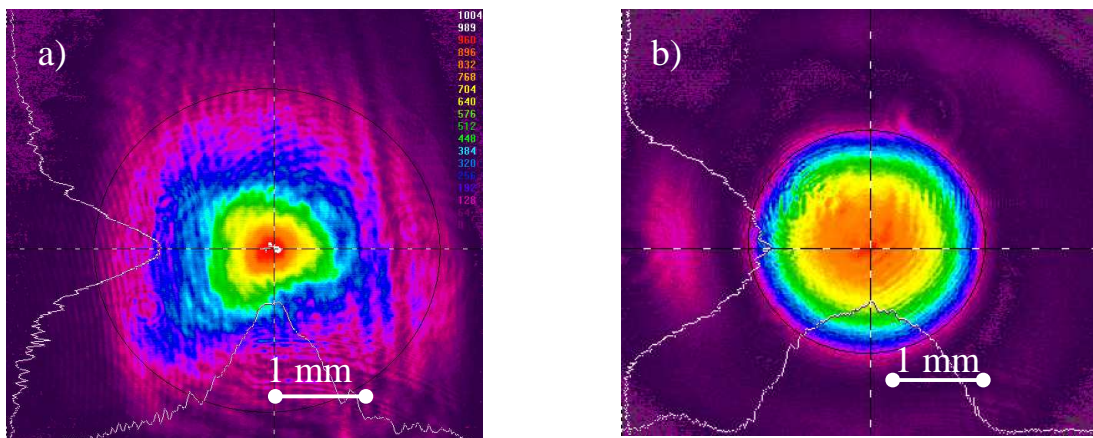
Fig.5.33 Cross-section of the pump beam a) and TISA beam at 825 nm b) with the pump laser in the configuration Pump-2.

Comparing this result with the slope efficiency of the TISA pumped with the Pump-1, a severe increase of the lasing threshold was observed. This is mainly caused by using of the negative intra-cavity lens in the last TISA layout; there was no lasing possible until the growing thermal lens in the crystal compensates the lens with $f = -980$ mm. To include this effect in the pulse evolution model, the overlap between the eigenmode and the pump beam was parameterized with respect to the strength of the thermal lens in the rod using the results of the thermal lens
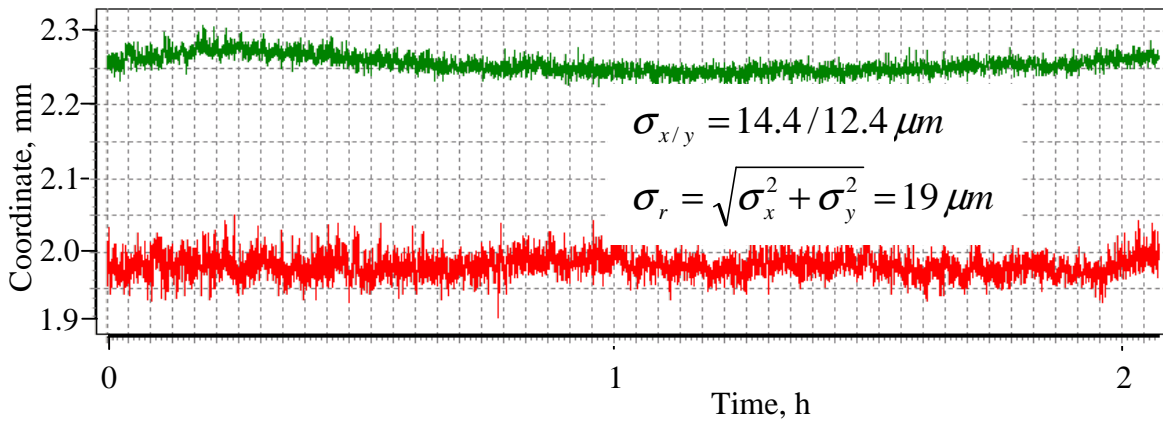
Fig.5.34 Trend of the beam position of the TISA laser at 825 nm in horizontal (green) and vertical (red) planes; the beam was monitored at the distance of 1.5 m from the OC.

measurement, described in Subsection 5.2.4. The energy distribution in the pump beam profile was assumed constant for various pump power. Another reason of the higher threshold and the lower overall conversion efficiency was the worse energy distribution in the pump beam (see Fig.5.33, a). Keeping the peak energy density on the rod surface under 1.8 J/cm^2, the pump beam radius was increased to 1.35 mm with corresponding overlap reduction to 50%.

The TISA-laser beam (see Fig.5.33, b) has a near-gaussian smooth profile with a secondary ring, which makes further beam shaping more difficult. This beam distortion is caused by thermally-induced aberrations in the TISA rod. Pumping with the Pump-1 with absorbed power of $\approx$ 23 W, only 4% of the total pulse energy was disposed in the ring, whereas pumping with Pump-2 and $\approx$ 35 W pump power absorbed yields already 10% of the energy leaked in the ring. The beam quality in the experiment with the Pump-2 was not measured; estimation gives $M^2 <$ 2.

The pointing stability of the TISA laser was derived, monitoring the beam position using a CCD-camera. Figure 5.34 plots the coordinates of the TISA beam center in horizontal and vertical planes, recorded within the time range of 2 hours. The standard deviation of this series is 14.4/12.4 μm in horizontal/vertical plane, respectively.

Taking into account Fig.3.11, fluctuations of the pump beam position on the end-faces of the TISA crystal were considered the major source for the spatial instability of the TISA beam. Hence, inside the resonator the maximum eigenmode displacement corresponds to the crystal plane and the minimum – from the propagation symmetry – to the point a half-resonator length apart from the rod. Thus, the radial standard deviation of the series of $\sigma_r =$ 19 μm at 1.5 m from mid-resonator point corresponds the angular standard deviation of $<$ 13 μrad.
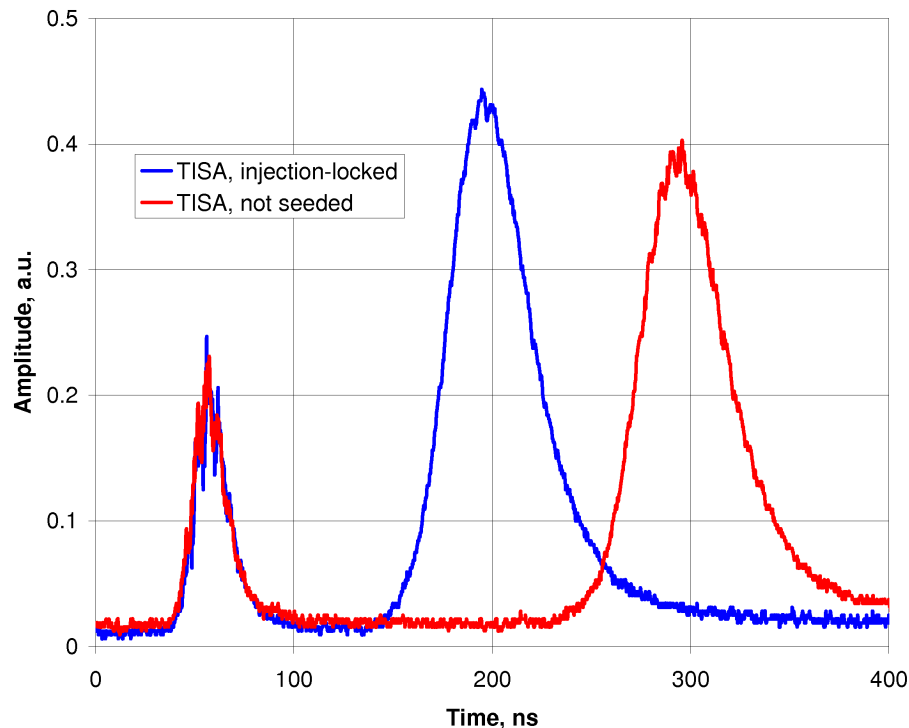
Fig.5.35 Temporal profile of the pump pulse at 523 nm (the first of three) and TISA pulse at 825 nm, seeded (blue) and free-running (red) in configuration Pump-1. A small mode beating in the seeding mode is notable.

5.5.3 Temporal profile of the pulse

In the experiment with the Pump-1 the temporal profile of the TISA laser pulse was recorded with a high-speed photo diode (see Fig.5.35). The first is the pump pulse at 532 nm with a width of ≈ 23 ns (FWHM). The two following pulses with the width of 48 ns and 49 ns present the emission of the TISA laser in the seeded and in the free-running modes, respectively. This measurement showed a build-up time reduction from 240 ns for the free-running operation to 140 ns for the seeded mode (full pump power, measured peak-to-peak). TISA laser in the seeded mode was operating almost single mode – a small mode beating is still notable. With the Pump-2 the laser yields similar temporal shapes and delays of the pulses.

Figure 5.36 illustrates the dependence of the pulse width and the pulse build-up time of the TISA laser from the energy in the pump pulse in the configuration Pump-2. At a high pump power the pulse duration is the same in the seeded and not seeded modes, corresponding the classical pulse evolution model (see Eq.A.15). But at a low pump power the pulse width in the free-running mode is longer due to severe gain drop near the lasing threshold, not considered in this equation. The build-up time difference of > 300 ns at 110 mJ pump power corresponds $> 10\%$ additional depopulation of the upper laser level, yielding remarkable grow of the pulse width.
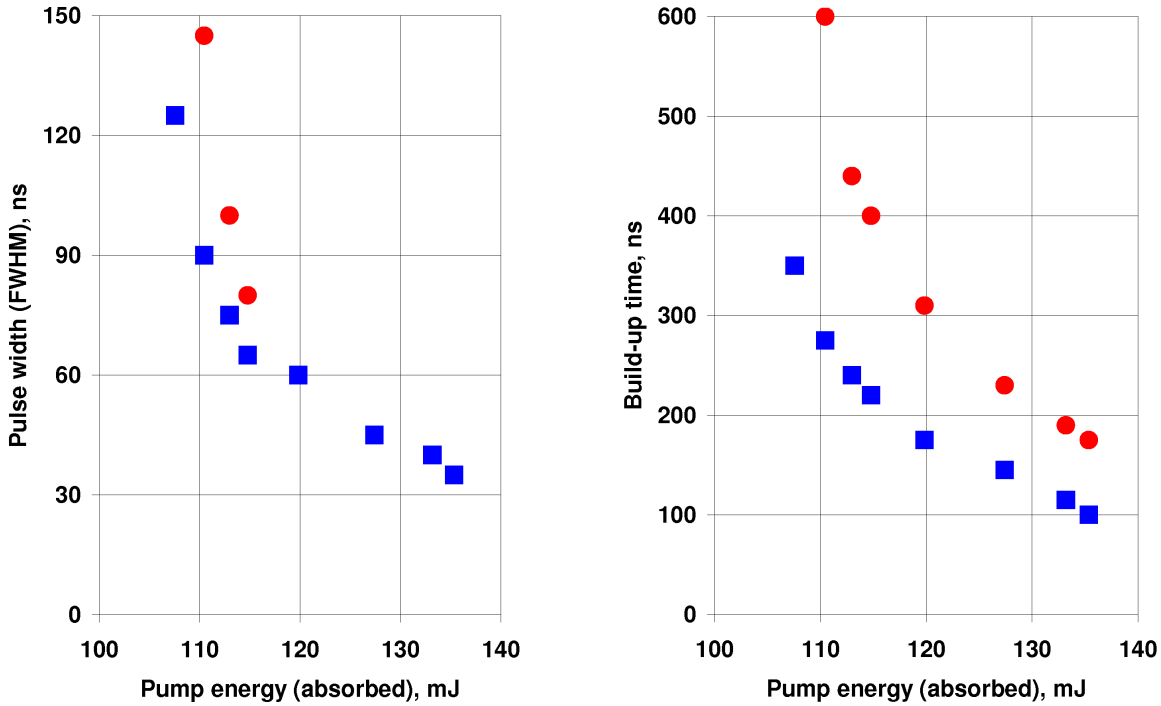
Fig.5.36 Pulse width (left) and pulse build-up time (right) of the TISA laser at 825 nm vs. absorbed pump energy. Results of the TISA with seeded emission marked blue, free-running – red.

5.5.4 Spectral properties – bandwidth and frequency stability

To fulfill the requirements for the ground-based water-vapor DIAL (see Table 2.1), the frequency deviation of the TISA must be kept less than 200 MHz rms with correspondent bandwidth < 400 MHz. But this is valid only for the boundary layer. To perform measurements up to the top of the troposphere with an overall instrumental error < 5%, system specifications must correspond ones for the airborne DIAL, namely < 160 MHz bandwidth and < 60 MHz frequency stability.

Applying the injection-seeding technique, theoretically the bandwidth of the transmitter can be narrowed down to a Fourier-transform limit, giving a linewidth of 11 MHz for the pulse of 40 ns long (FWHM). In practice the bandwidth of the slave laser is always broader due to instabilities of resonator parameters and the pump power. For the fine specification of the spectral properties of the TISA, the spectrum analyzer with a FSR of 7.5 GHz was implemented as it was described in Subsection 5.4.4. Figure 5.37 depicts the fringe patterns of the emission of the TISA laser, locked to the frequency of the IS (left) and the emission of the single-mode cw IS. The multiple secondary pattern on the plots is caused, obviously, not by the spectral properties of the lasers but diffraction effects on the 5-mm mirrors of the SA and aberrations of the imaging lens.
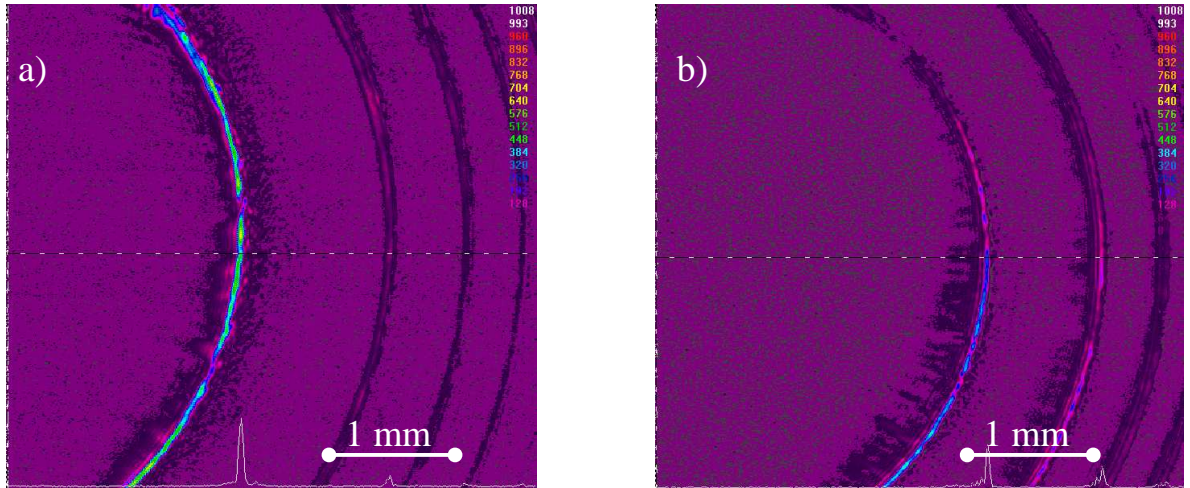
Fig.5.37 Fringe patterns of the laser emission build in a confocal FPI and recorded with a CCD-camera. Here are the measurements of the seeded TISA laser (a) and the single-mode cw IS (b) at 820 nm. The shots were shifted rerding the center of the fringes to capture simulteneously at least three rings for an accurate definition of the departure of the mirrors and magnification of the optics.
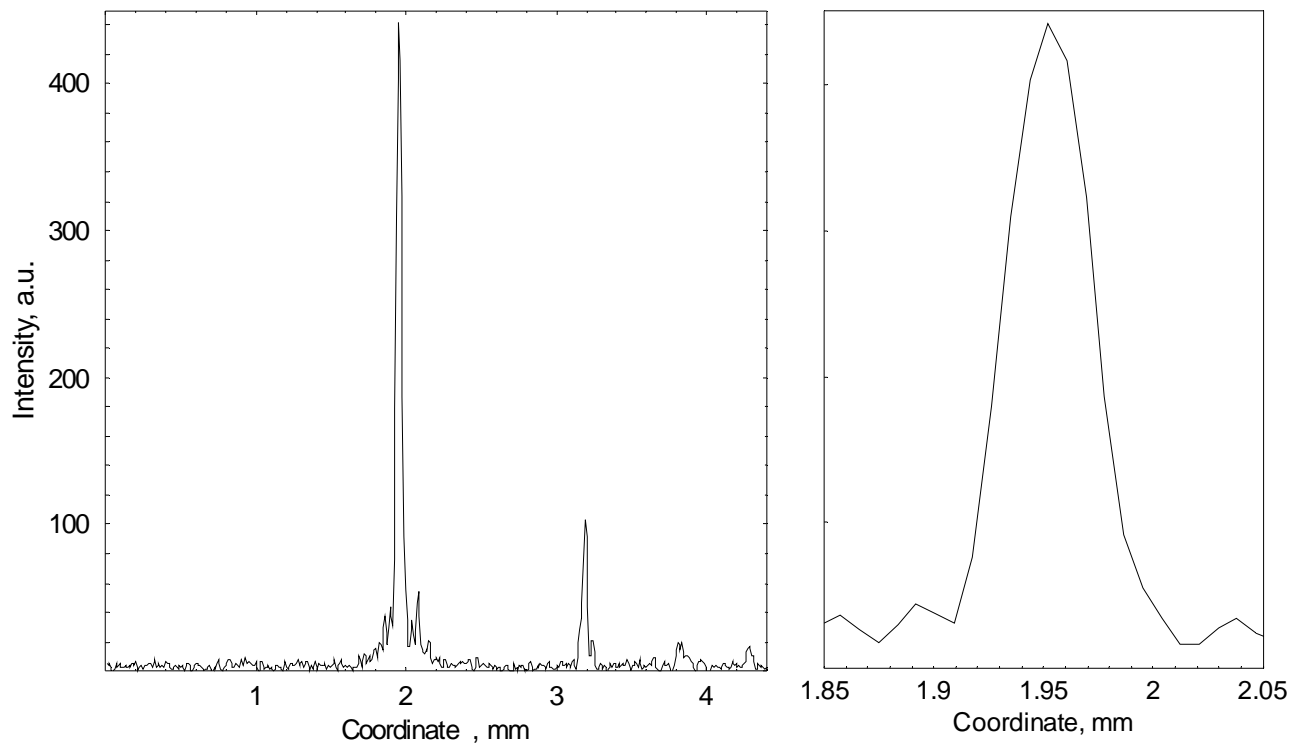
Fig.5.38 Intensity distribution in the fringe pattern of the injection-locked TISA laser at 820 nm along the horizontal main axis of the fringes (left); corresponds the horizontal dashed line on the Fig. 5.38 (a). Scaled cross-section of the first-order ring is imaged on the right, cell width of the CCD-array is 8.6 μm.
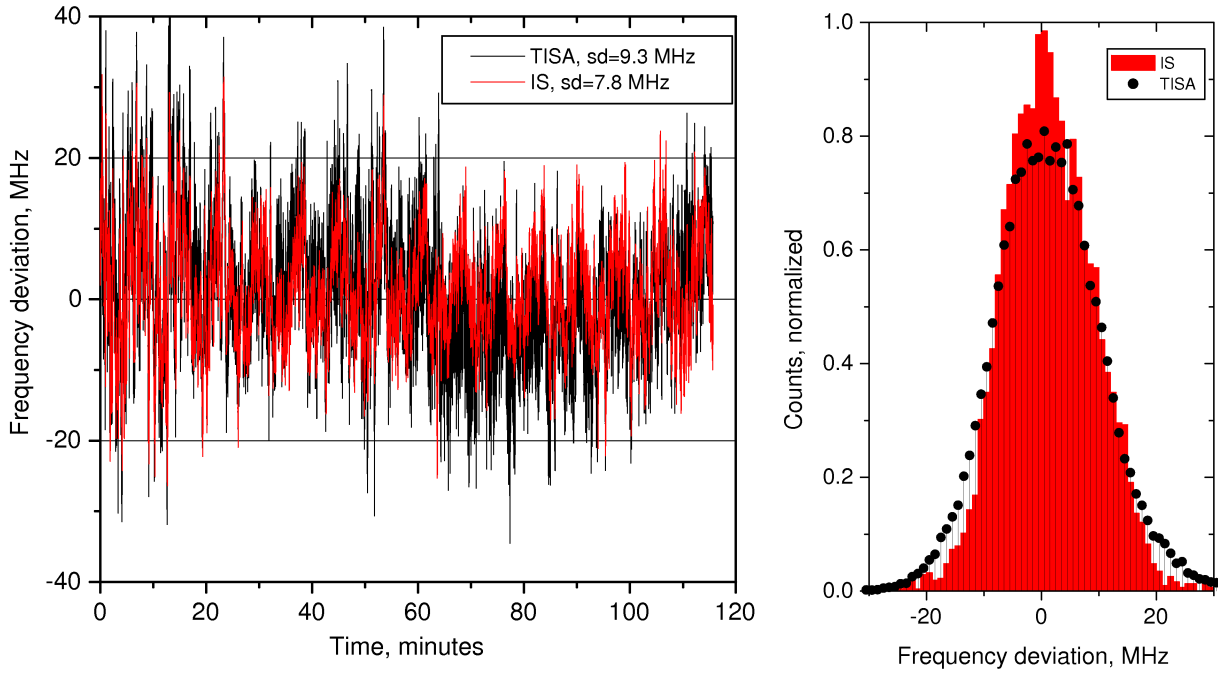
Fig.5.39.Measured frequency deviation of the injection seeder (red) and injection-locked TISA laser (black) within a 2-hour trend (left) and its statistics (right).

This measurement as well as further specifications of the TISA transmitter were performed in a trailer of a ground-based DIAL (see Subsection 6.1) with the pump laser in the configuration Pump-2 and the IS from DLR Oberpfaffenhofen the wavelength of 820 nm.

Figure 5.38 presents the intensity distribution in the fringe pattern of the injection-locked TISA emission along the horizontal main axis of the fringes (left), corresponding the horizontal dashed line on the Fig. 5.37 (a). The scaled cross-section of the first-order ring is depicted right, the cell width of the CCD-array is 8.6 μm. Regarding Eq.5.10 the bandwidth of the presented TISA signal is < 157 MHz (departure of the mirrors in FPI is 11 μm, magnification of the imaging optics is 3.9).

Frequency stability of the injection-locked TISA laser was measured with a pulse wavemeter (HighFinesse, WSU-423) (see Fig. 5.39). The overall instability of the IS emission was < 8 MHz 1σ and of the TISA emission < 10 MHz 1σ. The frequency fluctuation of IS output with a period of ~10 minutes was influenced by the environmental instability, namely temperature drift in the trailer. The short-time jitter was caused, likely, by mechanical vibrations. The spectrum of the TISA emission was conducted by the IS. The larger frequency drift of the transmitter was due to a drift of the pulse wavemeter itself, whereas the separate wavemeter of the IS was continuously calibrated with a stabilized HeNe laser (see Subsection 4.4.2).
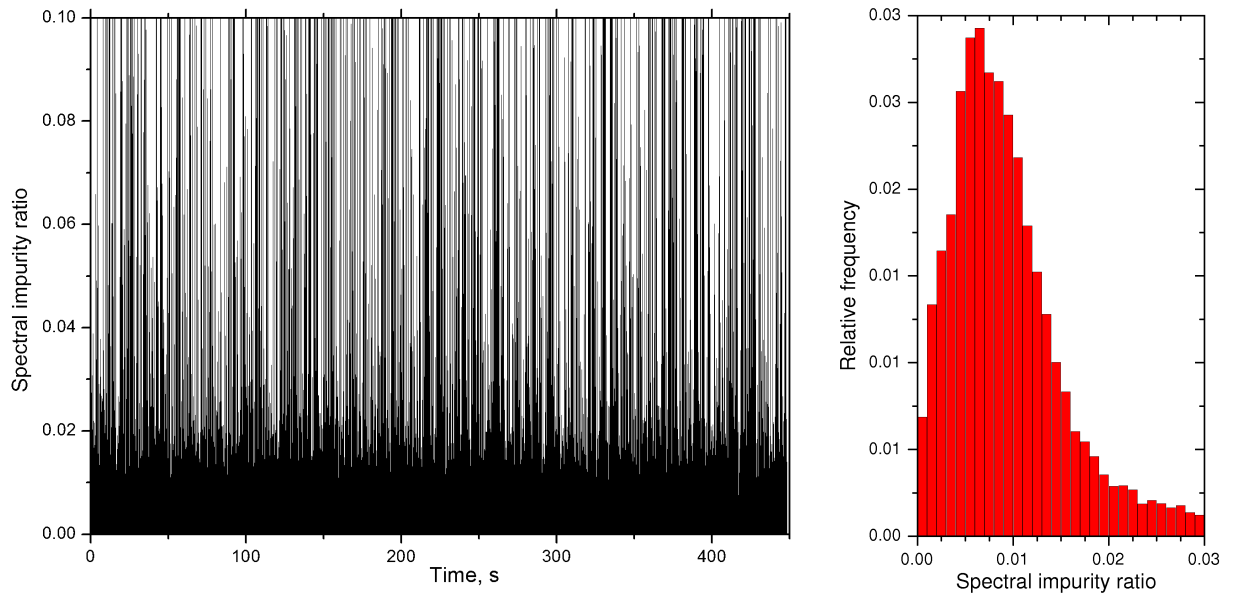
Fig.5.40 Spectral impurity measurement of the TISA transmitter with a DIAL-system in coaxial configuration. Here is presented shot-to-shot 450 s trend of the spectral impurity ratio I_{on}/I_{off} (left) and the correspondent statistics (right). Assuming all the negative data having a noise nature, they were removed from the final statistics.

5.5.5 Spectral properties – spectral purity.

The last spectral feature of the TISA transmitter important for the DIAL measurement is a spectral purity (SP), practically defined for the laser emission tuned at the center of an absorption line as a fraction of spectrum emitted within this line. The 30-m multipass absorption cell used for specification of the SP at 935 nm cannot be implemented in the current experiment: the strongest line in the band at 817.922233 nm (see Table 5.3) has an absorption intensity of $S = 5.25 \cdot 10^{-23}$ cm. In the cell filled only with water vapor at a pressure of 20 mbar a peak absorption cross-section of this line is $9 \cdot 10^{-20}$ cm^2, yielding a transmittance on the 30 m and 60 m track (double pass) of 25% and 8%, respectively. To qualify the laser with the required SP of 99.7%, an absorption cell with the optical length of > 150 m has to be deployed.

The spectral purity specification of the transmitter can be performed using the DIAL system. For this measurement a steering unit of the DIAL (see Fig. 6.1) was orientated horizontally to hit a hard target (top of a mountain) at a distance of ≈ 15 km away from the device. Comparing intensities of the back-reflected signal at the online and the offline wavelengths, the value of the spectral impurity was derived. For a temperature of 298 K, a relative humidity of 60% and an air pressure of 90 kPa, the atmospheric transmission on this track for the laser emission centered at the absorption line G5 (820.294513 nm) is $< 10^{-4}$% and residual absorption can be neglected. Thus spectral purity can be calculated as $SP = 1 - I_{on}/I_{off}$.

Figure 5.40 (left) presents a shot-to-shot trend of the spectral impurity ratio I_{on}/I_{off} for the duration of 10 minutes. Numerous of online shots were not spectrally clean, for 68% of measured values the spectral purity is $SP > 99\%$ (see Fig.5.41 right). The reason is a bad work of the stabilization circuit when an optical chopper in front of the receiving detector was operated (see Subsection 6.2). The produced mechanical and acoustical vibrations affected the cavity length and destroyed the correction signal of the feed-back loop. Thus, the DIAL system in the present configuration can not be qualified for scanning measurements.

To derive the spectral purity of the transmitter more accurately, a DIAL data from a vertical profiling of atmospheric water vapor was implemented. For this measurement, the DIAL was switched in a bi-axial configuration with the optical chopper disabled (see Subsection 6.1). The SP value was estimated, comparing water-vapor profiles derived with the DIAL with *in-situ* measurements of a radiosonde, taken for a reference.

Figure 5.41 depicts profiles of the water-vapor number density derived during a 1.25-hour DIAL measurements on 1st August 2007. To reduce the noise, DIAL data was temporally averaged over 15 minutes and split in five profiles, covering time range from 1022 UTC to 1135 UTC. Averaging within a 15 minutes frame allows for a severe improve of the SNR, and this time range is short enough to neglect variations of the atmospheric parameters. The 1.25-hour average was also calculated (marked red on the plot). The data from the radiosonde launched at 1057 UTC is drawn with a black curve. The information on the water vapor number density was extracted from the DIAL signal implementing a 600-m average for derivative calculation. To achieve a comparable smoothing, a 150-m gliding average was applied to the water-vapor profile of the radiosonde.

The spectral impurity applies a positive bias to the measured water-vapor number density, and the induced error at a distance *r* from the DIAL can be calculated as [Bösenberg, 2005]:

$$\frac{\Delta n}{n}(r) = \frac{1 - SP}{(1 - SP) + SP \cdot \exp(-2\tau(r))}, \tag{5.11}$$

where *n* is the number density of the water vapor, *τ(r)* is optical thickness of the track *r*. Figure 5.42 represents the height-dependent value of the relative error, induced in the water-vapor number density derivation by different values of spectral impurity of the transmitter signal (the necessary atmospheric parameters were taken from the radiosonde measurements).
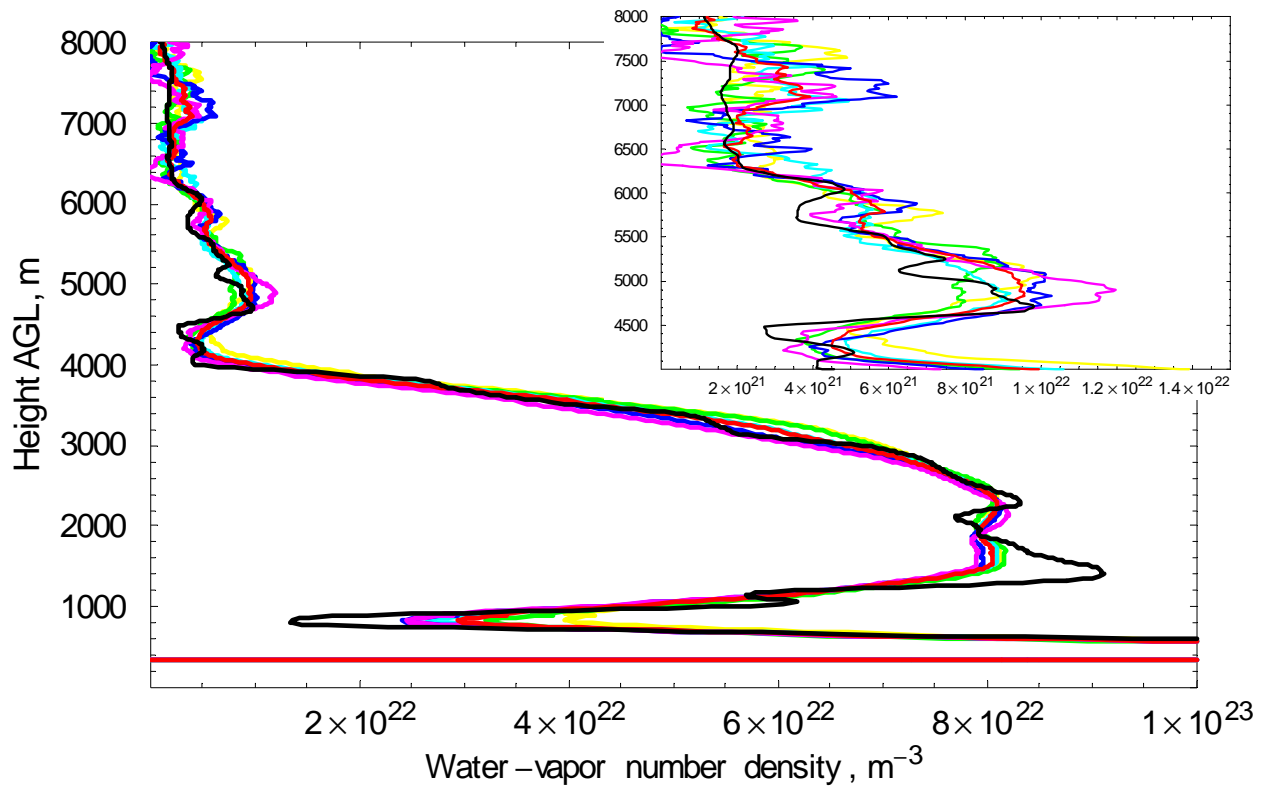
Fig.5.41 Water-vapor number density profiles, obtained with the DIAL (color curves) and radiosonde (black curve) from 1 August 2007 1020-1135 UTC, Hornisgrinde. DIAL profiles are averaged over 15 minutes and have a 600-m window gliding. Radiosonde data was smoothed with a 150-m gliding window.
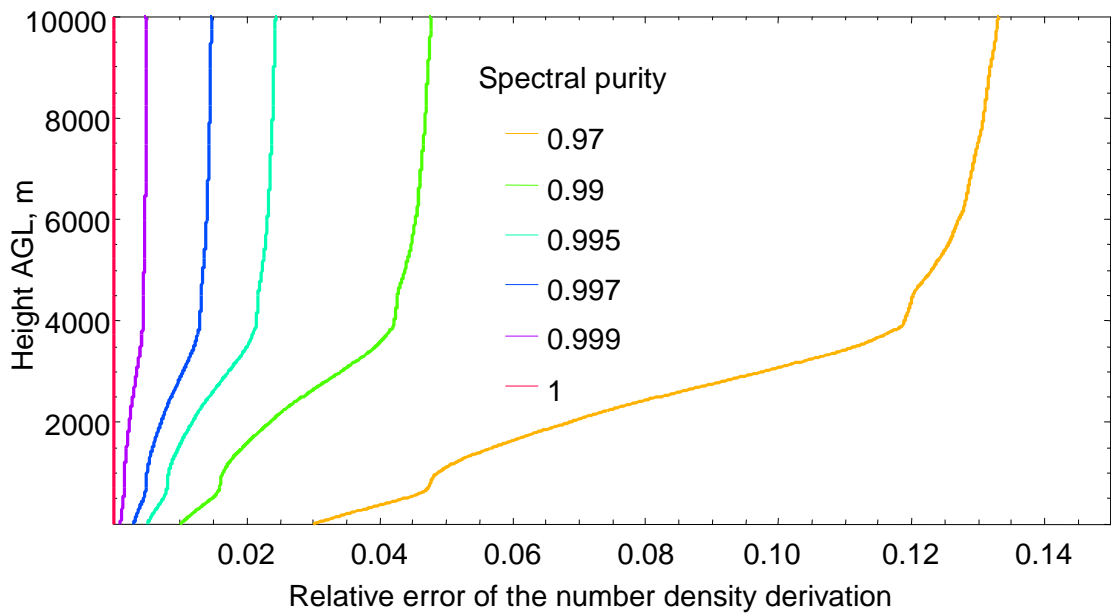
Fig.5.42 Relative value of the spectral-impurity induced error for derivation of the water-vapor information from a DIAL-measured profile on variuos heights. Atmospheric conditions are simulated regarding the radiosonde measurement on 01 Aug 2007, 1057 UTC, Hornisgrinde.
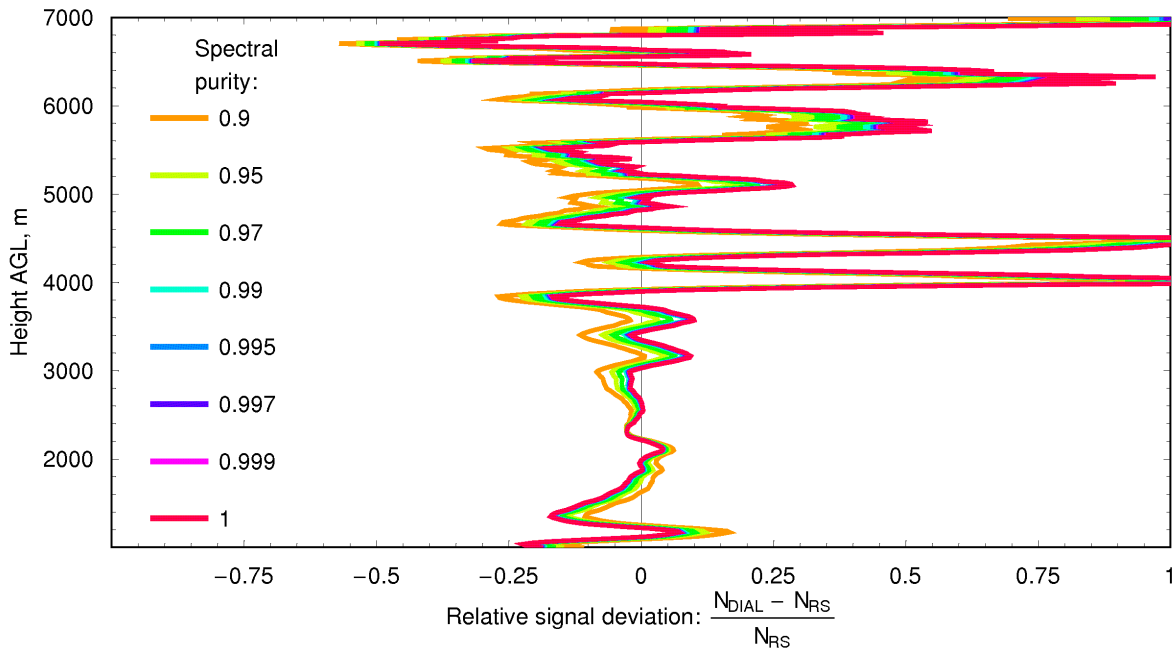
Fig.5.43 Relative deviation between DIAL and radiosonde signals for measurement on 1st Aug 2007, 1100 UTC. A spectral-impurity correction was applied to the DIAL profile, averaged around the launch time of the RS. Different curves on the plot corresponds different levels of the estimated spectral purity of the DIAL emission, from 90% to 100%. The one with the smallest bias indicates the expected value of the spectral purity.

Every water-vapor profile of the DIAL was corrected for a specific value of the spectral impurity. To eliminate the bias induced by uncertainty of the absorption cross-section data, the corrected DIAL profiles were scaled to fit the profile of the radiosonde at heights 2000-2700 m. Afterwards, the profiles were compared with the radiosonde in the region 4600-5500 m (see Fig.5.43), the best fitting one represents the most probable value of the spectral purity. Calculating the mean value of the ratio $\frac{n_{DIAL}}{n_{RS}}$ for different time series, the profile covering the launch time of the radiosonde (1051-1106 UTC) showed a SP of $> 99.9\%$ (standard deviation 10%).

Although the result varies a lot regarding the intercomparison range chosen, and the severe data jitter makes this qualification rather uncertain, it can be verified that the atmospheric water-vapor profiles derived in the bi-axial mode were free from frequency jumps of the 'online' emission and the overall signal quality is better. Therefore, SP of the transmitter at 820 nm was defined as $> 99.6\%$. Taking into account the achieved frequency stability of < 10 MHz, the specification for the spectral purity can be moderated down to SP $\geq 99.3\%$ with respect to the requirement of the

overall instrument error of $< 5\%$ (see Subsection 2.2). Thus, the DIAL can be allowed for the accurate water-vapor measurements up to the top of the troposphere.

The back-scattered signal of the DIAL can be used for estimation of a shot-to-shot energy stability of the transmitter. The standard deviations of the measured series were 3.7% and 3.4% for 'online' and 'offline' signals, respectively.

5.5.6 Summary of the 820 nm experiment

In the following table the requirements for the laser transmitter for the ground-based DIAL reference system together with the experimentally achieved values are summarized.

Although the final goal of 10 W output power was not achieved, the power of 7 W of the transmitter is the highest average power obtained with a TISA laser at 820 nm, emitting single-mode with a near-Gaussian beam profile. To increase the output power, the single-rod transmitter can be expanded in a MOPA configuration (see Subsection 7.2.2 for a more extensive discussion).

Table 5.4 Summary of the requirements for the ground-based water-vapor DIAL system and results of the experiment at 820 nm.

Parameter	Required	Reached
Wavelength, nm	820	820-825
Average power, W	10	7
Pulse energy, mJ	40-10	27
Repetition rate, Hz	250 – 1000	250
Pulse duration, ns	< 200	40
Pulse linewidth, MHz	< 160	157
Frequency instability, MHz 1σ	< 60	10
Energy instability, 1σ	$< 4\%$	$< 3.7\%$
Tunability, GHz	± 10	$> \pm 10$
Beam quality, M^2	< 2	< 2
Depolarization ratio	$< 1\%$	$< 1\%$
Spectral purity	$> 99.7\%$	$> 99.6\%$
Pointing instability, μrad 1σ	15	< 13

The other specifications do fit the requirements for the transmitter for the ground-based water-vapor DIAL system, except the spectral purity in the scanning mode. Possible ways to solve the problem are presented in the Subsection 7.2.

5.6 Summary

The high-power high-energy TISA transmitters for the ground-based and airborne water-vapor DIAL were created and specified to fulfill the requirements for the accurate water-vapor measurements in the troposphere, summarized in the Table 2.1.

The developed thermal model considered the astigmatism of the thermal lens in the laser rod with the end surfaces cut at the Brewster-angle.

The resonator design model considers the thermal lensing and allows for optimization of the cavity parameters with respect to dynamical stability of the eigenmode and its minimum size along the resonator. The matrix-based model offers a simple scalability for any reasonable number of the cavity elements. The experimental results yield a good fit to the theory.

The pulse evolution model expands the traditionally used analytical solution of rate equations, referring to a fast decay time of the upper laser level of the TISA crystal. Using the new model, a discrepancy of the output energies in the seeded and free-running modes was explained. However, the model has to be completed in the part of the free-running lasing and the seeded lasing without master-slave frequency matching.

Designing a high-energy high average power transmitter, rather the Brewster-cut prisms have to be preferred for a coarse spectrum definition than the mirrors with thick multilayer coatings. The latter have a lower damage threshold and, likely, cause a wavefront distortion at high energy densities.

The experiment with the TISA laser revealed limitations on applicability of a single-resonator configuration with the high-energy high repetition rate pump source. In the current layout with the rod length of 2 cm and cavity the lengths from 130 to 160 cm to achieve an overlap between the eigenmode and the pump beam $> 90\%$, the maximum pump pulse energy has to be confined to 88 mJ at a repetition rate of 250 Hz. This limitation is caused by the decreased at this rate surface-LIDT of the TISA, which defines the maximum safe energy density of the pump beam and of the cavity mode. Possible solutions to overcome this boundary are given discussed in Subsection 7.2.2.

Chapter 6

Water-vapor differential absorption lidar and measurements during COPS

6.1 Ground-based mobile platform for the differential absorption lidar

The TISA transmitter was build as a part of the ground-based water-vapor DIAL, designed and manufactured within the framework of DFG package proposals "Lidar Reference System based on a High-Power-Laser". The proposal consists of the following parts:

- Project 1 (P1) is dealing with a high-power rod-based pump laser system and is performed by the Chair of Photonics of Potsdam University, Germany. The title of P1 reads "Diode-Pumped High-Brightness Solid-State Rod Laser with ns-Pulses in the Joule-Range". The pump laser used for the experiment is a prototype system, where new techniques were tested to implement in the advanced, more powerful model.

- Project 2 (P2) has the title "High-Power, Injection-Seeded Ti:Sapphire Laser Designed for Frequency Conversion of a 200-W Diode-Laser Pumped Laser System". This project includes the TISA laser described in the theses, and the injection-seeding module, designed at the Institute for Atmospheric Physics (IPA) of the German Aerospace Center (DLR) in Oberpfaffenhofen (see Subsection 4.4.2). The combination of the lasers developed in P1 and P2 is a high-power laser transmitter for water-vapor DIAL measurements.

- Project 3 (P3) is the "Development of a Mobile Platform with Scanner for Determining the Atmospheric Absolute Humidity". The Institute for Tropospheric Research (IfT) in

Leipzig performed this work. The laser transmitter developed within P1 and P2 was incorporated in a mobile platform with a scanning capability and was equipped with an efficient, low-noise receiver system as well as a data acquisition system.

Figure 6.1 (a) reveals the principle layout of a transmitter-receiver part of the DIAL. The Nd:YAG laser pumps the TISA laser with an average power of 45 W at 532 nm. The outgoing beam of the TISA at 820 nm is enlarged with a 5^x beam expander and passes an axicon. The *s*-polarized beam reflects on two large-aperture thin-film polarizers, passes second, 3.4^x beam expander and a quarter-wave plate (QP). The mount of the telescope has steering capability with two degrees of freedom: it can be rotated 380° azimuthally and ±90° by elevation. The outgoing laser pulse is delivered to the telescope' secondary mirror through series of bending mirrors. The axicon obtains doughnut-shape of the energy distribution in the outgoing beam, avoiding its obscuration on the aperture of the secondary mirror of the telescope, assembled regarding the Cassergian scheme with two parabolic mirrors.

The laser energy backscattered in the atmosphere is concentrated with the telescope and propagates back to the QP and then to the beam expander. After the double pass through the QP, the originally *s*-polarized laser energy yields a *p*-polarization regarding the TP. With minimal losses on the TP it propagates through the first beam reducer (BR) of the detector unit. A beam splitter chips off around 10% of the signal in the near-field channel with the rest 90% used for a far-channel. While in the first branch the energy is focused with a second BR on an avalanche photo diode (APD), in the far-field channel a fast optical chopper is mounted in a focal plane of another BR. The chopper is triggered to the pump pulse to block the strong atmospheric backscatter emission from the first kilometers of the atmospheric track and the stray light from the enlarging and steering optics of the transceiver Thus the high-gain APD is prevented from saturation and optical damage, yielding better SNR for the far-field detection. This design of the detector unit allows to cover a signal intensity range of several orders of magnitude without saturation of the detectors. The analog signal from APDs is converted with a broad-bandwidth analog-digital converter (ADC) and the values are stored by a data acquisition system.

After first DIAL measurements was found that mechanical vibrations of the optical chopper destroy operation of the stabilization circuit of the TISA laser. Therefore, water-vapor profiling of the atmosphere was realized in a bi-axial mode (see Fig. 6.1, b).
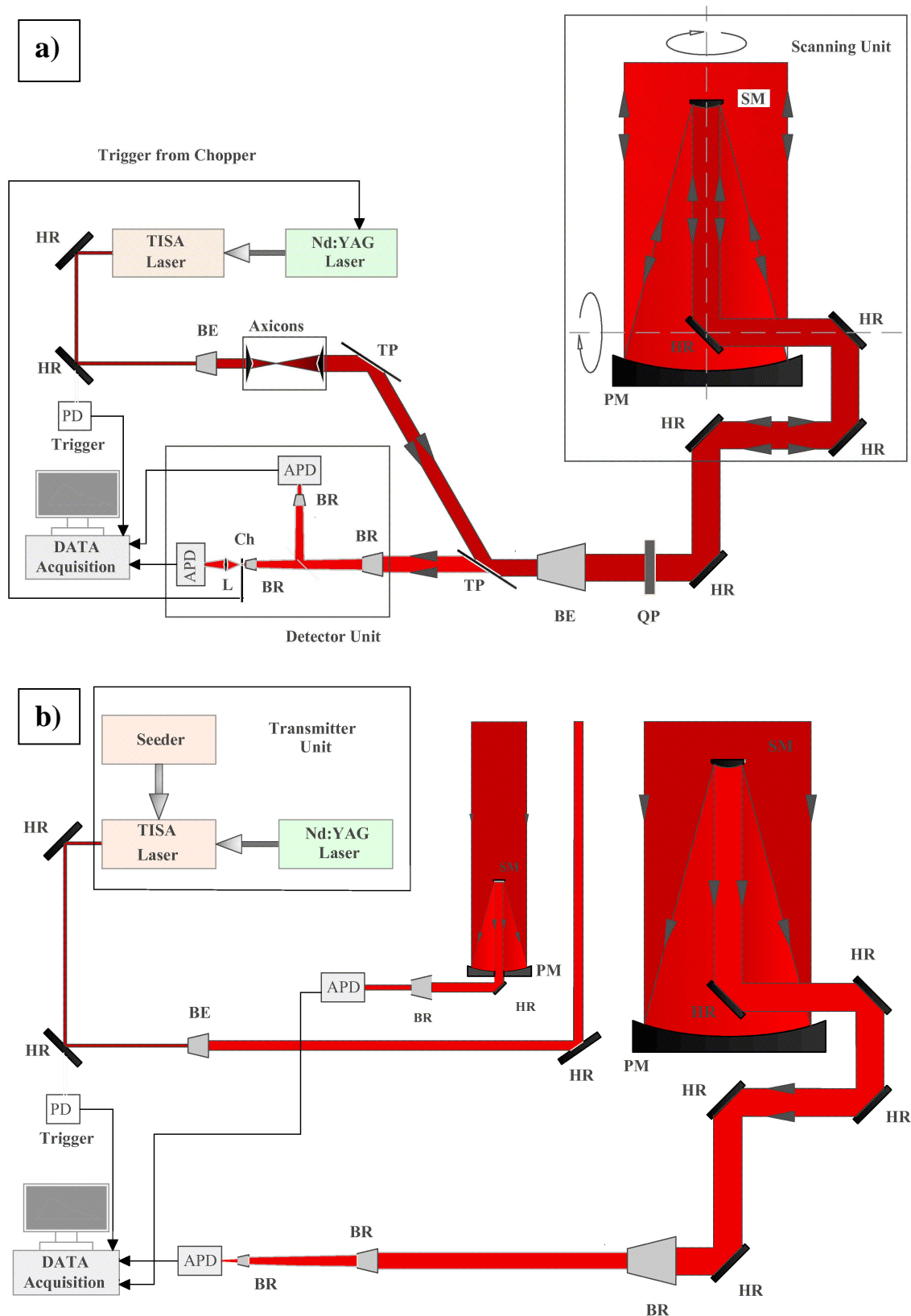
Fig.6.1 Principle scheme of the water-vapor DIAL in coaxial (a) and bi-axial (b) configurations (courtesy of Dr. Riede, IPM). Here: BE – beam expander, TP – thin-film polarizer, QP – quarter-wave plate, HR – high-reflection mirror, PM and SM – primary and secondary mirrors of the telescope, BR – beam reducer, Ch – fast chopper, L – lens, PD – silicon photodetector, APD – avalanche photodetector.

Fig.6.2 Photo of the mobile platform for the water-vapor DIAL. A – energy module, B – laboratory module and C – telescope compartment.

In this mode the telescope is aimed vertically, the output of the transmitter after the first beam expander is sent into atmosphere. For the co-alignment of the beam and telescope axes, an additional 2" bending mirror was applied. Thus, the saturation of the detector with the transmitter pulse backscattered on the optics of the transceiver is avoided and the chopper is removed from the layout. For the near-field channel an additional 20-cm telescope is implemented.

The mobile platform was designed at Institute of Tropospheric Research, Leipzig and manufactured in Fahrzeugbau und Entwicklungswerk Paul Deckwerth Company, Wurzen (see Fig.6.2). The trailer is separated into three modules. Compartment A – the energy module – is intended for the devices that could cause mechanical vibrations and influence the stability of the optical systems of the transmitter and the receiver, namely air condition, cooling system of the laser, Diesel generator and air compressor. For the measurements, the module is mechanically separated from the rest of the trailer. Section B contains laboratory module, equipped with the mechanical frame that carries the optical benches. Part C is the transceiver module, where transceiver, made specially for this system, is kept for transportation. For measurements the roof of the compartment is rolled aside and the scanning telescope is lifted up as it is shown on the photo.

In the compartment B three optical tables are mounted together, forming an optical bench with size of 6x1.2 m. The pump laser, TISA laser and the transmitter-receiver part until the quarter-wave plate are mounted on it. The scanning telescope and the optical bench are fixed on a specially designed base plate 6.4 m long, 1.2 m wide and 30 cm thick. Having the maximum static deformation of < 0.3 mm over the whole length, this plate preserves the alignment and obtains a very good mechanical stability for the optical path from the TISA laser though the transceiver optics to the telescope and back to detectors.

For transportation the optical bench is lifted up using eight high-pressure air-balloons to decrease the probability of mechanical damage of the equipment. Specially designed guides obtain the default position of the bench after sinking. Nevertheless, the alignment of the optical set-up has to be verified after each transportation.

This mobile platform was delivered in Hohenheim in November 2006 with mounted transceiver and data acquisition system. Works on assembling the pump laser, TISA, IS and collateral electronics and alignment of the optics were started immediately. In the May 2007 system was ready for operation and participated COPS measurement campaign in June-August 2007. The system was located on the top of Hornisgrinde, the highest mountain of the north Black Forest, Germany. During this field experiment more than 300 hours of water-vapor measurements with a high spatial and time resolution were collected.

6.2 Measurement campaign COPS 2007

6.2.1 About COPS

Significant deficiencies of quantitative precipitation forecast, which are existing for many years, led to the initiation of the Priority Program (PP) 1167 "Quantitative Precipitation Forecast PQP" by the DFG in 2003 (PQP stands for "Praecipitationis Quantitativae Praedictio"). This research program addresses the challenges identified by many user groups with respect to QPF. The program gathers atmospheric scientists at German and Swiss universities as well as research institutes to combine their knowledge for improving QPF. In close cooperation with the German Meteorological Service (DWD), its operational forecast systems are used and refined as a basic backbone for model development, testing, and validation. For more details see [Hense, 2004; Wulfmeyer et al, 2008a; www.uni-hohenheim.de/spp-iop].

The priority program focuses on reaching the following scientific objectives:

- identification of processes responsible for deficiencies in QPF;

- determination and use of the potentials of existing and new data as well as new process descriptions to improve QPF;

- determination of the predictability of weather forecast models by combined statistical and dynamical analyses with respect to QPF.

The PQP consist of the three phases. The first – Preparation – started April 2004 and lasted for three years and was dedicated to coordination of further measurement and modeling activity of the participants. During this time five specialized workshops, several conferences and symposiums were performed. The second, experimental phase, comprise a large-area observation phase of one year (General Observations Period, GOP) from January to December 2007, and a dedicated experiment regarding the precipitation process over several months, COPS, providing high-resolution, four-dimensional measurements of atmospheric variables.

The third phase – Data Analyses – started in January 2008 and will run until April 2010. Within this time the acquired data is to be processed and used for improving existing weather and climate models.

6.2.2 In-field operation of the Ti:sapphire transmitter

During COPS, the TISA laser was working for more than 300 hours, some days > 20 hours continuously, showing good long-term stability and reliability. For that operation the set-up of the transmitter was modified as it is shown on Fig. 6.3.

Comparing to the laboratory set-up (see Fig. 5.28), the ring resonator was folded into more compact design for a better mechanical rigidity and to obtain a ~0° incident angle of the cavity mode at the light resonator mirror glued on the HVPA. This reduces the misalignment of the cavity, deploying the feed-back loop. A real-time monitoring of the features of the output beam was applied: a leak of the pulse energy through one of the HR-mirrors was split 50% to a CCD-camera to check the shape and position of the beam and another 50% were directed to a plane Fabry-Perot interferometer (FPI) followed with a line CCD-array to observe a Fizeau pattern of the emission and verify the single longitudinal-mode operation of the TISA laser.

To confirm stable and durable operation of the transmitter in the environment with increased dust concentration and significant temperature and humidity variations, the maximum pump power was reduced to 32 W with corresponding reduction of the transmitter output down to 4 W. During the last IOPs in the end of August, the power of the TISA laser was increased up to 5 W. For examples of the water-vapor measurements see Subsection 6.2.3.
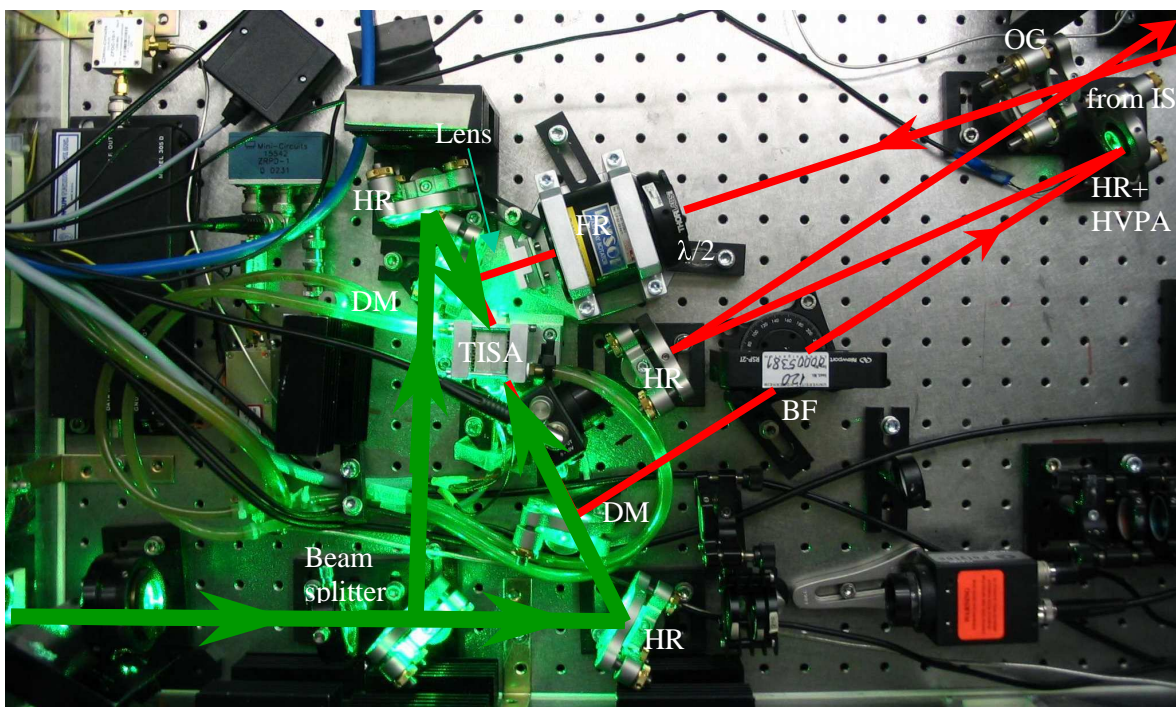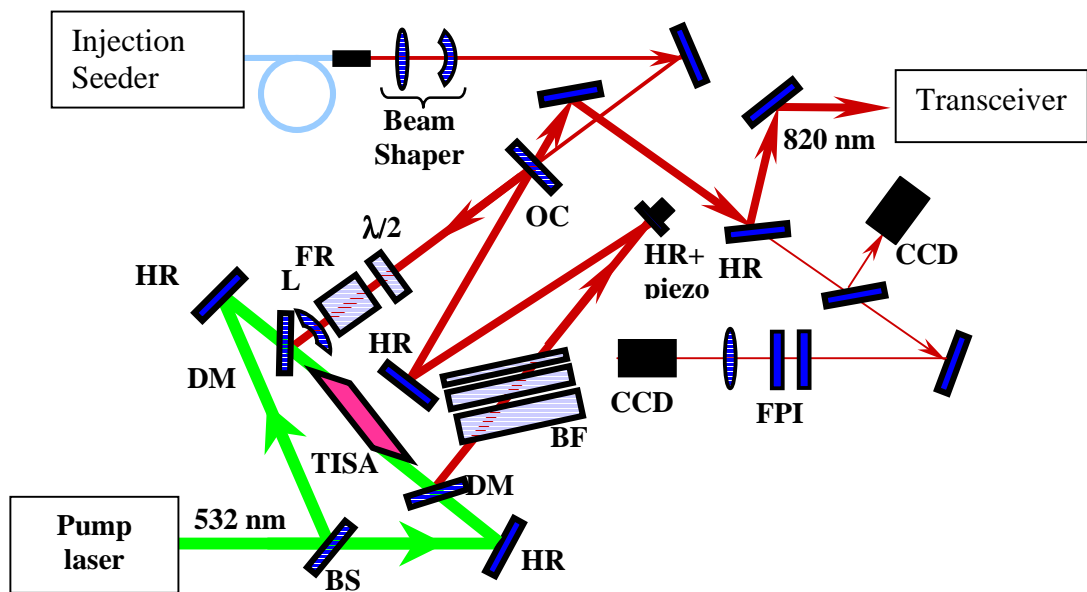
Fig.6.3 Scheme of the set-up of the TISA laser at 820 nm and photo of the TISA cavity during COPS. Here beam splitter (BS), high-reflective mirrors (HR), dichroic mirrors (DM), output coupler (OC), Faraday rotator (FR), birefringent filter (BF), Fabry-Perot interferometer (FPI), halfwave plate (λ/2), HR mirror, glued on a piezo actuator (HR+HVPA).

$$\sigma_r = \sqrt{\sigma_x^2 + \sigma_y^2} = 54\,\mu m$$
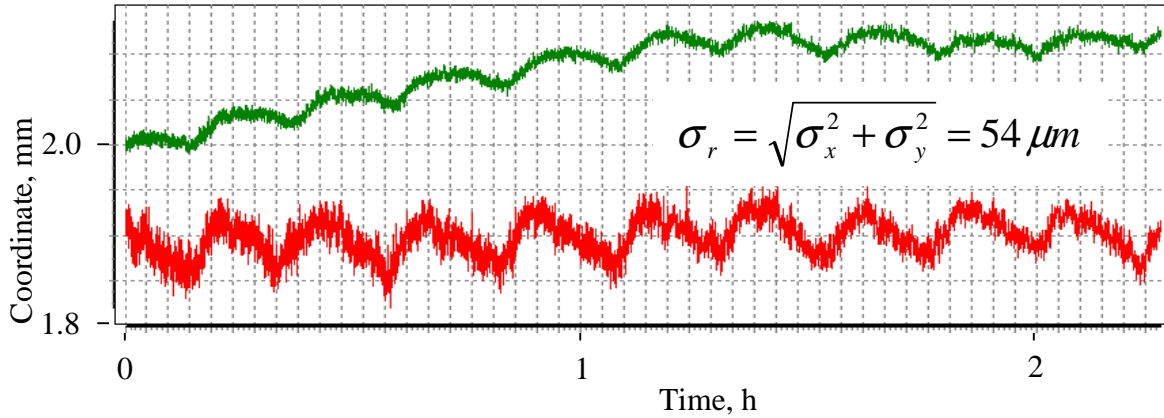
Fig.6.4 Trend of the beam pointing of the TISA laser recorded in the DIAL trailer for horizontal (red) and vertical (green) components. Recorded with a CCD-camera 2.5 m away from the OC of the TISA.

Another peculiarity of the in-field operation was a higher spatial and power instability of the transmitter properties. On the Fig. 6.4, a 2.5 hour trend of the TISA beam position is depicted, separately in horizontal (red) and vertical (green) planes. The slow drift of 0.1 mm in horizontal direction was expected from laboratory experiments, the reasons for this effect were already discussed in Subsection 3.3.2. But the faster drift with a period of approx. 15 minutes was never observed before. It was found, that most likely these fluctuations are caused by temperature variation in the trailer. The feed-back of the climate system with power ≈ 20 kW is by far too slow for an accurate temperature control. This results in temperature cycles with an amplitude of up to 5°C. The drift of the pump beam in the TISA crystal led both to corresponding drift of the lasing direction and the resonator misalignment with $\approx 10\%$ output power fluctuation.

The standard deviation of the given series is $\sigma_r = \sqrt{\sigma_x^2 + \sigma_y^2} = 54$ μm, which gives on a distance of 2.5 m the angular standard deviation of 22 μrad. After enlargement in the first beam expander with magnification 5, the angular deviation of the beam is reduced to 4.4 μrad 1σ, matching the requirement of the maximum allowed jitter of 15 μrad 1σ (see Table 2.1).

Operating the DLR IS, several problems were revealed. The ultra-fast switch was detuned, yielding a cross-talk of -20 dB instead of the specified –65 dB. The high leak of the 'offline' seeding emission in the 'online' channel was destroying the spectral purity of the transmitter. It was decided to operate only the 'online' IS and treat the non-seeded output of the transmitter for the 'offline' signal. For the operation in this mode, electronic circuit of the PDH feed-back loop was accomplished with the input gate, as it was described in the Subsection 4.2.2.

The emission of the diode lasers in the IS suffered severe frequency jitter and narrow mode-hop-free zone, caused by instable environment in the trailer. Furthermore, absence of optical isolators in ECDL layouts between the laser chip and the fiber coupler induced additional negative impact on the spectral stability of the IS. A long-term thermal drift of the diode lasers caused regular mode-hops in its emission.

This spectral instability influenced the emission of the slave laser, disturbing its single-frequency operation. To improve the spectral properties of the diode lasers the IS was running continuously, minimizing temperature drift in the laser chips. The spectrum of the TISA laser was monitored in a real time for immediate defining a deviation from a single-frequency operation.

6.2.3 Measurement results

Within 31 days of intensive observation more than 300 hours of data were stored. As an example, a 1.5 hour plot of vertical atmosphere profiling on the 1st of August 2007 (IOP 13a) is presented. Figures 6.5 (left and middle) show range-square corrected backscattered signal intensity from the far-field channel for 'offline' and 'online' wavelength respectively. Spatial resolution – 15 m, time average – 1 s. Figure 6.5 (right) depicts water-vapor mixing ratio distribution in the atmosphere calculated from the given data; the temporal resolution was decreased to 10 s for a better SNR. Using a 10-point derivation method, the result is affected by additional 150 m gliding-window averaging. The plot is merged from two of the far- and near-field channel, temperature information to calculate the mixing ratio from the number density data was obtained with a radiosonde launched that time from the Hornisgrinde.

Careful study of the plot emphasizes the details not visible on the initially measured atmosphere backscatter fields for 'online' and 'offline'. First, it is a dry layer with a water-vapor mixing ratio (MR) of 0.1-0.2 g/kg from 800 to 1100 m AGL, covering a humid convective boundary layer with MR of ~7 g/kg and followed by a relatively moist zone with MR of 3-4 g/kg. Aerosol backscatter shows a contrast between the layers of only 1 to 5. Also, a thin cloud around 3000 m AGL, obviously seen on the backscatter plot, is likely to consist of a dry dust due to corresponding dark zone on the MR plot. Validation of the DIAL measurements was performed using information of the water-vapor mixing ratio from the aforementioned radiosonde (see Fig. 6.6).

Figure 6.7 presents a 17-hour trend of the development of a warm moist air mass with embedded Saharan dust in the boundary layer and its following interaction with forced convection, recorded on 1-2 August 2007 (IOP 13 a/b). The presented water-vapor mixing ratio field has the same resolution as on the Fig. 6.6 (right).

During the observation period the troposphere stayed stable preserving a stratified structure (see Fig.6.7): a humid convective boundary layer with the values of MR up to 10 g/kg is covered with a dry layer of constant temperature and thickness around 400 to 500 m. Above the latter, a relatively moist zone with a mixing ratio of 3-4 g/kg is located. Between 0845 and 1800 UTC the top border of the convection zone raises from 500 to 800 m AGL, lifting also a cold 'cap'. After 1800 UTC, a warm moist-dry layered air mass is advected from west in the lower free troposphere above the lidar site. Wind speed was increasing and reached ≈ 12 m/s near 500 m AGL at 2300 UTC. An appearance of a strong outflow boundary, produced by the mesoscale convective system around 0120 UTC, is shown by a sudden rise of the moist layer at this time. The end of the measurement period at 0240 UTC was caused by oncoming precipitations. A larger vertical covering from 2130 till 0145 UTC is due to a better alignment of the near-field telescope.

This and other measurement examples, also in synergy with a scanning temperature Raman lidar [Radlach et al., 2008] and wind Doppler lidar [Wieser, 2005], can be found in [Pal et al., 2008].
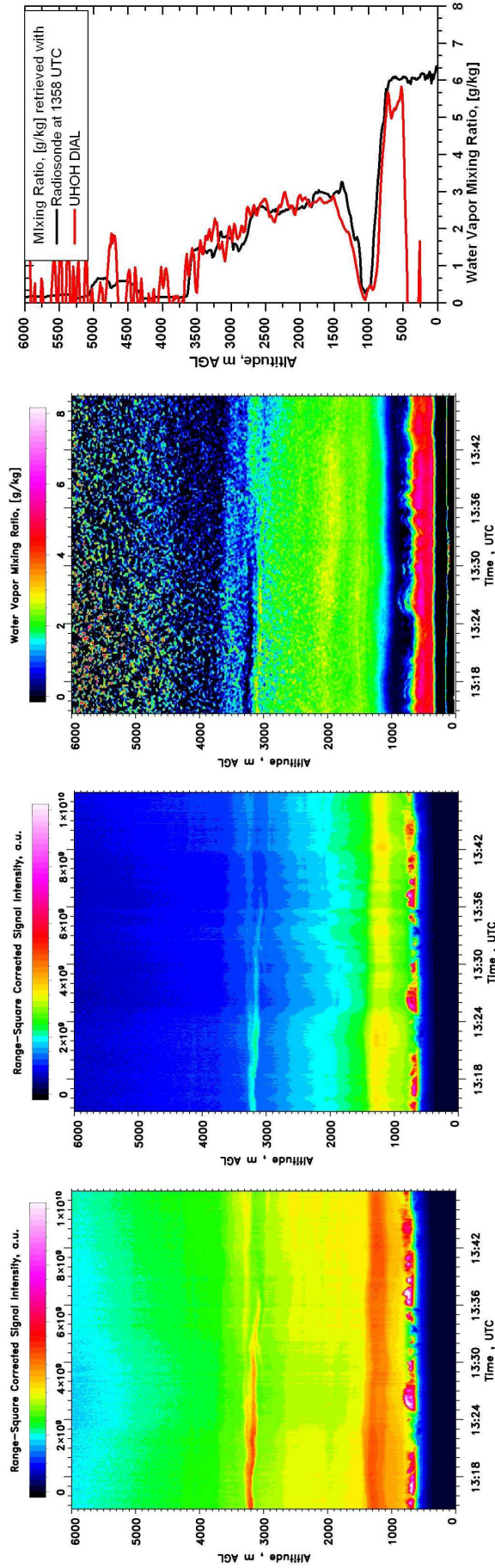
Fig.6.5 Time-height cross-section of the range-square corrected signal intensity, offline (left), range-square corrected signal intensity, online (middle) and water-vapor mixing ratio, g/kg (right), obtained during measurements on 1-2 August 2007 (IOP 13a/b) [Behrendt et al., 2008]. The time and range resolutions of the backscattered signal are 1 s and 15 m, respectively; for the water-vapor distribution these amount to 10 s and 15 m with an additional 150 m gliding window average. The data coverage of last starts from a height of 300 m because of included data from a near-field 20-cm telescope.

Fig.6.6 Intercomparison of the water-vapor mixing ratio data, measured with UHOH DIAL and radiosonde on 1st August 2007 (IOP 13a).

117
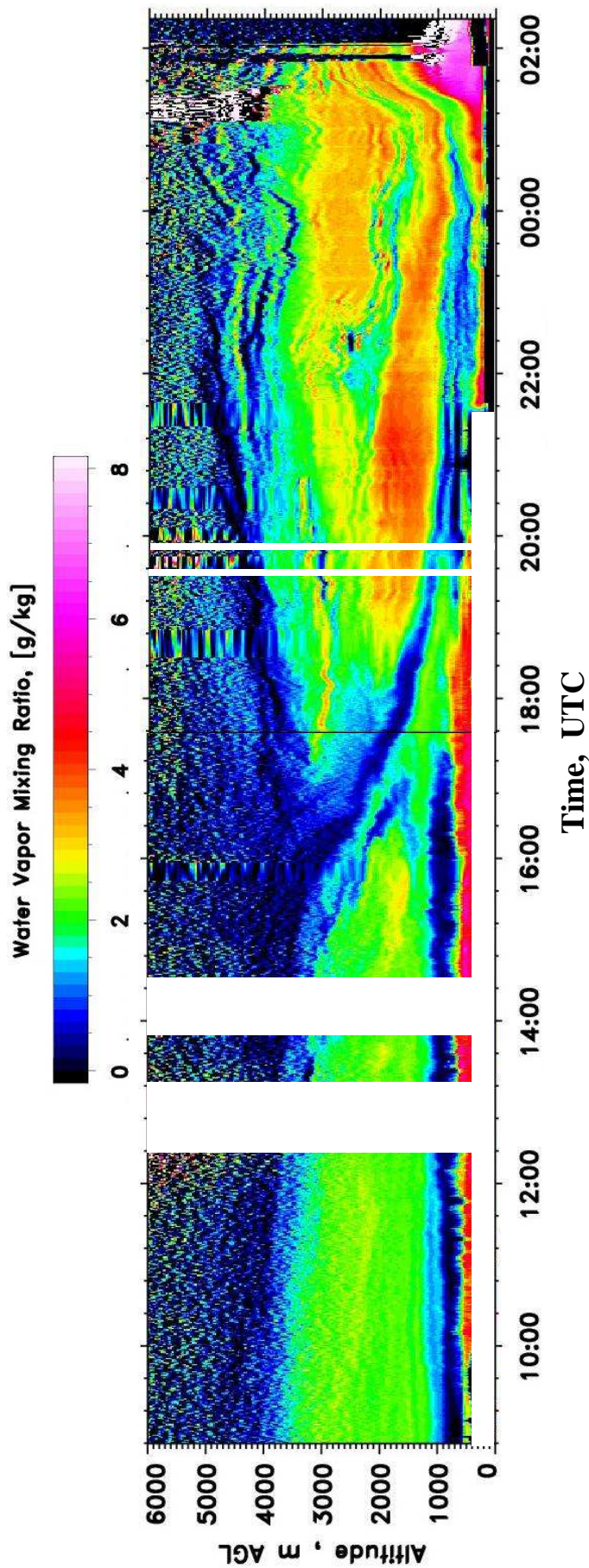
Fig.6.7 Time-height cross-section of the water-vapor mixing ratio obtained with UHOH DIAL from 1st August 0930 UTC until 2nd August 0220 UTC from the top of Hornisgrinde, Black Forest [Pal et al., 2008]. Note that an out flow boundary passed over the lidar site around 0112 UTC on 2nd August 2007. Time resolution is 10 s, range resolutions is 15 m (with 150 m gliding average). No Reyleigh-Doppler correction was performed for the measured data. From 2130 UTC onwards, the bottom height of the data collected is lower because of the better alignment of a near-range telescope. Vertical and horizontal white bands on the figure are due to gaps in measurement and incomplete overlap, respectively.

Chapter 7

Summary and outlook

7.1 Summary

The laser developed within the scope of this thesis shows to my knowledge the highest average output power demonstrated yet by a single-rod single-frequency TISA laser at 820 nm as well as at 935 nm. The transmitter fulfills the requirements for accurate, high temporally- and spatially-resolved measurements of atmospheric water vapor deploying the DIAL technique. The following main achievements have to be mentioned regarding this work.

7.1.1 Pump laser

Designing and assembling of the pump laser in the IB Laser (Berlin) was participated. Appling the pre-measured strength of the thermal lenses in pump chambers of the master-oscillator and the amplifiers, the complete optical layout of the pump laser was simulated in ZEMAX. The construction was optimized with respect to a symmetrical propagation of the eigenmode through the amplifiers. Together with Artur Napiwotzky (IB Laser), the optical components were assembled into the laser set-up piece-by-piece with an intermediate control of the beam parameters. When the measurement showed a principal difference from the simulation, the model have been adopted accordingly, optimization of the layout have been repeated, and the modification have been introduced in the set-up.

After the system was assembled, it was thoroughly controlled for matching the requirements of the pump laser in the water-vapor DIAL transmitter.

Later a routine maintenance of the laser was performed, including alignment control after each transportation of the trailer, incorporation detectors and CCD cameras to monitor the pulse shape and beam position. For repayment procedures some components were replaced, namely quaterwave plate in the master oscillator, whole pump chambers as well as Nd:YAG rods only,

SHG crystals etc., with the following realignment of the system and new specification of its characteristics.

7.1.2 Injection seeder

For the laboratory experiments, the IS on the base of the Toptica DL100 ECDL was designed, specified and deployed. The ECDL was several times realigned due to replacements of the laser diode after its optical damage or when the IS was retuned from 935 nm to 820 nm region.

To optimize the operation of the IS made at the DLR Oberpfaffenhofen, some minor changes in the LabView driving program were introduced. The ultra-fast optical switch was replaced because of its damage.

7.1.3 Ti:sapphire transmitter

Design of the TISA transmitter was the most time- and efforts-consuming part of the work. Construction of the clamp-shells from NCAR was modified for another rod size and the TISA-crystal was clamped in the heat sink. The focal lengths of the optically-induced thermal lens in the Brewster-cut TISA crystal were measured for different levels of the pump power. The ring resonator was calculated with respect to dynamical stability of the eigenmode and its minimum size along the resonator.

Transmission and reflection spectrums of the intra-cavity elements, namely resonator mirrors, lenses and birefringent filters, were optimized regarding operation of the transmitter either at 935 nm or 820 nm. Spectrums of the small-signal round-trip amplification in the resonator were estimated for both designs.

The laser layouts for operation at 935 nm and 820 nm were assembled and specified for matching the requirements of the transmitter of the airborne and ground-based water-vapor DIAL system, respectively. Both systems demonstrated single-frequency operation with a near-Gaussian beam profile and the highest average power so far.

7.1.4 Differential absorption lidar

The TISA laser optimized for 820-nm operation was incorporated into the mobile platform of the water-vapor DIAL system and participated the measurement campaign COPS in summer 2007. The system was working for 3 months, including 31 days of intensive observations. More than 300 hours of high spatially- and temporally resolved day- and nighttime measurements were acquired. Comparison of the preliminary processed water-vapor data with information from the *in-situ* sensors (radiosonde) confirmed a low bias of the measured values.

7.2 Outlook

7.2.1 Modernization of the current system

Although the TISA laser transmitter fulfills the requirements for an accurate water-vapor profiling of the atmosphere, its in-field operation revealed several weaknesses of the system. There are certain activities planned to solve the discovered engineering problems.

In a first hand, the warm-up time of the pump laser has to be reduced and the spatial drift of its beam during operation has to be minimized. This will improve pointing- and energy stability of the TISA laser, preserving high conversion efficiency.

The pump laser has to be modified regarding the options discussed in Subsection 3.4: either modernization of the MO to the 2-chamber layout or applying of an active beam-direction control has to be performed. An active temperature control of components of the MO, e.g. the Q-switch, will improve the stability of the laser emission in the environment with remarkable temperature fluctuations.

For a better spatial overlap between the pump beam and the eigenmode of the TISA laser, the pump beam cross-section of the optimum size with a better energy distribution has to be imaged in the rod plane. The beam shaper has to be modified from a Galileo- to a Kepler-scheme (with two positive lenses). Deployment of a vacuum cell with Brewster-windows between the lenses is required to prevent ionization of air and severe energy scattering in the focus of the first lens.

The operation of the DLR IS in the trailer is affected by the low response time of the computer-based feedback loop and thermal drift of the laser diodes. When mechanical noise and temperature fluctuations of the environment cannot be eliminated, another stabilization technique has to be applied. The external-cavity diode lasers have to be replaced with lasers with distributed feedback.

Using of the optical chopper in the detector unit distorts functionality of the stabilization scheme of the TISA laser and blocks the backscattered signal from the first 3 km of the atmospheric profile. To avoid deployment of the chopper for the scanning, the DIAL system has to be modified to a bi-axial configuration.

A new set-up of transmission optics is currently under the test. The TISA laser output is coupled in a high-power multi-mode fiber and delivered to a collimator, fixed on the scanning telescope. A 20-cm off-axis parabolic mirror was implemented to collimate the fiber output with a residual divergence of < 0.6 mrad. To fold a 75-cm focal distance, a flat bending mirror with aperture of

10 cm was applied. The collimator was designed with respect to 50 K temperature variation and a high mechanical stiffness of the construction. Among other advantages, this layout allows for increasing the transmission of the laser pulse through the transceiver optics in the atmosphere from the current $\approx$ 30% to $\approx$ 60%.

The last major modification of the DIAL concerns the climate system in the trailer. When the trailer environment will be free from the temperature fluctuations and mechanical vibrations, passive stability of the transmitter and IS characteristics will be significantly improved. The possible solutions are currently under discussion.

7.2.2 Upgrade of the transmitter

It is planned to upgrade the pump laser to the 200 W average power output at 532 nm. The TISA laser has to be upgraded correspondingly to handle this power level and obtain its effective conversion into a single-frequency IR emission with a low M^2 parameter.

The maximum pump and output energies of the transmitter utilizing a TISA laser with a single-crystal stable resonator are limited due to the low optical damage threshold of the TISA at the pulse repetition rate of 250 Hz. For a TISA rod length of 2 cm, cavity lengths from 130 to 160 cm and an overlap of > 90%, the maximum pump pulse energy has to be confined to 88 mJ, yielding a maximum energy extraction efficiency of ~90% (see Fig.A.2).

For operations with the same pulse rate at higher pulse energy, the size of the cavity mode has to be increased to preserve the maximum energy density on the optical elements. This can be achieved switching the layout from the stable to an unstable resonator [Wagner, 2009]. The corresponding theoretical study was performed and the layout was built to specify the energy, spatial and spectral parameters of the laser.

However, a shorter cavity length of the unstable resonator may cause a reduction of the pulse build-up time and corresponding decrease of the damage threshold. The maximum pump power of the single laser crystal has to be considered as well. A TISA crystal with a length of 20 mm and diameter of 7 mm mounted in the clamp-shells (see Subsection 5.2.1) can effectively handle pump powers up to 50 W. For a higher power levels a 2-crystal resonator has to be preferred. To work with the pump power of > 100 W, it is required to rebuild the TISA laser in a MOPA (master oscillator – power amplifier) configuration. For the amplifiers two TISA crystals with undoped end-caps with diameters of 7 mm and total lengths of 40 mm are available.

Appendix A

Laser pulse evolution model

A model of the laser operation based on the principle of balance of the particle number on energy levels of the activator and completed with the energy balance of the photon flow is useful to describe energy and temporal properties of the laser emission. Different to e.g., [Koechner, 1999] description approach is presented, pretending to be more self-understanding [Пахомов, 1986]. For the set of differential equations an approximated analytical and a numerical solution is given. The effect of spontaneous depopulation of the upper laser level in the TISA was found essential for a better understanding of the operation principles of the TISA laser.

A.1 Balance equations

In general, the variation speed of the population on the ith energy level of the laser material can be characterized as:

$$
\frac{\mathrm{d}n_i}{\mathrm{d}t} = \sum_{j \neq i} W_{ji} n_j + \sum_{j > i} A_{ji} n_j + \sum_{j > i} d_{ji} n_j - \sum_{j \neq i} W_{ij} n_i - \sum_{j < i} A_{ij} n_i - \sum_{j < i} d_{ij} n_i
$$
$$
\sum_i n_i = N = const
$$

(A.1)

where n_j – number density of atoms on the jth energy level, $j \neq i$; A_{ji}, A_{ij} – probability of spontaneous transitions to/from the ith level; W_{ji}, W_{ij} – probability of stimulated transitions to/from the ith level, proportional to the intensity of propagating radiation with a single photon energy $h\nu = |E_i - E_j|$; d_{ji}, d_{ij} – probability of non-radiative transitions to/from the ith level.

The TISA can be treated as a four-level active medium (see Fig. 5.1); the laser operates in a quasi Q-switch mode (so called 'gain switching'). The populations of the upper level n_3 and the lower laser level n_1 can be neglected due to its fast decay to the upper laser level and to the

ground state, respectively, hence, $n_1 = n_3 \approx 0$ and $N = n_0 + n_2$. In the present system the pump pulse length is ≈ 20 ns, so that the pump laser activity during the TISA pulse build-up time can be neglected and the pump pulse temporal shape can be approximated with a delta-function $\delta(t = 0)$. Thus, the model of the active medium with the laser emission propagating along the z-axes with the pump pulse absorbed, is described with the following equation for inversion population of laser level, completed with the photon flow relation:

$$\frac{d(\Delta n(t,z))}{dt} \approx \frac{dn_2(t,z)}{dt} = -\phi(t,z,\nu)\sigma(\nu)n_2(t,z) - \frac{n_2(t,z)}{\tau},$$

$$\frac{\delta\phi(t,z,\nu)}{\delta z} + \frac{1}{\upsilon}\frac{\delta\phi(t,z,\nu)}{\delta t} = \phi(t,z)[\sigma(\nu)\Delta n(t,z) - \beta(\nu,z)], \tag{A.2}$$

where $\phi(t,z,\nu)$ – photon flow density, $\sigma(\nu)$ – gain cross-section, $\beta(\nu,z)$ – losses in the active medium, τ – relaxation time of the upper laser level, $\upsilon = c/n_c$ – speed of the EM-wave propagation in the medium with n_c here – refraction index of the crystal. Introducing the gain coefficient $g(t,z,\nu) = \sigma(\nu)\Delta n(t,z)$ and the saturation energy density $Q(\nu) = \frac{h\nu}{\sigma(\nu)}$, the Eq. A.2 can be written finally as

$$\frac{dg(t,z,\nu)}{dt} = -I(t,z,\nu)\frac{g(t,z,\nu)}{Q(\nu)} - \frac{g(t,z,\nu)}{\tau}, \tag{A.3}$$

$$\frac{\delta I(t,z,\nu)}{\delta z} + \frac{1}{\upsilon}\frac{\delta I(t,z,\nu)}{\delta t} = I(t,z,\nu)[g(t,z,\nu) - \beta(\nu,z)], \tag{A.4}$$

with $I(t,z,\nu) = h\nu\,\phi(t,z,\nu)$ – radiation intensity. For the unidirectional ring resonator with cavity length L equal to the active medium size l, the following start and boundary conditions are valid:

$$I(t = 0) = I_0,$$

$$g(t = 0) = g_0(z,\nu) = \sigma(\nu)\frac{E_{st}(z)}{h\nu_p V_{am}}, \tag{A.5}$$

$$I(z = 0) = R \cdot I(z = l),$$

where R – reflectivity of the output coupler, E_{st} – energy stored on the upper laser level within a volume of the intra-cavity mode, $V_{am} = Sl$ – volume of the intra-cavity mode, $h\nu_p$ – energy of a photon of the pump emission. The Eqs. A.3-A.5 are insensitive for the profiles of the pump beam and the cavity mode. The flat-top profile of the pump beam is assumed. The overlap of the beams is treated optimal when the pump beam radius is equal to one of the eigenmode, measured at the level $1/e^2$ from the peak energy.

A.2 Coordinate-independent approximation

The general solution of the equation set Eq. A.3-A.5 can be derived only numerically. To derive an analytical solution for estimation of the output energy, the pulse length and the pulse build-up time, a "point-resonator" model was deployed with the following assumptions [e.g., Koechner, 1999]:

- *I* and *g* do not depend on the coordinate and may be replaced by their spatial-averaged

  values $\bar{I}(t) = \frac{1}{l}\int_0^l I(t,z)dz$ and $\bar{g}(t) = \frac{1}{l}\int_0^l g(t,z)dz$. The real distribution of the intensity

  and the gain over the active medium is far from homogeneous, and this assumption may cause some uncertainties;

- the intra-cavity losses, passive and for out-coupling, are all concentrated in the crystal. The amount of uncertainty induced by this approximation depends on the cavity configuration;

- the spectrum of the laser emission is narrow-band around frequency ν_0 and the gain cross-section can be approximated as $\sigma(\nu_0) = const = \sigma$. For the TISA with a gain bandwidth of ~300 nm the value of the cross-section within several nanometers, pre-selected with the coarse spectral narrowing of the birefringent filter (see Subsection 4.1), may be accepted constant with a negligible error. The modeling shows a good fit to the experiment (comparable with a measurement uncertainty), when for a gain peak the value $\sigma = 2.7*10^{-19}$ cm^2 @ 800 nm is applied [Moulton, 1986].

These assumptions lead to a resonator of negligible length equal to the length of the laser crystal.

To complete the model, resonator losses shall be included. The spatially averaged intensity after a single pass through the laser crystal grows as $\bar{I}(t>0) = \bar{I}_0 \exp[(\bar{g}(t) - \beta_{ae})l]$, which is a Lambert' law. Hence, an amplification of the intra-cavity field intensity after a round-trip in a ring cavity is

$$\tilde{G}(t) = \frac{\bar{I}_0 \exp[(\bar{g}(t) - \beta_{ae})l]R\prod_i(1-\gamma_i)}{\bar{I}_0} = \exp[(\bar{g}(t) - \beta_{am})l]R\prod_i(1-\gamma_i), \tag{A.6}$$

where $\bar{I}_0$ – intensity at the starting point of the round-trip, γ_i – intra-cavity losses: γ_R – absorption in optical elements and leak through HR-mirrors, γ_{dif} – diffraction losses, γ_{mis} – losses

on misalignment. Introducing coefficients $\beta_i = \frac{1}{l}\ln\left[\frac{1}{1-\gamma_i}\right]$ and $\beta_{out} = \frac{1}{l}\ln\left[\frac{1}{R}\right]$, Eq. A.6 can be written as

$$\tilde{G}(t) = \exp[(\overline{g}(t) - (\beta_{am} + \sum_i \beta_i + \beta_{out}))l] = \exp[(\overline{g}(t) - (\beta_{loss} + \beta_{out}))l] =$$
$$= \exp[(\overline{g}(t) - \beta_\Sigma)l] \tag{A.7}$$

where β_{loss} – dissipative losses in the resonator, β_{out} – coupling losses of the resonator, β_Σ – total losses. From this formula, lasing is possible when $\tilde{G} > 1$ and $\overline{g} > \beta_\Sigma$.

The pulse evolution model with the given approximations is intended to simulate the seeded operation of the laser. It can be implemented for a model of the free-running mode of the TISA laser as well, when a BF obtains coarse spectral narrowing and constrains the emission spectrum to a few nanometers. However, such a simulation does not concern the multimode nature of the not-seeded lasing and may cause a high result uncertainty.

The laser pulse in the free-running mode develops from the noise emission with a power $P_{spon}(t=0) = \frac{\overline{g}_0 lSQ}{\tau}$. The energy scatters in all directions homogeneously and only the photons reaching the crystal after a round-trip in the cavity will contribute the pulse evolution. Thus the intensity of the 'natural seed' is attenuated with a spatial factor of $\eta_S = \frac{1}{4\pi L^2}$.

The noise photons are emitted over the whole spectrum of the TISA with random polarization and only those enjoying the round-trip amplification $\tilde{G} > 1$ will impact the build-up of the laser pulse (see Eq. A.7). Spectral η_ν and polarization dependant η_{pol} components of the efficiency of the spontaneous emission can be distinguished. Spectral efficiency is a ratio of a spectrum fraction of the TISA small-signal gain with $\overline{g}(t=0,\nu) > \beta_\Sigma(\nu)$ to the total emission spectrum. Here $\beta_\Sigma(\nu) = \beta(\nu) + \beta$ – intra-cavity losses, consisting of the spectrally dependant part (transmission of the BF, reflectivity of the HR-mirrors and OC), – and spectrally independent part (losses for resonator misalignment, energy scattering on optics etc.). Polarization efficiency depends on the intra-cavity gain: whereas near the lasing threshold only photons with *p*-polarization have $\tilde{G} > 1$, at a higher pump energies fraction of the *s*-polarized photons increases.

Hence, concerning cavity losses and the difference in lengths of the resonator and the active medium, Eq. A.3, A.4 and A.5 can be rewritten as

$$\frac{d\overline{g}(t)}{dt} = -\overline{I}(t)\frac{\overline{g}(t)}{Q} - \frac{\overline{g}(t)}{\tau},$$

$$\frac{d\overline{I}(t)}{dt} = \overline{I}(t)\frac{\upsilon}{\chi}\left[\overline{g}(t) - \beta_{\Sigma}\right]$$

(A.7)

$$\overline{g}(t=0) = \sigma\frac{E_p}{h\nu_p V_{am}}\eta_p,$$

$$\overline{I}(t=0) = I_0 = \begin{cases} \overline{I}_{noise} = \dfrac{\overline{g}_0 lSQ}{\tau}\dfrac{1}{4\pi L^2}\eta_v\eta_{pol}, & \text{without IS} \\[3mm] \overline{I}_{IS} = \dfrac{P_{IS}}{S}\dfrac{1-R}{1-R(1-B)}\eta_{IS}, & \text{with IS} \end{cases}$$

(A.8)

with $\chi = \dfrac{L+n_c l}{n_c l}$ specifies the filling ratio of the cavity with the length L and the crystal of the

optical length $n_c l$, E_p – single-pulse pump energy approaching the laser crystal, $\eta_p = \eta_q\eta_o\eta_a$ – pump efficiency. Here η_q quantum efficiency of the transition from the ground-state to the upper laser level. For the pump wavelength of 532 nm $\eta_q \approx 1$. η_o is an overlap between the pump beam

w_p and the cavity mode w_c in the crystal. For Gaussian beams $\eta_o = 4\dfrac{w_p^2 w_c^2}{(w_p^2 + w_c^2)^2}$; for non-

Gaussian beams with energy distributions in their beam cross-sections described with normalized

functions $I_1(x,y)$ and $I_2(x,y)$, the overlap can be derived as $\eta_o = \left(\iint\limits_S \sqrt{I_1 I_2}\,dxdy\right)^2$. η_a is the

absorption of the pump energy in the crystal.

The intensity I_{IS} of the seeding emission is calculated for the steady-state condition, when the gain is absent and the energy losses, dissipative and for the out-coupling, are compensated with the seeded beam, yielding a unit round-trip amplification $\widetilde{G} = 1$. P_{IS} – power of the cw-IS before coupling in the cavity, η_{IS} – coupling efficiency of the injected photons in the resonator mode.

Averaging of the intensity and the gain over the crystal may cause a severe uncertainty of the result. To estimate the reliability of the model, the relative difference of energy intensities on the exit of the crystal and an average one was calculated. When intra-cavity field intensity is on its maximum and the gain coefficient is depleted to the threshold level $\overline{g} = \beta_{\Sigma}$, the relative error is

$$\delta = \frac{I(z=l) - \overline{I}}{I(z=l)} = \frac{1 - R + \ln(R)}{\ln(R)}$$

(A.9)
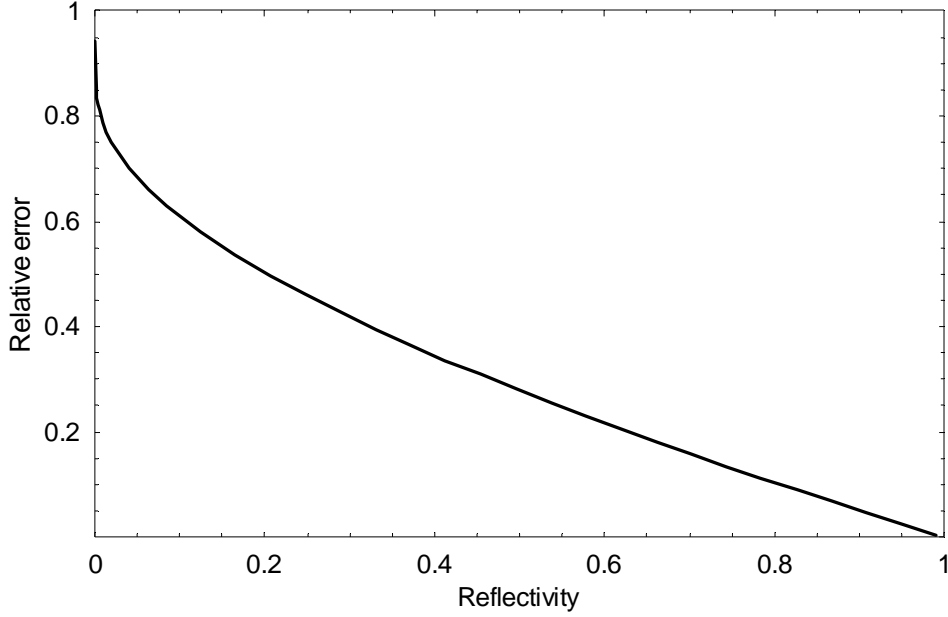
Fig.A.1 Estimated relative error of the point-resonator model vs. reflectivity of the OC.

The plot for $\delta(R)$ is depicted on the Fig.A.1. For the $R > 50\%$ relative error does not exceed 30%, which is acceptable for engineer calculations. It is necessary to mention that for a linear resonator such an error for $R > 50\%$ is less than 6% [Пахомов, 1982].

A.3 Output energy and temporal properties of the pulse

Solving analytically Eq. A.7 together with boundary and initial conditions Eq.A.8, it is usually assumed that the spontaneous depopulation of the upper laser level may be neglected for the times of evolution of the laser pulse:

$$\frac{d\overline{g}(t)}{dt} = -\overline{I}(t)\frac{\overline{g}(t)}{Q}, \tag{A.10}$$

Hence, the following analytical solutions in this approximation were derived [Пахомов, 1982]

for the output energy

$$E = QV_{am}\beta_{out}(X + 0.2 - \frac{1.2}{X}), \tag{A.11}$$

for the peak power

$$P_{peak} = QV_{am}\frac{\upsilon}{\chi}\beta_{out}\beta_{\Sigma}(X - 1 - \ln X) \tag{A.12}$$

128

A.3 Output energy and temporal properties of the pulse
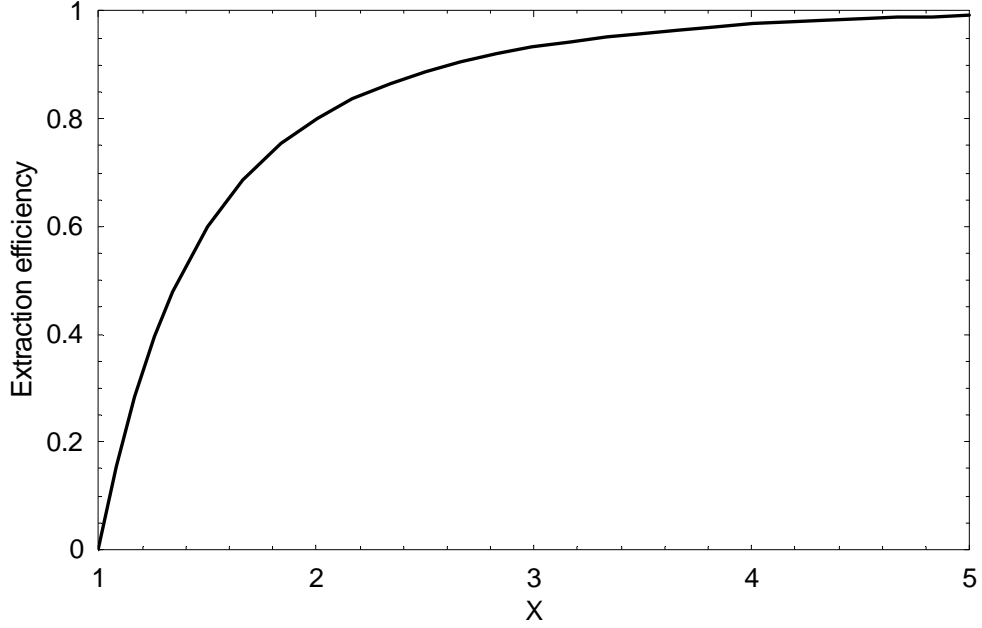

Fig.A.2 Extraction efficiency of the stored energy regarding ratio $X = \dfrac{g_0}{\beta_\Sigma}$, representing an exceeding of the small-signal gain over the total losses (see also [Siegman, 1986, p.1015]).

for the pulse build-up time

$$t_{bu} = \frac{\chi}{\upsilon(\bar{g}_0 - \beta_\Sigma)} \ln\left[\frac{Q\upsilon(\bar{g}_0 - \beta_\Sigma)}{10\bar{I}_0\chi} + 1\right],$$

(A.13)

for the pulse length

$$t \approx \frac{E}{P_{peak}} = \frac{1}{\beta_\Sigma}\frac{\chi}{\vartheta}\frac{\left(X + 0.2 - \dfrac{1.2}{X}\right)}{X - 1 - \ln X}$$

(A.14)

where $X = \dfrac{\bar{g}_0}{\beta_\Sigma}$ – ratio of the small-signal gain coefficient to the total losses in the cavity. For further calculations of the pulse build-up time of the TISA, it is assumed all injected photons fit one of the longitudinal modes of the resonator.

Deriving the Eq.A.11 for the output energy, a relation between an extraction efficiency of the stored energy in a pulse and the gain-to-losses ratio X may be depicted (see Fig. A.2). For $X = 5$, more than 99% is extracted, though the acceptable efficiency of $> 93\%$ is achieved already for the $X = 3$. The extracted energy is coupled out as well as contributes the passive losses.
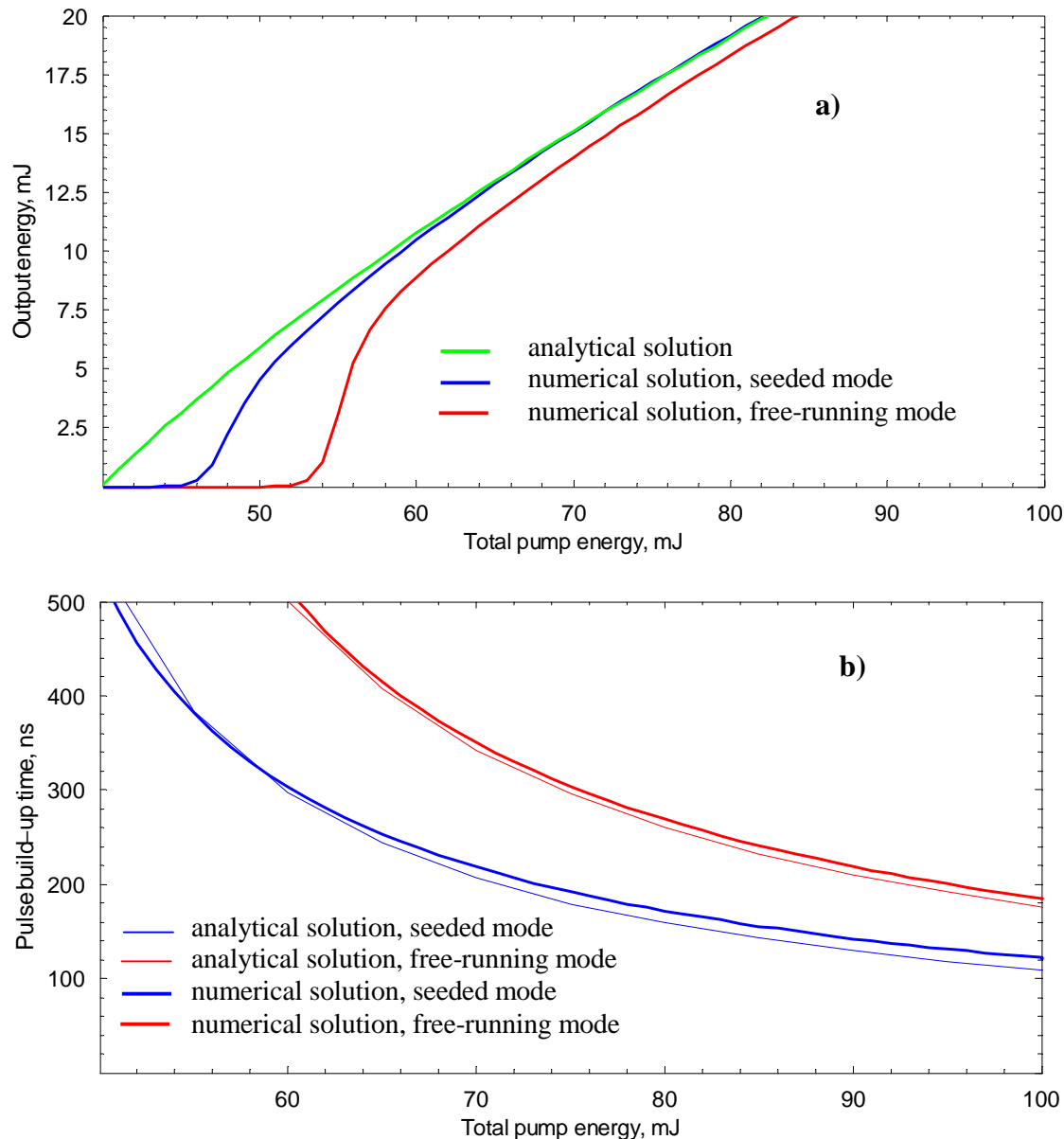
Fig.A.3 Estimated slope efficiency (a) and pulse build-up time (b) of the TISA laser, derived using analytical and numerical solutions of the rate-equation model. Here wavelength 935 nm and the corresponding gain cross-section of $\sigma(935) = 1.35*10^{-19}$ cm^2, eigenmode radius on the crystal $w_c = 0.65$ mm, pump coupling efficiency 77%, reflectivity of the OC R = 72%, injection seeder power 15 mW. The level of passive losses is 13% and 8% for the simplified and for the numerical calculation, respectively.

Equation A.11 shows that the energy extracted from the laser crystal in a single pulse does not depend on the strength of the initial field and is the same for the seeded as well as for the not seeded modes. However, this equation does not represent the behavior of the TISA laser adequately: the experiment showed a remarkable difference of the output energy (5-10%)

between seeded and not seeded modes (see Figs.5.14, 5.29, 5.32). The explanation of this effect lies in a longer evolution time of the non-seeded pulse.

The minimum measured build-up time difference between the free-running mode and the seeded mode is 100 ns. For the relaxation time of the TISA of $\tau = 3.2$ µs [Moulton, 1986], this corresponds 3.5% depopulation of the upper laser level. Introducing this correction in the Eq.A.11, the estimated defect of the output energy is 7%.

Solving Eqs. A.7, A.8 numerically, more realistic solution was obtained. Figure A.3 (a) depicts the result of the simulation of the TISA performance using Eq. A.11 (green) and numerical solution for the seeded (blue) and free-running (red) modes. The initial conditions for the calculations were: wavelength 935 nm and the corresponding gain cross-section of $\sigma(935) = 1.35*10^{-19}$ cm^2, eigenmode radius on the crystal $w_c = 0.7$ mm, pump coupling efficiency 87%, reflectivity of the OC $R = 72\%$, power of the injection seeded 15 mW. The amount of passive losses was assumed of 13 % and 8 % for the analytical and numerical calculation, respectively. Comparing the pulse build-up times derived with analytical and numerical approaches, the same model outputs were achieved assuming the level of the passive losses of $B = 13\%$ for analytical and $B = 8\%$ for numerical solution (see Fig.A.3. b).

The discussed rate-equation model assumes a severe spatial simplification of the lasing processes in the resonator. However, comparison of simulations with experimental results showed a good coincidence with an uncertainty, comparable with a measurement error (see Fig. 5.14, 5.16, 5.29, 5.32).

References

ANSI, 1986: American National Standard Z136.1-1986: Safe Use of Lasers, *American National Standards Institute*, New York.

Ansmann A., 1985: Errors in ground-based water-vapor DIAL measurements due to Doppler-broadened Rayleigh backscattering, *Appl.Opt.*, **24**, 3476-3480

Barnes N. P. and Barnes J. C., 1993: Injection seeding I: Theory, *IEEE J. Quantum Electron.*, **29**(10), 2670-2683.

Barnes J. C., Barnes N. P., Wang L.G., Edwards W., 1993: Injection seeding II: Ti:Al2O3 Experiments. *IEEE J. Quantum Electron.*, **29**(10), 2684-2692.

Behrendt A., Wagner G., Petrova A., Shiler M., Pal S., Schaberl T., Wulfmeyer V., 2005: Modular lidar systems for high-resolution 4-dimensional measurements of water vapor, temperature, and aerosols, In *Lidar Remote Sensing for Industry and Environmental Monitoring V*. Edited by Singh, Upendra N.; Mizutani, Kohei. (Proceedings of the SPIE 5653), 220-227.

Behrendt A., Wulfmeyer V., Di Girolamo P., Kiemle C., Bauer H.-S., Schaberl T., Summa D., Whiteman D. N., Demoz B. B., Browell E. V., Ismail S., Ferrare R., Kooi S.,. Ehret G, Wang J., 2007a: Intercomparison of water vapor data measured with lidar during IHOP_2002, Part 1: Airborne to ground-based lidar systems and comparisons with chilled-mirror hygrometer radiosondes, *J. Atmos. Oceanic Technol.* **24** (1), 3-21.

Behrendt A., Wulfmeyer V., Kiemle C., Ehret G., Flamant C., Schaberl T., Bauer H.-S., Kooi S., Ismail S., Ferrare R., Browell E. V., Whiteman D. N., 2007b: Intercomparison of water vapor data measured with lidar during IHOP_2002, Part 2: Airborne to airborne systems, *J. Atmos. Oceanic Technol.* **24** (1), 22-39.

Behrendt A., Wulfmeyer V., Schiller M., Pal S., Riede A., Bauer H., Wagner G., Fix A., Wirth M., Ehret G., Wandinger U. and Althausen D., 2008: High-resolution water-vapor measurement

References

using a ground-based, mobile differential absorption lidar system, *88th Annual Meeting of the American Meteorological Society*, New Orleans.

Bevis M., Businger S., Herring T., Anthes R., Rocken C., Ware R., 1992: GPS Meteorology: Remote sensing of atmospheric water vapor using the Global Positioning System, *J. Geophys.Res.* **97**, 15787-15801.

BGV B2, 1997: Laserstrahlung, Empfehlung für die Verwendung von Laserschutzbrillen, http://www.bc-verlag.de/UVVen/93/ANH4A.HTM, Berufsgenossenschaft der Feinmechanik und Elektrotechnik, Köln

Black E.D., 2001: An introduction to Pound-Drewer-Hall laser frequency stabilization, *Am. J. Phys.,* **69**, 79-87

Born M., Wolf E., 1964: Principles of optics, *Pergamon Press*, Oxford

Bösenberg, J., 1998: Ground-based differential absorption lidar for water-vapor and temperature profiling. *Appl. Opt.,* **37,** 3845–3860.

Boyd, G. D. and Kleinman, D. A., 1968: Parametric Interaction of Focused Gaussian Light Beams, *J. of Appl. Phys.*, **39**, 3597-3639.

Bradley M.M., Fuelberg H.E. and Xiang X., 1994: Simulations of the Effects of Water Vapor, Cloud Liquid Water, and Ice on AMSU Moisture Channel Brightness Temperatures, *Appl. Meteorol*. **33**, 1133-1154.

Browell, E.V., Ismail S. , Hall W.M., Moore A.S. Jr., Kooi S.A., Brackett V.G., Clayton M.B., Barrick J.D.W., Schmidlin F.J., Higdon N.S., Melfi S.H. and Whiteman D.N., 1996: LASE validation experiment. Advances, In *Atmospheric Remote Sensing with lidar*, edited Ansmann A., Neuber R., Rairoux R. and Wandinger U., Spinger-Verlag, New York, Berlin, Heidelberg, 289-295.

Browell E.V., Ismail S. and Grant W.B., 1998: Differential absorption lidar (DIAL) measurements from air and space, *Appl. Phys*. *B*, **67**, 399-210.

Bruneau D., Cazeneuve H., Loth C. and Pelon J., 1991: Double-pulse dual-wavelength alexandrite laser for atmospheric water vapor measurement, *Appl. Opt.*, **30**, 3930-3937.

Bruneau D., Arnaud des Lions T., Quaglia P. and Pelon J., 1994: Injection-seeded pulsed alexandrite laser for differential absorption lidar application, *Appl. Opt.*, **33**, 3941-3950.

Bruneau D., Quaglia P., Flamant C., Meissonnier M. and Pelon J., 2001a: Airborne Lidar LEANDRE II for Water-Vapor Profiling in the Troposphere. I. System description, *Appl. Opt.*, **40**, 3450-3461.

Bruneau D., Quaglia P., Flamant C. and Pelon J., 2001b: Airborne Lidar LEANDRE II for Water-Vapor Profiling in the Troposphere. II. First results, *Appl. Opt.*, **40**, 3462-3475.

Canova F., Chambaret J.-P., Mourou G., Sentis M., Uteza O., Delaporte P., Itina T., Natoli J.-Y., Commandre M. and Amra C., 2005: Complete characterization of damage threshold in titanium doped sapphire crystals with nanosecond, picosecond, and femtosecond laser pulses., In *Laser-Induced Damage in Optical Materials* Ed. by Exarhos G. J., Guenther A. H., Lewis K. L., Ristau D., Soileau M. J., Stolz C. J. (Proceedings of the SPIE 5991), 639-645.

Chalon G., Cayla F. and Diebel D., 2001: An Advanced Sounder for Operational Meteorology, *52nd Congress of IAF*, Toulouse France.

Di Girolamo, P., Summa D., Bauer H., Wulfmeyer V., Behrendt A., Ehret G., Mayer B., Wirth M., and Kiemle C., 2004: Simulation of the performance of WALES based on an end-to-end model. 22nd International Laser Radar Conference. July 12-12, Matera, Italy.

Drever R., Hall J., Kowalski F., Hough J., Ford G., Munley A. and Ward H., 1983: Laser phase and frequency stabilization using an optical resonator, *Appl. Phys. B*, **31**, 97-105.

DWD, 2001: Quarterly report of the operational NWP-models of the Deutscher Wetterdienst. Business Area and Development, Report Nr. **28**, Deutscher Wetterdienst, Offenbach 2001.

Eloranta E. and Forrest D., 1992: Volume-imaging lidar observations of the convective structure surrounding the flight path of a flux-measuring aircraft, *J. Geophys. Res.,* **97**, 18383–18393.

Elsayed K. A., DeYoung R. J., Petway L. B., Edwards W. C., Barnes J. C. and Elsayed-Ali H. E., 2003: Compact High-Pulse-Energy Ultraviolet Laser Source for Ozone Lidar Measurements, *Appl. Opt*. **42**, 6650-6660.

Emanuel K., Raymond D., Betts A., Bosart L., Bretherton C., Droegemeier K., Farell B., Fritsch J.M., Houze R., LeMone M., Lilly D., Rotunno R., Shapiro M., Smith R. and Thorpe A., 1995: Report of the first prospectus development team of the U.S. Weather Research Program to NOAA and the NSF, *Bull. Amer. Meteor. Soc.*, **76**, 1194-1208.

Ertel K., Linné H. and Bösenberg J., 2005: Injection-seeded pulsed Ti:sapphire laser with novel stabilization scheme and capability of dual-wavelength operation, *Appl. Opt.*, **44**, 5120-5126.

References

ESA 2008, Callies J., Learner R.C.M., Schermaul R., Zobov N.F., Newnham D.A., Ballard J. and Tennyson J.: Measurement of H2O Absorption Cross-Sections, *British Atmospheric Data Centre*,. available from http://badc.nerc.ac.uk/data/esa-wv .

Fabry F., Frush C., Zawadzki I. and Kilambi A., 1997: On the Extraction of Near-Surface Index of Refraction Using Radar Phase Measurements from Ground Targets, *J. Atmos. Oceanic Technol.*, **14**, 978–987.

Ferrare R. A., Turner D. D., Brasseur L. H., Feltz W. F., Dubovik O. and Tooman T. P., 2001: Raman lidar measurements of the aerosol extinction-to-backscatter ratio over the Southern Great Plains, *J. Geophys. Res.*, **106**(D17), 20333–20347.

Fix A., 2006: Private discussions, DLR Oberpfaffenhofen.

Gérard, É., Tan D. G. H., Garand L., Wulfmeyer V., Ehret G., and Di Girolamo P., 2004: Major advances foreseen in humidity profiling from WALES (Water Vapour Lidar Experiment in Space). *Bull. Amer. Meteor. Soc.*, 85, 237-251.

Gimmestad G., 2005: Differential-Absorption Lidar for Ozone and Industrial Emissions, in *Lidar - Range-resolved optical remote sensing of the atmosphere,* Ed. by Weitkamp C., Springer, New York.

Grund C.J., Banta R.M., George J.L., Howell J.N., Post M.J., Richter R.A. and. Weickmann A.M, 2001: High-Resolution Doppler Lidar for Boundary Layer and Cloud Research, *J. Oceanic Atmos. Technol.* **18**, 376.

Hamilton M., Atkinson R., Dinovitser A., Peters E. and Vincent R.A., 2008: Towards low-cost water-vapour differential absorption lidar, *24th International Laser Radar Conference*, Boulder.

Hänsch T.W. and Couillaud B., 1981: Laser frequency stabilization by polarization spectroscopy of a reflecting reference cavity, *Opt. Commun.* **35**, 441.

Henderson S.W., Yuen E.H. and Fry E.S., 1986: Fast resonance-detection technique for single-frequency operation of injection-seeded Nd:YAG lasers, *Opt. Lett.* **11**, 715.

Hense, A., Adrian G., Kottmeier C., Simmer C. and Wulfmeyer V., 2004: Das Schwerpunktprogramm SPP 1167 der Deutschen Forschungsgemeinschaft „Quantitative Niederschlagsvorhersage", DMG-Mitteilungen.

HITRAN 2005, Rothmana L.S., Jacquemarta D., Barbeb A., Bennerc C. D., Birkd M., Browne L.R., Carleerf M.R., Chackerian C. Jr.g, Chancea K., Couderth L.H., Danai V., Devic V.M.,

Flaudh J.-M., Gamachej R.R., Goldmank A., Hartmannh J.-M., Jucksl K.W., Makim A.G., Mandini J.-Y., Massien S.T., Orphalh J., Perrinh A., Rinslando C.P., Smitho M.A.H., Tennysonp J., Tolchenovp R.N., Tothe R.A., Vander A. J., Varanasiq P. and Wagnerd G.: The HITRAN 2004 molecular spectroscopic database, *J. of Quant. Spectr. & Rad. Tr.,* **96**, 139-204.

Hodgson N. and Weber H., 1997: Optical resonators: fundamentals, advanced concepts and applications, Springer, London.

IPCC 2007: The Physical Science Basis. Contribution of Working Group I to the Fourth Assessment Report of the Intergovernmental Panel on Climate Change, Ed. Solomon S., Qin D., Manning M., Chen Z., Marquis M., Averyt K.B., Tignor M. and Miller H.L., Cambridge University Press, Cambridge, United Kingdom and New York, NY, USA.

IPCC 2008:, Eds., Climate Change and Water. Technical Paper of the Intergovernmental Panel on Climate Change, Ed. Bates B.C., Kundzewicz Z.W., Wu S. and. Palutikof J.P, IPCC Secretariat, Geneva.

Ismail S., Ferrare R., Browell E., Kooi S., Notary A., Butler C., Burton S., Fenn M., Krishnamutri T., Dunion J., Heymsfield G. and Anderson B., 2008: LASE measurements of water vapour, aerosol, and cloud distributions in Saharan air layers and tropical disturbances, *24th International Laser Radar Conference*, Boulder, USA.

ISO 11146-1, 2005(E): Lasers and laser-related equipment — Test methods for laser beam widths, divergence angles and beam propagation ratios — Part 1: Stigmatic and simple astigmatic beams.

Jedlovec G.J., 1990: Precipitable water estimation from high-resolution split window radiance Measurements, *J. Appl. Meteor*., **29**, 851-865.

Koechner W., 1996: Solid-state laser engineering, Springer-Verlag, Berlin.

Koechner W, 1970: Thermal lensing in a Nd:YAG laser rod. *Appl Opt*, **9**, pp. 2548–2553

Konno S., Shuichi F. and Yasui K., 1997: "80 W cw TEM00 1064 nm beam generation by use of a laser-diode-side-pumped Nd:YAG rod laser, *Appl. Phys. Lett.*, **70**, 2650–2651.

Mattis I., Ansmann A., Althausen D., Jänisch V., Wandinger U., Müller D., Arshinov Y. F., Bobrovnikov S. M. and Serikov I. B., 2002: Relative humidity profiling in the troposphere with a Raman lidar, *Appl. Optics*, **41**, 6451-6462.

References

Melfi S.H., Lawrence J.D. and McCormick M.P., 1969: Observation of Raman scattering by water vapor in the atmosphere, *Appl. Phys. Lett.,* **15**, 295-297.

Moulton, P.F., 1982: *22nd Int. Quantum Electronics Conference*, Munich, Germany.

Moulton, P.F., 1986: Spectroscopic and lasing characteristics of Ti:Al2O3, *J. Opt. Soc. Am. A*, **43**, 125-133.

Nehrir A. R., Repasky K. S., Obland M. D., Xiong Y., Carlsten J. L. and Shaw J. A., 2008: Water vapor profiling using a compact widely tunable diode laser differential absorption lidar (DIAL), *24th International Laser Radar Conference*, Boulder CO, US.

Ostermeyer M., Kappe P., Menzel R. and Wulfmeyer V., 2005: Diode-pumped Nd:YAG master oscillator power amplifier with high pulse energy, excellent beam quality, and frequency-stabilized master oscillator as a basis for a next-generation lidar system, *Appl. Optics*, **44**, 582-590.

Pal S., Behrendt A., Bauer H., Radlach M., Riede A., Schiller M., Wagner G. and Wulfmeyer V., 2008: 3-dimensional observations of atmospheric variables during the field campaign COPS, *IOP Conf. Ser.: Earth Environ. Sci.,* **1**, 012031.

Pal S., Behrendt A.,. Radlach M, Schaberl T. and Wulfmeyer V., 2006: Eye-safe scanning aerosol lidar at 355 nm, *23rd International Laser Radar Conference*, Nara, Japan.

Park Y.K., Giuliani G. and Byer R.L., 1984: Single axial mode operation of a Q-switched Nd:YAG oscillator by injection seeding, *IEEE J. Quantum Electron.*, **20**, 117.

Petrova-Mayor, A., Wulfmeyer V., and Weibring P., 2008: Development of an eye-safe solid-state tunable laser transmitter in the 1.4-1.5-µm wavelength region based on Cr^{4+}:YAG crystal for lidar applications, *Appl. Opt.*, **47**, 1522-1534.

Radlach M., Behrendt A. and V. Wulfmeyer, 2008: Scanning rotational Raman lidar at 355 nm for the measurement of tropospheric temperature fields, *Atmos. Chem. Phys.*, **8**, 159-169, http://www.atmos-chem-phys.net/8/159/2008/acp-8-159-2008.pdf.

Rahn L.A., 1985: Feedback stabilization of an injection-seeded Nd:YAG laser, *Appl. Opt.*, **24**, 940.

Rudich Y., Kaufman Y. J., Dayan U., Yu H., Kleidman R.G., 2008: Estimation of transboundary transport of pollution aerosols by remote sensing in the eastern Mediterranean, *J. of Geoph. Res.*, **113**.

Schlüssel P., 1989: Satellite-derived low--level atmospheric water vapour content from synergy of AVHRR and HIRS, *J. Rem. Sens.* **10**, 705-721.

Schotland R.M., 1966: Some observations of the vertical profile of water vapor by means of a ground based optical radar. In *Proc. Fourth Symposium on Remote Sensing of the Environment*, University of Michigan.

Siegman A., 1986: Lasers, University science books, Sausalito.

Spuler S.M., Mayor S.D., 2005: Scanning Eye-Safe Elastic Backscatter Lidar at 1.54 μm, *J. of Atm. and Oc. Tech.*, 22, 696

Sträßer A., Waltinger T. and Ostermeyer M., 2007: Injection seeded frequency stabilized Nd:YAG ring oscillator following a Pound–Drever–Hall scheme, *Appl. Opt.*, **46**, 8358-8363.

Stry S.,Thelen S., Sacher J., Halmer D., Hering P. and Mürtz P. 2006: Widely tunable diffraction limited 1000 mW external cavity diode laser in Littman/Metcalf configuration for cavity ring-down spectroscopy, *Appl. Phys. B,* **85**, 365-374.

Vassen W., Zimmermann C., Kallenbach R. and Hänsch T.W., 1990: A frequency-stabilized titanium sapphire laser for high-resolution spectroscopy, *Opt. Commun.*, **75**, 435-440.

Vogelmann H. and Trickl T., 2008: Wide-range sounding of free-tropospheric water vapor with a differential-absorption lidar (DIAL) at a high-altitude station, *Appl. Opt.* **47**, No. 12.

Wagner G., Shiler M. and Wulfmeyer V., 2005: Simulations of thermal lensing of a Ti:Sapphire crystal end-pumped with high average power, *Opt. Express* **13**, 8045-8055.

Wagner G., 2009: Theoretical analysis and design of high performance frequency converters for lidar-systems, Doctoral thesis, Inst. of Physics and Meteorology, University Hohenheim, Stuttgart, Germany.

Wandinger, U., 2005: Introduction to lidar, Raman lidar, In *Lidar - Range-resolved optical remote sensing of the atmosphere,* Ed. Weitkamp C., Springer, New York.

Weckwerth T. M., Wulfmeyer V., Wakimoto R. M., Hardesty R. M., Wilson J. W., and Banta R. M., 1999: NCAR/NOAA lower tropospheric water vapor workshop, *Bull. Amer. Meteor. Soc.* **80**, 2339-2357.

References

Wieser A., 2005: The Karlsruhe Doppler Wind Lidar: Comparison with Tower-, Profiler-, Sodar-, Radiosonde- and Thethersonde-Data, *European Geosciences Union (EGU), General assembly*, Wien, Austria.

Wirth M., Fix A., Mahnke P., Schwarzer H., Schrandt F. and Ehret G., 2009: The airborne multi-wavelength water vapor differential absorption lidar WALES: system design and performance, *Appl.Phys.B*, DOI 10.1007/s00340-009-3365-7

Wohlfahrt C., 2006: Development of a widely tunable, frequency stable diode laser with online/offline frequency switching for differential absorption lidar applications, Diploma thesis, Inst. of Physics and Meteorology, University Hohenheim, Stuttgart, Germany.

Wulfmeyer V. and Bösenberg J., 1994: Water vapor DIAL using an Alexandrite regenerative amplifier, *17th International Laser Radar Conference*, Paper 26A1, 149.

Wulfmeyer V., Bösenberg J., Lehmann S., Senff C. and Schmitz St., 1995: Injection-seeded alexandrite ring laser: performance and application in a water-vapor differential absorption lidar, *Opt. Lett.* **20**, 638-640.

Wulfmeyer V. and Bösenberg J., 1996: Single-mode operation of an injection-seeded alexandrite ring laser for application in water-vapor and temperature differential absorption lidar, *Opt. Lett*. **21**, 1150-1152.

Wulfmeyer V., 1998: Ground-based differential absorption lidar for water-vapor and temperature profiling: Requirements, development, and specifications of a high-performance laser transmitter, *Appl. Opt.,* **37**, 3804-3824.

Wulfmeyer V. and J. Bösenberg, 1998: Ground-based differential absorption lidar for water-vapor profiling: Assessment of accuracy, resolution, and meteorological applications, *Appl. Opt*. **37**, 3825-3844.

Wulfmeyer V., 1999a: Investigation of turbulent processes in the lower troposphere with water-vapor DIAL and Radar-RASS, *J. Atmos. Sci*,. **56**, 1055-1076.

Wulfmeyer V., 1999b: Investigations of humidity skewness and variance profiles in the convective boundary layer and comparison of the latter with large eddy simulation results. *J. Atmos. Sci.* **56**, 1077-1087.

Wulfmeyer V., Randall M., Walther C., Newsom R., Brewer A. and Hardesty R. M., 2000a: High-performance 2-mm Doppler lidar and its shipborne applications in the tropical marine boundary layer, *20th International Laser Radar Conference*, Vichy.

Wulfmeyer V., Randall M., Brewer A. and Hardesty R.M., 2000b: 2mm Doppler lidar transmitter with high frequency stability and low chirp, *Opt. Lett*. **25**, 1228-1230.

Wulfmeyer V. and Walther C., 2001a: Future performance of ground-based and airborne water vapor differential absorption lidar. I: Overview and theory. *Appl. Opt*. **40**, 5304-5320.

Wulfmeyer V., and Walther C., 2001b: Future performance of ground-based and airborne water vapor differential absorption lidar. II: Simulations of the precision of a near-infrared, high-power system, *Appl. Opt*. **40**, 5321-5336.

Wulfmeyer V., Ansmann A., Bach H.-G., Brauch U., Behrendt A., Eichler H., Hoffman D., Huber G., Klingenberg H. and Ostermeyer M., 2006: Lidar Reference System Based on a High-power Laser, Application for a DFG Research Unit.

Wulfmeyer V., Behrendt A., Bauer H.S., Kottmeier C., Corsmeier U., Blyth A., Craig G., Schumann U., Hagen M., Crewell S., Di Girolamo P., Flamant C., Miller M., Montani A., Mobbs S., Richard E., Rotach M.W., Arpagaus M., Russchenberg H., Schlüssel P., König M., Gärtner V., Steinacker R., Dorninger M., Turner D.D., Weckwerth T., Hense A. and Simmer C., 2008a: The convective and orographically-induced precipitation study: a research and development project of the world weather research program for improving quantitative precipitation forecasting in low-mountain regions, *Bull. Amer. Meteor. Soc.* **89** (10), 1477-1486.

Wulfmeyer V., Behrendt A., Bauer H.-S., Corsmeier U., Kottmeier C., Craig G., Ehret G., Hagen M., Schumann U., Volkert H., Blyth A., Crewell S., Di Girolamo P., Flamant C., Miller M., Montani A., Mobbs S., Richard E., Rotach M.W., Arpagaus M., Russchenberg H., Schlüssel P., König M., Gärtner V., Steinacker R., Dorninger M., Turner D.D. and Weckwerth T., 2008b: The convective and orographically-induced precipitation study: A research and development project of the world weather research program, *Reviewed and Revised Papers of the 24th International Laser Radar Conference,* 24 - 28 June 2008, Boulder, Colorado.

Yamakawa K. and Barty C.P.J., 2000: Ultrafast, ultrahigh-peak, and high-average power Ti:sapphire laser system and its applications. IEEE J. *Select. Topics Quantum Electron*. **6**, 658-675.

References

Zavelani-Rossi M., Lindner F., Le Blanc C., Cheriaux G. and Chambaret J.P., 2000: Control of thermal effects for high-intensity Ti:sapphire laser chains, *Appl. Phys. B*, **70**, 193-196.

Zuev V. V., Zuev V. E., Makushkin Yu. S., Marichev V. N., and. Mitsel A. A, 1983: Laser sounding of atmospheric humidity: experiment, *Appl. Opt.* **22**, 3742-3746.

Пахомов И.И., Рожков О.В. и Рождествин В.Н., 1982: Оптико-электронные квантовые приборы. Москва, Радио и связь.

Acknowledgements